Searching for Axions from Celestial Objects with the X-Ray Telescope at CAST

Tillmann Guthörl

Physikalisches Institut
Albert-Ludwigs-Universität Freiburg

Searching for Axions from Celestial Objects with the X-Ray Telescope at CAST

Diplomarbeit

vorgelegt
von

Tillmann Guthörl

Physikalisches Institut
Albert-Ludwigs-Universität
Freiburg

September 2009

Contents

List of Figures

List of Tables

1. Introduction

The standard model of particle physics is a theoretical framework that is quite successful in discribing strong, electromagnetic and weak interactions. Despite its wide validity, the standard model has some blemishes. For instance, the so-called strong CP-problem is not understood so far. Invariance under charge- (C) and parity-transformation (P) is violated in the weak interaction, but such violation has not been observed in case of the strong interaction yet. One explanation for this puzzling detail could be the existance of an additional symmetry in Quantum Chromo Dynamics (QCD), that is spontaniously broken at an unknown scale. This broken symmetry in turn would give rise to a light, neutral pseudoscalar particle named *axion*.

Having a predicted mass of above 100 keV/c^2, the original axion was soon ruled out experimentally. After that, new models were developed that predict a light and very weakly interacting type of axion. This so-called *invisible axion* is, depending on its actual mass, an excellent candidate for cold dark matter. Axions would be produced via the Primakoff effect, i.e. conversion of a real photon to an axion under the influence of a virtual photon provided by an electric or magnetic field. Thus strong X-ray sources are good candidates for axion production.

The CAST experiment at CERN makes use of the inverse Primakoff effect to detect axions. A magnetic field of 9.0 T, provided by a decomissioned LHC prototype dipole magnet, is used to re-convert incoming axions to X-ray photons. In total, 3 different low-background X-ray detectors are operated to detect such re-conversions. Although CAST is designed to detect axions emitted by the sun, right from the beginning an observation of outstanding galactic objects was intended as well [1, 2]. These targets are the two bright X-ray sources Scorpio X-1 and the Crab nebula along with Sagittarius A, which is at the centre of our galaxy.

In 2003, Sco X-1 was observed for 25.15 hours in total and the galactic centre was tracked for 6.2 hours. The data obtained with the Charge Coupled Device (CCD) detector during these trackings is analysed in the scope of this work.

In the first part of this thesis the theoretical development in QCD, which later led to the postulation of the axion, is reviewed. A short overview on axion physics is given and the role of the axion as a dark matter candidate is investigated. In Chapter 3, the setup of the CAST experiment is discribed in detail, including the X-ray detectors and their properties. The focus is set on the X-ray telescope and the CCD detector. After that, a short introduction to the investigated celestial objects is given in Chapter 4, followed by the analysis of the data in Chapter 5. Since no signal above background was

observed, an upper limit on the free fit parameter flux times axion-to-photon coupling constant^2 ($\phi g_{a\gamma}^2$) is derived for both Sgr A and Sco X-1, using the method of maximum likelihood. The results are reviewed and conclusions concerning the feasibility of axion astronomy are drawn.

2. The Axion

This chapter illustrates the development in QCD that later led to the postulation of the axion, a hypothetical neutral pseudoscalar particle. After a short introduction of the motivation for axions a brief discussion on axion properties is given, followed by some astrophysical and cosmological constraints that narrow the mass region in which axions can exist. Since the axion provides not only an elegant solution to the so-called Strong CP-Problem but would also contribute to Dark Matter the role of axions in this context is discussed here. This is followed by a glance at experimental attempts to detect axions.

2.1 Theoretical Motivation

Originally the axion was introduced as a solution of the Strong CP[1]-Problem, one of the few blemishes that Quantum Chromo Dynamics (QCD), the theory of the Strong Interaction, reveals. This problem results from a solution of the $U(1)_A$-Problem, that introduces a CP-violating term to the QCD Lagrangian.

2.1.1 The $U(1)_A$-Problem

Typically, calculations in QCD are done perturbatively, i.e. particles and interactions are characterised by expansions of the corresponding field around the ground state (vacuum). The Lagrangian of pertubative QCD can be written as

$$\mathcal{L}_{\text{pert}} = \sum_f \bar{q}_f(\gamma^\mu i D_\mu - m_f)q_f - \frac{1}{4}G^b_{\mu\nu}G_b^{\mu\nu}, \tag{2.1}$$

where f denotes the quark flavors, q the quark fields, m the current quark masses and $G^b_{\mu\nu}$ the gluon field tensor with b from 1 to 8. D_μ is the covariant derivative [3],

$$D_\mu = \partial_\mu + igT_bG^b_\mu. \tag{2.2}$$

with T_b being the generators of the group and g the strong coupling constant. In the limit of vanishing quark masses - which appears to be a good approximation since m_u and m_d are much smaller than the QCD scale [4] - $\mathcal{L}_{\text{pert}}$ is invariant under a global axial vector transformation $U(1)_A$ leading to a symmetry between left- and right-handed

[1] CP stands for charge and parity. It refers to the behavior of physical systems under charge conjugation and change of sign of all spatial coordinates (parity transformation).

quarks. This symmetry however is not observed in nature which means it must be spontaneously broken. As a result a massless Nambu-Goldstone boson should exist. In the more realistic case of non-vanishing but small quark masses this particle has a small mass itself and therefore is called a Pseudo-Goldstone boson. In total one would expect four Goldstone bosons for the $U(1)_A$-symmetry breaking to exist but only three are observed experimentally namely the Pi-Mesons (π^+, π^0 and π^-). The fourth candidate η' has the right quantum numbers ($J^P = 0^-$) but with a mass of 958 MeV/c^2 (compare $m_\pi = 135$ MeV/c^2) it is too heavy since the relation

$$m_{\eta'} \leq m_\pi \sqrt{3}, \tag{2.3}$$

should hold [5]. This missing forth Pseudo-Goldstone boson is referred to as the $U(1)_A$-Problem.

2.1.2 The Solution of the $U(1)_A$-Problem

A solution to the $U(1)_A$-problem was found by 't Hooft. He postulated an anomalous breaking of the $U(1)_A$-symmetry [6] which adds a term $\mathcal{L}_\Theta$ to the QCD Lagrangian

$$\mathcal{L}_\Theta = \Theta \frac{g^2}{32\pi^2} G_b^{\mu\nu} \tilde{G}^b_{\mu\nu}, \tag{2.4}$$

where Θ an angle between 0 and 2π, which results from the fact that the QCD vacuum is a superposition of an infinite number of degenerated vacua. To distinguish between different vacua a winding number n is introduced [7].

$$|\Theta\rangle = \sum_{n=-\infty}^{\infty} e^{-in\Theta} |n\rangle. \tag{2.5}$$

The dual of the gluon field strength tensor

$$\tilde{G}_b^{\mu\nu} = -\frac{1}{2} \epsilon^{\mu\nu\alpha\beta} G^b_{\alpha\beta}, \tag{2.6}$$

contains the ϵ-tensor which is not invariant under parity and therefore makes $\mathcal{L}_\Theta$ CP-violating. Including electroweak interactions as well, equation 2.4 converts to

$$\mathcal{L}_{\bar{\Theta}} = \bar{\Theta} \frac{g^2}{32\pi^2} G_b^{\mu\nu} \tilde{G}^b_{\mu\nu}, \tag{2.7}$$

with $\bar{\Theta} = \Theta + \arg(\det M)$ where M is the quark mass matrix [4].

2.1.3 The Strong CP-Problem

As a consequence of the introduction of the CP-violating term $\mathcal{L}_{\bar{\Theta}}$ to the QCD Lagrangian the neutron is expected to have an electric dipole moment d_n depending on the actual value of $\bar{\Theta}$ [8]

$$d_n \approx 5 \times 10^{-16} \bar{\Theta} \text{ e cm}. \tag{2.8}$$

The current experimental limit on the electric dipole moment of the neutron [9, 10] is however

$$|d_n| < 12 \times 10^{-26} \text{ e cm}, \tag{2.9}$$

at 95 % confidence level which implies that $\bar{\Theta} \leq 10^{-10}$. The fact that $\bar{\Theta}$ is so small (or even zero), although in principle it could take any value between 0 and 2π, is known as the so-called Strong CP-Problem.

2.1.4 The Peccei-Quinn Solution

There are several possible solutions to the Strong CP-Problem where the idea of introducing an additional chiral symmetry seems to be the most promising one [4]. This so-called $U(1)_{\text{PQ}}$-symmetry[2] is necessarily spontaneously broken and its introduction compensates the static CP-violating term $\bar{\Theta}$ with a dynamical CP-conserving field a [11, 12]. This broken symmetry is associated with a new Pseudo-Goldstone boson - the axion[3] [13, 14]. Three new terms are added to the QCD-Lagrangian:

$$\mathcal{L}_{\text{total}} = \mathcal{L}_{\text{pert}} + \mathcal{L}_{\bar{\Theta}} - \frac{1}{2}\partial_\mu a \partial^\mu a + \mathcal{L}_{\text{int}} + C_a \frac{a}{f_a} \frac{g^2}{32\pi^2} G_b^{\mu\nu} \tilde{G}^b_{\mu\nu}, \tag{2.10}$$

where f_a is the scale parameter at which the symmetry breaking occurs and C_a is a model dependent constant. The third term represents the kinetic energy, $\mathcal{L}_{\text{int}}$ represents interactions of the axion with e.g. fermions and the last term gives the axion field an effective potential with a minimum at $\langle a \rangle = -\bar{\Theta} f_a / C_a$.

$$\left\langle \frac{\partial V_{\text{eff}}}{\partial a} \right\rangle = -\frac{C_a}{f_a} \frac{g_s^2}{32\pi^2} \left\langle G_b^{\mu\nu} \tilde{G}^b_{\mu\nu} \right\rangle \Big|_{\langle a \rangle = -\bar{\Theta} f_a / C_a} = 0. \tag{2.11}$$

At this minimum the $\bar{\Theta}$ term is cancelled and the Strong CP-Problem is solved dynamically. Expanding the potential around the minimum gives the axion a mass [4]

$$m_a^2 = \left\langle \frac{\partial^2 V_{\text{eff}}}{\partial a^2} \right\rangle = -\frac{C_a}{f_a} \frac{g^2}{32\pi^2} \frac{\partial}{\partial a} \left\langle G_b^{\mu\nu} \tilde{G}^b_{\mu\nu} \right\rangle \Big|_{\langle a \rangle = -\bar{\Theta} f_a / C_a}. \tag{2.12}$$

[2] PQ is an abbreviation for Peccei-Quinn.

[3] Both S. Weinberg and F. Wilczek pointed out this fact independently. The new particle was named by F. Wilczek.

The existence of the axion however is yet to be proven. So far only upper limits on e.g. the axion to photon coupling could be derived by certain experimental approaches (cp. [10, 15] and Sec. 2.4).

2.1.5 The Axion as a Dark Matter Candidate

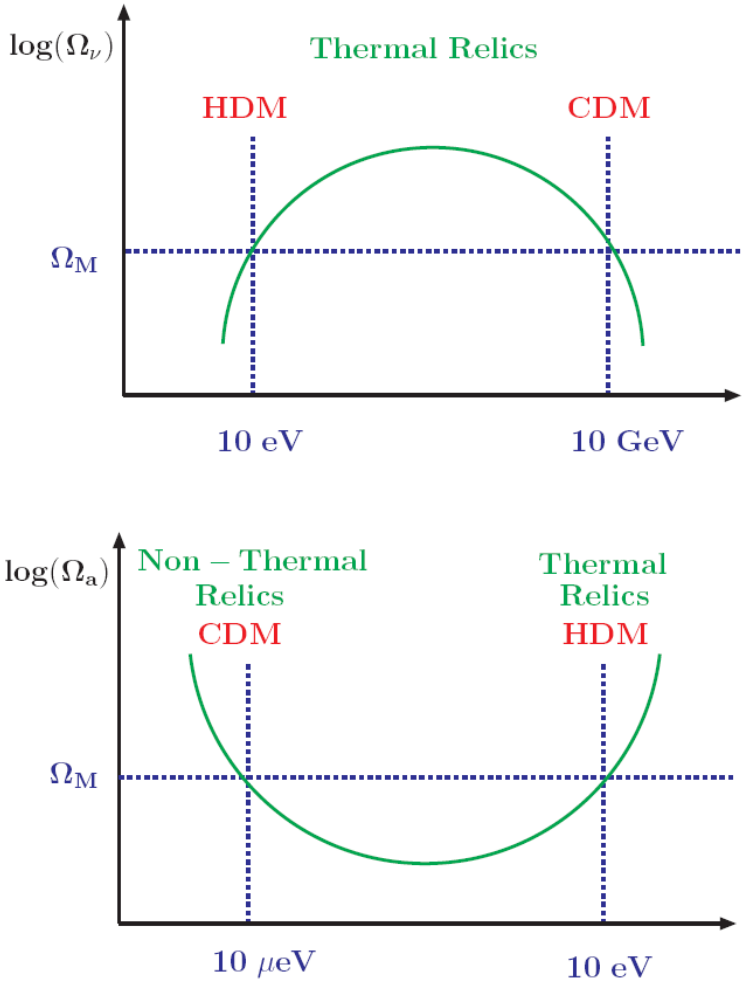

Figure 2.1: Schematic Lee-Weinberg curves for neutrinos (upper picture) and axions (lower picture). $\Omega_{a(\nu)}$ refers to the fraction axions (neutrinos) contribute to the total amount of energy in the universe. Ω_M denotes the total amount of matter both baryonic and non-baryonic. Picture taken from [16].

Looking at rotational curves of spiral galaxies, a discrepancy between observed velocity and computed velocity according to Kepler's laws of motion can be found. This implies the existence of further gravitating mass, not taken into account for the predictions, or the need to modify the laws of gravity [17]. Recent observations of colliding galaxy clusters [18] favor the existence of a new type of matter, which can not be seen by

astronomical observations, because it does not emit electromagnetic radiation and is therefore called *dark matter*. For explanation of such non-luminous matter[4], a new weakly interacting particle[5] has to be introduced. Predicted particles that would be able to contribute to dark matter are the axion and *weakly interacting massive particles* (WIMPs). Among others, the latter could be realised by the *lightest supersymmetric particle* (LSP), which occurs in supersymmetric extensions to the standard model of particle physics [19].

Axions can contribute to dark matter if produced in early stages of the universe. The role these so-called relic axions can play, highly depends on their production mechanism (cp. Sec. 2.3.2). Thermally produced axions would be part of the hot dark matter component which can only be a certain fraction of dark matter, since an over-dominant hot dark matter component would smear out cosmic large scale structures [21]. The universe thus would not have formed as observed today. If produced by misalignment effects or axion string decay, relic axions would be non-thermal and therefore part of the cold dark matter component. The fact that light axions would contribute to cold dark matter, whereas heavy axions would contribute to hot dark matter is contrary to the behavior of neutrinos and WIMPs. This intuition contradicting behavior is a consequence of the fact that light axions were not relativistic when being produced. This circumstance is illustrated in Fig. 2.1, which shows the mass dependency of the fraction of energy that axions (neutrinos) contribute to the total amount of energy in the universe.

2.2 Axion Properties

Axion properties basically depend on the scale f_a where the PQ-symmetry is broken. The axion mass m_a and coupling constants[6] g_{ai} which describe the strength of the coupling of axions to other particles i are inversely proportional to the breaking scale:

$$m_a \propto \frac{1}{f_a}, \tag{2.13}$$

$$g_{ai} \propto \frac{1}{f_a}. \tag{2.14}$$

2.2.1 Axion Coupling

Depending on the actual model (see Sec. 2.2.3) axions do or do not couple to certain particles. The coupling to gluons is independent of the model and therefore given for

[4]The term "non-luminous" in principle can also refer to large astronomical bodies that are unable to ignite fusion processes, but by using gravitational micro lensing the number of such objects has been determined to be too low to explain the gravitational behavior of galaxies [17].

[5]The only candidate the standard model offers is the *neutrino* which gets a non-zero mass from an extension of the standard model. But since light neutrinos are *hot dark matter* they are incapable to allow for formation of structures as observed in the universe [19, 20].

[6]Sometimes g_{aii} is used instead of g_{ai} to indicate that the axion couples to two particles of the same kind.

all axions as well as the axion photon coupling which is a consequence of the axion gluon coupling. The term $\mathcal{L}_{\text{int}}$ in Eq. 2.10 can be decomposed into terms representing the individual contribution to the Lagrangian for each coupling.

$$\mathcal{L}_{\text{int}} = \mathcal{L}_{a\gamma} + \mathcal{L}_{ag} + \mathcal{L}_{af}. \tag{2.15}$$

$\mathcal{L}_{a\gamma}$ represents the coupling of axions to photons, $\mathcal{L}_{ag}$ the coupling to gluons and $\mathcal{L}_{af}$ the coupling to fermions.

Coupling to Gluons

Axions couple to gluons via a triangle loop giving

$$\mathcal{L}_{ag} = \frac{\alpha_s}{8\pi f_a} a\, G_b^{\mu\nu} \tilde{G}^b_{\mu\nu}, \tag{2.16}$$

with α_s being the strong coupling constant. From the axion-gluon coupling results the axion-pion mixing as illustrated in Fig. 2.2. This can be used to compute the mass of the axion:

$$m_a = \frac{m_{\pi^0} f_\pi}{f_a} \left(\frac{z}{(1+z+w)(1+z)} \right)^{\frac{1}{2}}, \tag{2.17}$$

where z denotes the mass ratio of u- and d-quarks while w denotes the mass ratio of u- and s-quarks. Using the known pion mass $m_{\pi^0} = 135\ \text{MeV}/c^2$ and its decay constant $f_\pi = 93$ MeV, as well as the quark mass ratios $z = 0.568 \pm 0.042$ and $w = 0.0290 \pm 0.0043$ [22] one obtains

$$m_a \approx 0.60\,\text{eV}/c^2 \frac{10^7 \text{GeV}}{f_a}, \tag{2.18}$$

an expression that is frequently used in axion physics [23].

Coupling to Photons

Due to the mixing with pions, axions couple also to photons (see Fig. 2.3). The corresponding contribution to the Lagrangian can be written as

$$\mathcal{L}_{a\gamma} = -\frac{1}{4} g_{a\gamma}\, F_{\mu\nu} \tilde{F}^{\mu\nu}\, a = g_{a\gamma}\, a\, \vec{E} \cdot \vec{B}, \tag{2.19}$$

where $\vec{E}$ denotes the electric and $\vec{B}$ the magnetic field. Independently of the model considered, axions can couple to fermions that carry PQ-charge[7] and therefore couple to photons via a fermion triangle loop as well. The coupling constant in that case can be expressed as [23]

[7] The PQ-charge is introduced along with the PQ-symmetry. It characterises the transformation of fermion fields under $U_{PQ}(1)$-transformation [23].

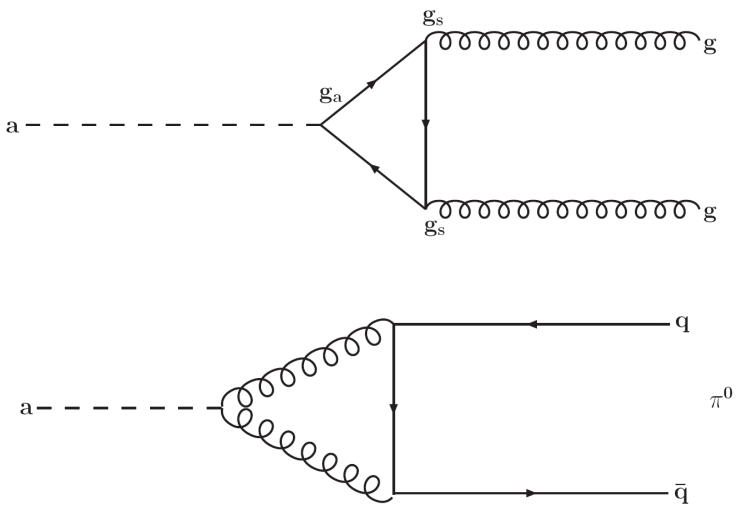

Figure 2.2: Axion to gluon coupling (upper image) and axion to $q\bar{q}$ coupling via two gluons leading to axion-pion mixing (lower image). g_s is the strong coupling constant and g_a the axion-fermion Yukawa coupling. Picture from [24].

$$g_{a\gamma} = \frac{\alpha}{2\pi f_a}\left(\frac{E}{N} - \frac{2(4+z+w)}{3(1+z+w)}\right). \tag{2.20}$$

E denotes the electromagnetic anomaly, while N represents the colour anomaly. The fraction E/N is a model dependent parameter:

$$\begin{aligned} E &= 2\sum_f X_f Q_f^2 D_f, \\ N &= \sum_f X_f. \end{aligned} \tag{2.21}$$

X denotes the PQ-charge, Q the electric charge and f is an index representing different fermions. $D_f = 1$ holds for colour singlets and $D_f = 3$ for colour triplets. Plugging in the values for the quark mass ratios, one obtains

$$g_{a\gamma} = \frac{\alpha}{2\pi f_a}\left(\frac{E}{N} - 1.92 \pm 0.08\right) = \frac{\alpha}{2\pi f_a} C_\gamma. \tag{2.22}$$

Besides the cases discussed above there are several more couplings to e.g. electrons or nucleons. These couplings are only mentioned here for completeness but do not play an important role in the scope of this work. However, they might play a vital role in astrophysical considerations concerning estimates of axion properties. For a compact but more detailed summary on axion couplings see reference [24] and references therein.

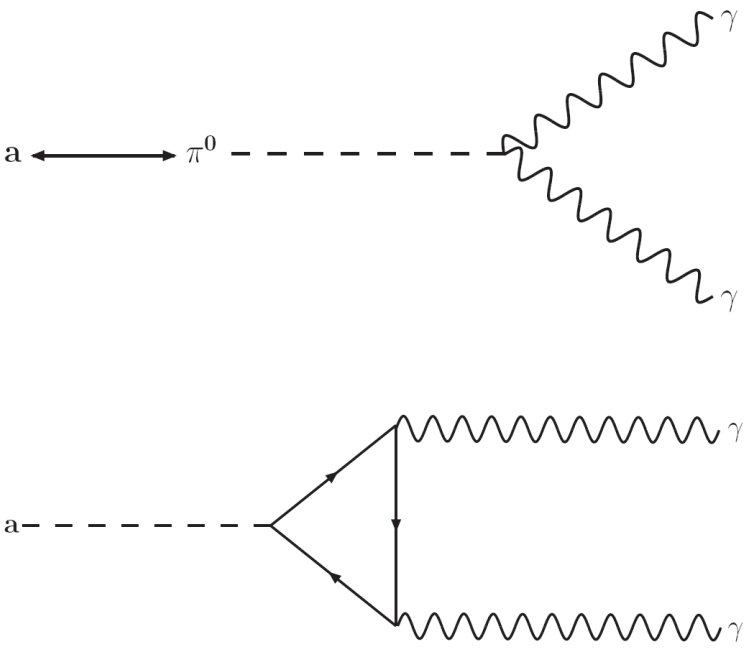

Figure 2.3: Axion to photon coupling via axion-pion mixing (upper image) and axion to photon coupling via a fermionic triangle loop (lower image). Picture from [24].

Primakoff Effect

The Primakoff effect is the conversion of a real photon into an axion after interaction with a virtual photon provided by a magnetic or electric field (see Fig. 2.4). This interaction takes place via a fermionic triangle loop and is expected to be one of the leading production processes of axions in hot plasmas as present in the interior of the sun or other celestial objects. The inverse Primakoff effect denotes the back conversion of axions into photons in a magnetic or electric field and is the working principle of *helioscopes* (cp. Sec. 2.4.4). Due to the interaction with virtual photons there is a direct momentum transfer between axions and real photons resulting in the fact that the original direction of motion is conserved.

2.2.2 Visible Axions

The originally proposed PQWW-axion[8] appears at a breaking scale f_a of the order of the electroweak scale, i.e. $f_a = f_{\text{weak}} \approx 250$ GeV implying an axion mass of $m_a \approx 200$ keV/c^2. Right from the beginning Weinberg doubted the existence of an axion with such properties due to the fact that large numbers of such particles should be created in nuclear reactors. This would have led to high count rates in NaI-detectors used for

[8] Peccei-Quinn-Weinberg-Wilczek

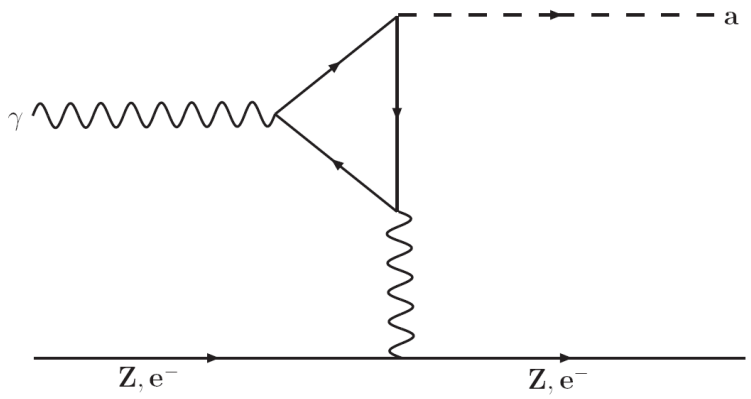

Figure 2.4: Feynman diagram of the Primakoff effect. Photons couple to axions via a fermionic triangle loop in the presence of a magnetic field or the electric fields of electrons or nuclei as shown in this diagram. Picture from [24].

reactor neutrino experiments in those days [13]. Besides that, experiments looking for axions from heavy meson decays like e.g.

$$J/\psi \rightarrow \gamma + a, \tag{2.23}$$

ruled out the existence of the PQWW-axion quickly [25]. Because of its high detectability the original axion is also referred to as *visible axion*.[9]

2.2.3 Invisible Axions

Since the original axion was excluded experimentally, a new type of axion, the so-called *invisible axion*, was introduced [26]. The choise of the breaking scale f_a is arbitrary and therefore can be much greater than the electroweak scale f_{weak}. This leads to a small axion mass and a weak coupling to other particles which reduces detectability. Although the term "invisible" implies no interaction[10] at all, it is in fact possible to detect such axions even though this is not an easy task.

KSVZ models

The first model for invisible axions was proposed by Kim [27], Shifman, Vainshtein and Zakharov [28]. Besides the weakly interacting axion it also postulates a new scalar meson σ^0 and a new heavy quark Q carrying Peccei-Quinn-charge. This is the only particle the axion couples to. Indirect coupling to other particles can be obtained via second order interactions. The fraction E/N can be calculated to be

$$\frac{E}{N} = 6\, Q_{\text{heavy}}, \tag{2.24}$$

[9] In up to date literature the term "visible" can also refer to *invisible axions* with energies corresponding to photons in the visible range. The meaning of "visible" usually gets clear from the context.

[10] besides gravity.

with $Q_{\text{heavy}} = -1/3, 2/3, 0, 1$ being the charge of the heavy quark which leads to values for E/N from -2 to 6 and the corresponding coupling constants according to Eq. 2.22. The probably most critical aspect about KSVZ-models is the existence of Q which should be - depending on its charge - detectable in collider experiments. Also fractionally charged stable hadrons $Q\bar{u}$, Quu, QQu and the neutral baryon QQQ, which would be a nice dark matter candidate, are expected in case $Q_{\text{heavy}} = 0$ [27].

DFSZ models

In models like those proposed by Dine, Fischler, Srednicki [29] and Zhitnitsky [30], axions are feebly interacting light particles that couple to all fermions since they all carry PQ-charge. The introduction of two Higgs doublets Φ_1 and Φ_2 is required just as it is in case of Grand Unified Theories (GUT). Using Eq. 2.21

$$\frac{E}{N} = \frac{2}{3}\frac{4X_u + X_d + 3X_e}{X_u + X_d}, \tag{2.25}$$

with $X_e = X_d$ the axion to photon coupling (cp. Eq. 2.22) can be derived:

$$g_{a\gamma} \approx -0.74\frac{\alpha}{2\pi f_a}. \tag{2.26}$$

Fig. 2.5 provides a comparison of mass dependencies of the axion to photon coupling for KSVZ and DSFZ models.

2.3 Theoretical Constraints

2.3.1 Astrophysical Constraints

If axions exist they are likely to be produced in stars via the production processes described above, thus providing a new energy loss channel due to their feebly interacting nature. This additional energy loss has consequences for stellar evolution so that its impact can be estimated and compared to astronomical data.

The energy loss due to axion production is expected to be more efficient in *horizontal branch stars* (HB)[11] than in *red giants* (RG)[12], which leads to the possibility to estimate axion production rates by comparing the number of HB stars and red giants. However, it has to be assured that all stars looked at are of the same age and therefore comparable. All stars within globular clusters are believed to have formed simultaneously, so that they are excellent candidates for these kinds of axion production rate estimates called

[11] Stars that ignited helium fusion are called horizontal branch stars due to their characteristic position in the so-called Hertzsprung-Russell diagram.

[12] At the end of their hydrogen burning phase, so-called *main sequence stars* develop bigger and cooler surfaces which let them appear as red giants. If the mass of a star is sufficiently large, the red giant phase is followed by the ignition of helium burning. For more information on stellar evolution and Hertzsprung-Russell diagrams see [17].

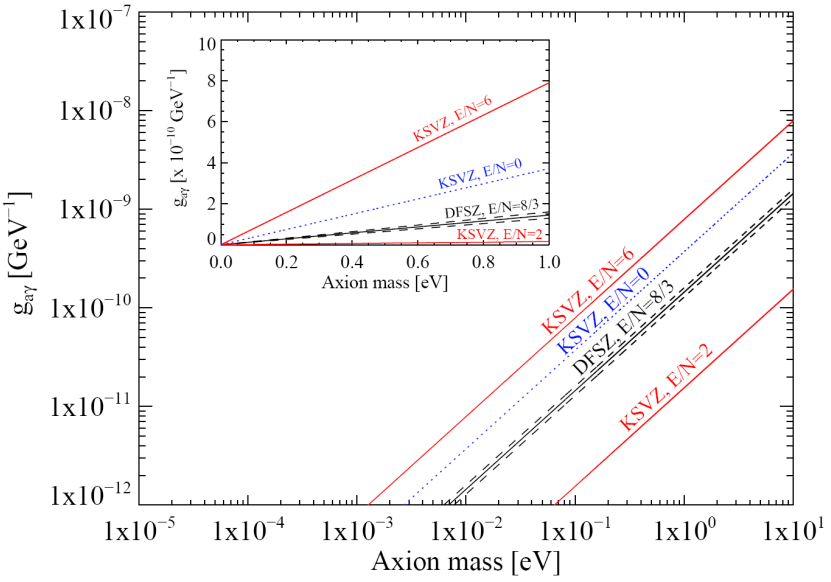

Figure 2.5: Predicted combinations of axion mass m_a and axion-to-photon coupling constant $g_{a\gamma}$. KSVZ and DSFZ models are shown with both logarithmic (main picture) and linear axes (embedded picture). Dashed black lines illustrate the error band for DSFZ predictions. Picture from [24].

globular cluster limit. From observations it is known that the luminosity for exotic energy loss channels L_x is at most 10% of the helium burning luminosity in HB stars [23]:

$$L_x = 0.1\, L_{3\alpha}. \tag{2.27}$$

Since helium burning takes place via the so-called triple alpha reaction the index 3α is used. This limitation can be translated into an energy loss rate using the estimated energy production rate via the triple alpha process $\epsilon_{3\alpha} = 8.0 \times 10^{-3}$ W/kg of [23]

$$\epsilon_x \lesssim 1.0 \times 10^{-3} \text{ W/kg}. \tag{2.28}$$

For average HB star temperature and density, Raffelt derives an energy loss rate for axions which are produced via the Primakoff effect, depending on the axion to photon coupling constant:

$$\epsilon_a \approx g_{10}^2 \cdot 3.0 \times 10^{-3} \text{ W/kg}, \tag{2.29}$$

with $g_{10} \equiv g_{a\gamma}/10^{-10}$ GeV^{-1}. Combined with Eq. 2.28 one obtains an upper limit on the coupling constant of [23]

$$g_{a\gamma} \lesssim 0.6 \times 10^{-10} \text{ GeV}^{-1}. \tag{2.30}$$

To take uncertainties of order 2 into account a limit of $g_{a\gamma} \lesssim 1.0 \times 10^{-10}$ GeV^{-1} is often used when comparing experimental data with theoretical restrictions [31].

2.3.2 Cosmological Constraints

Hot Dark Matter Limit

The model-independent axion-pion mixing

$$\pi + \pi \leftrightarrow \pi + a, \tag{2.31}$$

is the dominant axion production process for thermal axions at temperatures around $T = 200$ MeV. Axions produced in that process would be part of the hot dark matter (HDM). The WMAP[13] 5-year data allows the derivation of a limit on the total HDM contribution to dark matter and thus on the contribution of thermally produced axions which in turn yields an upper limit on the axion mass of

$$m_a < 1.02 \text{ eV}/c^2, \tag{2.32}$$

at 95% confidence level [20, 32].

Overclosure

Besides thermal production in the early universe axions can be produced by vacuum misalignment [33, 34, 35], axion string decay and axion domain wall[14] decay, where the contribution of axion domain wall decay is negligible. Thus it is possible to derive an estimate for the contribution to the cosmological density by axions Ω_a [36]

$$\Omega_a \approx \left(\frac{0.7}{h}\right)^2 \left(\frac{f_a}{10^{12} \text{ GeV}}\right)^{\frac{7}{6}}. \tag{2.33}$$

Here h denotes the Hubble parameter H_0 in units of 100 km/s/Mpc. From experiments it is known that the cold dark matter (CDM) contribution to the cosmological density is around $\Omega_{\text{CDM}} \approx 0.13$ [10], which leads to an upper limit on the axion decay constant $f_a \lesssim 10^{12}$ GeV, since the contribution of axions to the density of the universe can not exceed the density contribution of cold dark matter. Such an excess of dark matter would contradict the expansion of the universe as seen today. The upper limit on the decay constant can be translated into a lower limit on the axion mass according to Eq. 2.18.

$$m_a \gtrsim 10^{-6} \text{ eV}/c^2. \tag{2.34}$$

[13] Wilkinson Microwave Anisotropy Probe.

[14] Strings (1 dim.) and domain walls (2 dim.) are topological defects resulting from symmetry breaking.

2.4 Axion Detection

In the following a selection of experimental approaches undertaken to detect invisible axions is presented. None of these experiments was able to claim a discovery yet, but several regions in the axion parameter space could be excluded as can be seen in Fig. 2.6.

2.4.1 Microwave Cavity Experiments

As proposed by Sikivie in the early 1980s [37], the conversion of axions into photons via the Primakoff effect can be used to detect axions if they penetrate into a microwave cavity permeated with a magnetic field. The cavity has to be tunable to make the resonant frequency correspond to the unknown axion mass. Such microwave cavities are often used as *haloscopes*, which means they are looking for axions from the galactic halo, but can also be used to detect axions produced in laboratories. One showcase experiment is ADMX[15], covering the axion mass range [38]

$$1.98\,\mu\mathrm{eV}/c^2 < m_a < 2.17\,\mu\mathrm{eV}/c^2. \tag{2.35}$$

2.4.2 Crystal Detector Experiments

Crystal detector experiments also make use of the Primakoff effect, but instead of a magnetic field as in microwave cavities they use the Coulomb field of crystal atoms. Usually they are situated in underground laboratories to minimise background. They are either used as haloscopes or as *helioscopes*, which means they intend to detect axions emitted by the sun. In case of helioscopes, the Bragg condition for X-ray momentum transfer can be used to amplify the Primakoff conversion given that the relative orientation of the crystal to the sun is known. CDMS[16] is an example for crystal detector experiments giving an upper limit on the axion-photon-coupling of [39]

$$g_{a\gamma} < 2.4 \times 10^{-9}\ \mathrm{GeV}^{-1}, \tag{2.36}$$

for axion masses below 0.1 keV/c^2.

2.4.3 Laser Experiments

Photon Regeneration Experiments

The advantage of laboratory laser experiments over experiments looking for axion produced elsewhere is their independence of production models. The basic principle of such experiments is to produce axions in a first step, e.g. by shining an intense laser through a strong magnetic field, and then let them traverse through a barrier capable of blocking photons completely but transparent to axions, due to their low interaction probability. In a second step a back conversion of axions into photons, again by use

[15] Axion Dark Matter eXperiment.
[16] Cryogenic Dark Matter Search.

of a magnetic field, is intended. The detection of photons behind that barrier would indicate the successful creation and back-conversion of axions or other *axion like particles* (ALPs). The disadvantage of laboratory experiments is that the probability both for creation and detection of axions is very low, which makes a combination of both events quite improbable. Therefore laser experiments usually can not compete with other techniques in terms of discovery potential.

Polarisation Experiments

Photon regeneration experiments can easily be combined with polarisation experiments looking for initially linear polarised light to get elliptically polarised. This is expected to happen because the Primakoff effect just affects the electric field component parallel to the magnetic field, so that photons with matching orientation of the electric field vector are more likely to be converted to axions, leading to a changed overall polarization. PVLAS[17] is an example for polarisation experiments [40]. A representative for a combined "shining light through a wall" and polarisation experiment is OSQAR[18] [41].

2.4.4 Axion Telescopes

Axion telescopes, as proposed by Sikivie [37], make use of Primakoff conversion by applying a magnetic field perpendicular to the expected direction of motion of the axions. Therefore it is essential to build such experiments similar to ordinary telescopes, which means they have to be mounted on a movable device which allows them to track expected axion sources in order to maximise data taking time. The term "axion telescope" is not used very frequently. Experiments with a movable magnet such as CAST or the Tokyo Helioscope[19] are usually refered to as helioscopes (cp. Fig. 2.6) since their main purpose is to look for solar axions even though they might be used to investigate other celestial objects as well. The conversion volume of such experiments can either contain a vacuum or a buffer gas such as helium, to investigate certain axion mass ranges (see Sec. 3.4 for details).

[17] Polarizzazione del Vuoto con LASers.
[18] Optical Search for QED vacuum birefringence, Axion and photon Regeneration.
[19] Sumico.

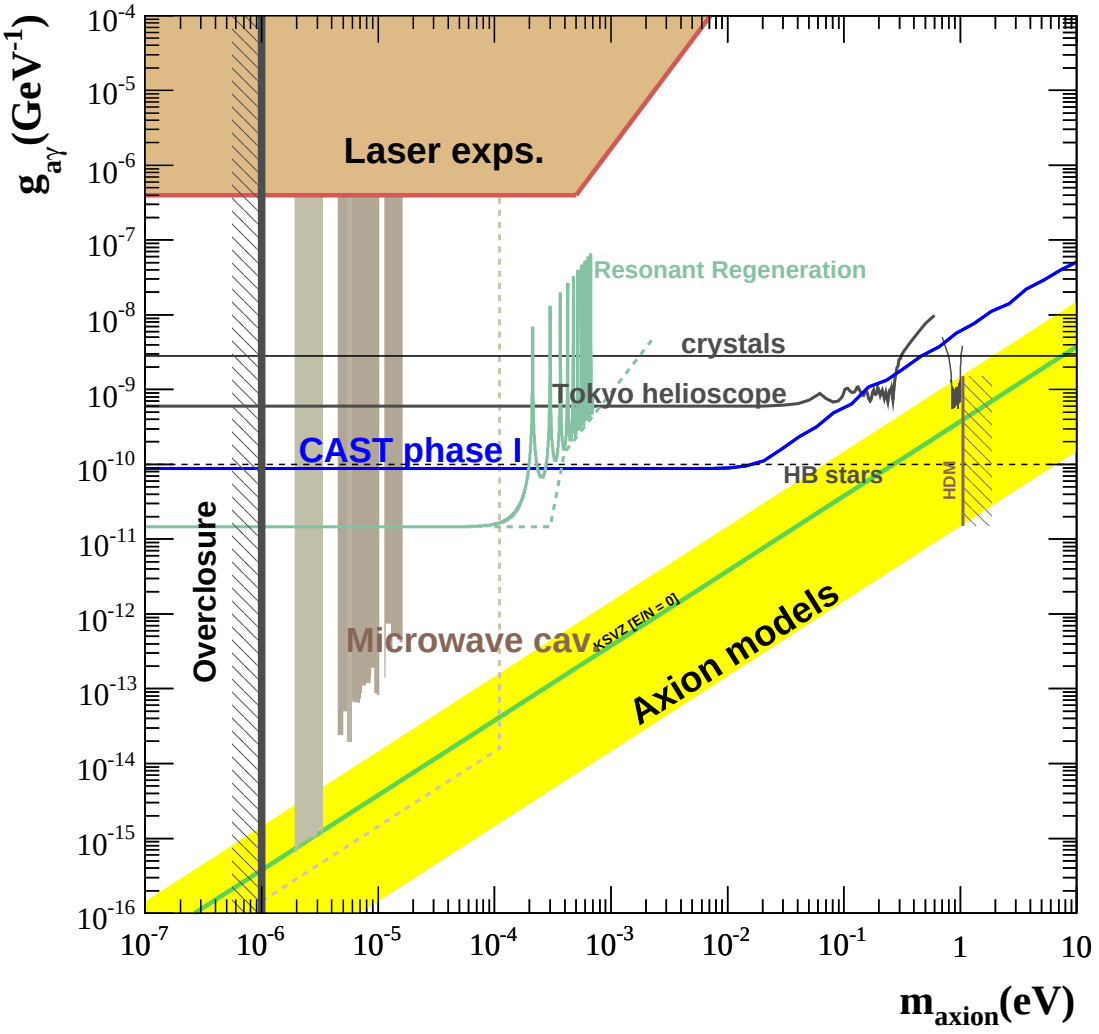

Figure 2.6: Excluded regions in axion parameter space. The comparison of these excluded regions give an idea about the discovery potential of different experimental attempts. Predictions by axion models and theoretical constraints are included as well. Picture from [24].

3. The CAST Experiment

This chapter is dedicated to the presentation of the CAST experiment and its actual design. The main focus will be on the X-ray detectors, especially the X-ray telescope and the CCD[1] camera, followed by a short summary on measurements carried out so far and their results. For a more detailed description see Ref. [42, 43] and references therein.

3.1 Experimental Setup

CAST is a helioscope (cp. Sec. 2.4.4) which demands the need to have a movable magnet in order to be able to track celestial objects as they move across the sky. The mobility of the used LHC[2] prototype dipole magnet is assured by a turntable at one end of the girder. The other end of the magnet is supported by lifting screws that enable vertical movement. The horizontal movement is realised by the fact that the lifting screws are mounted on a trolley driving on rails. For a schematic drawing of the CAST experiment see Fig. 3.1.

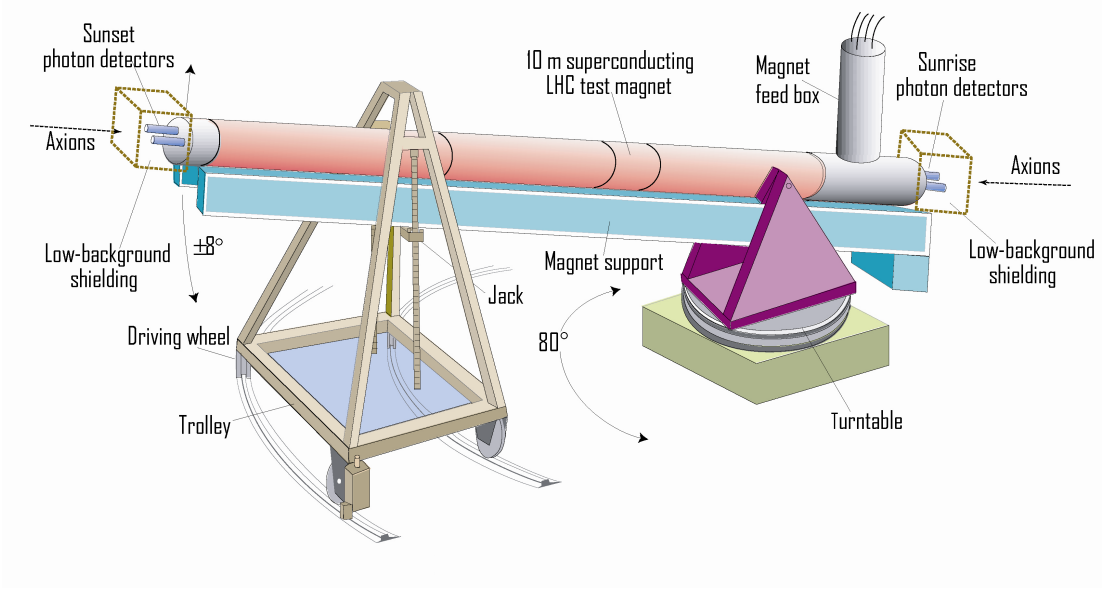

Figure 3.1: Schematic drawing of the CAST experiment. Figure courtesy of Dr. Silvia Borghi.

[1] Charge Coupled Device
[2] Large Hadron Collider

The vertical movement of the magnet is limited to $\pm 8^\circ$ mainly due to cryogenic constraints. Since the sun is only close to the horizon for certain azimuth angles, a horizontal movement within the range of 47° to 126° in azimuth angle is sufficient. Additional observation time can be gained by using the axion to photon conversion volume from both sides. During sunrise a Micromegas[3] detector and the CCD are used whereas during sunset the Time Projection Chamber[4] (TPC), mounted on the opposite side of the magnet, is operated.

3.1.1 The Magnet and the Vacuum System

The Magnet

The magnet used for axion to photon conversion is a decommissioned LHC prototype with an effective length of 9.26 m and two magnet bores with 43 mm diameter each (see Fig 3.2). The resulting cross sectional area is thus $A = 2 \times 14.522\ \mathrm{cm}^2$. In contrast to the dipole magnets currently used as bending magnets in the LHC, this prototype has not curved but straight magnet bores.

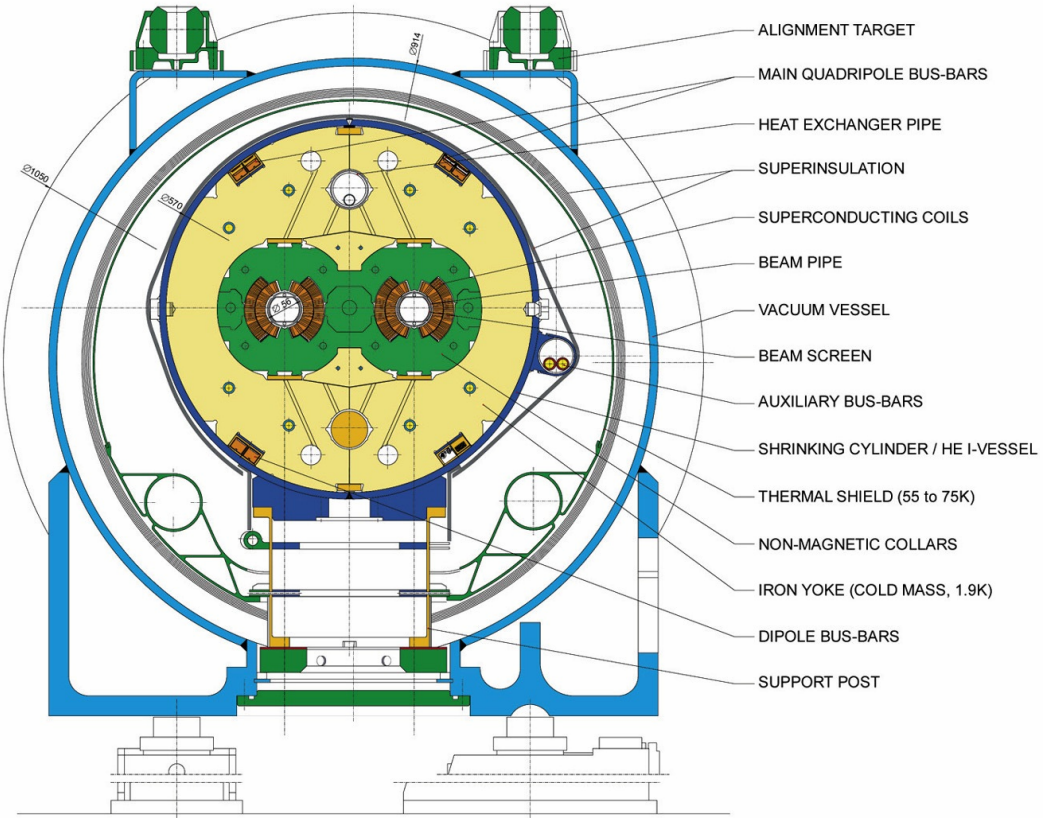

Figure 3.2: Cross section of standard LHC dipole magnets [44].

[3] MICROMEsh GAseous Structure.
[4] The TPC was replaced by 2 additional Micromegas detectors in 2007.

Although designed to provide a field strength of 8.4 T [45] the magnet is capable of providing 9.0 T corresponding to a current of 13.33 kA. In order to achieve such high currents, superconducting Niobium-Titanium coils are used. They are operated at a temperature of 1.8 K. Such low temperatures can be achieved by cooling with superfluid helium. Further details on cryogenics can be found in reference [46].

The Vacuum System

In phase I - when the magnet bores where operated with a vacuum of about 10^{-6} mbar - CAST was sensitive to axions with masses below 0.02 eV/c^2. Both beam pipes are interconnected and therefore have the same pressure which can be monitored by the pressure gauges (P6 and P7 in Fig 3.3) and is recorded by the Slow Control program.

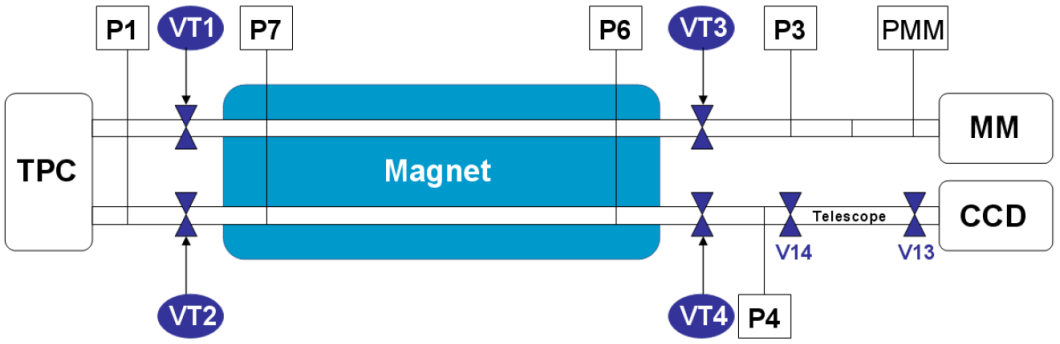

Figure 3.3: Scheme of the CAST vacuum system. Picture from [43].

To keep vacuum even if individual detectors have to be dismounted, each end of the magnet bores can be closed by a gate valve. VT1 and VT2 can seal off the magnet from the TPC, VT3 closes the connection between the magnet and the Micromegas detector and VT4 the one to the telescope and the CCD. Additionally these valves close automatically to protect the detectors in case of a quench or the magnet bores from contamination. The X-ray telescope itself can be sealed off by the valves V13 and V14 to protect its sensitive surfaces from contamination in the event of any kind of malfunction. Since the valves are not transparent to X-rays it is essential to make sure that they are open during data taking. The status of V13 and V14 therefore is checked at the beginning of each measurement as well as monitored by the telescope control PC. The status of VT1, VT2, VT3 and VT4 is kept under surveillance by the Slow Control program.

3.1.2 The Tracking System

The CAST magnet can be moved by use of two step motors. The actual position can be controlled by encoders whose values correspond to a local reference system and are automatically transformed into different kinds of coordinates by the tracking software. This program calculates the topocentric and galactic coordinates of objects of interest

for given local positions and times by using NOVAS[5]. In a second step the goal position of the magnet is calculated taking the actual position of the observed object into account. Using the values of the motor encoders the frequency and thus the speed for the motors are computed. This frequency is then send to the motors. The tracking program repeats the calculation described above once every minute and writes certain information such as time, coordinates, encoder values or motor frequencies to a logfile at the end of each cycle [47]. Fig. 3.4 provides a simplified scheme of this process. The tracking software can either be operated in *solar tracking mode* or in *galactic tracking mode* depending on whether the sun or any other object is going to be observed. The latter requires user defined target coordinates.

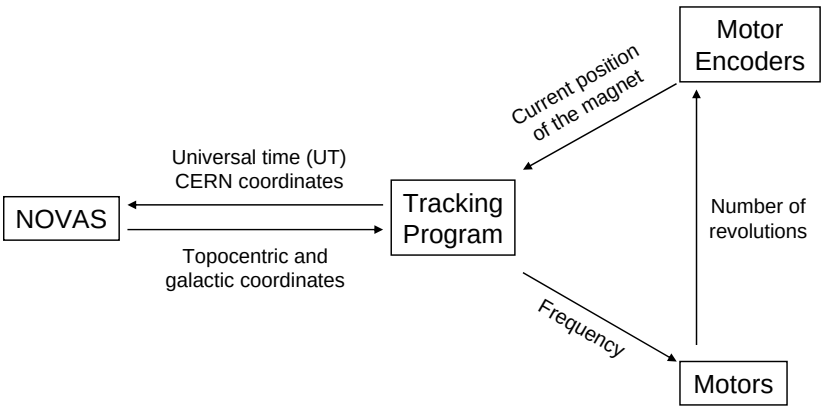

Figure 3.4: Schematic data flow of the tracking software.

Among the many variables stored in the logfile the pointing direction of CAST is included in terms of galactic longitude B and galactic latitude L. These values however just provide a crude estimate of the real pointing direction since they are calculated between the readout of the vertical encoder values and the readout of the horizontal encoder values. The time at which the calculation is carried out is refered to as *time* (cp. Fig 3.5).

The transformation from a local coordinate system to a galactic system is time dependent so that the precise time of transformation is needed. Therefore an accurate calculation of the pointing direction in terms of galactic coordinates can only be achieved by using the time *t.astro*, for which a new position of the magnet is calculated, along with the azimuth *AZ astr* and horizon angle *HA astr* at this specific time [47]. Using this set of time and topocentric coordinates a transformation into galactic coordinates giving the precise pointing direction is possible.

Even though CAST's pointing direction can be calculated precisely it is affected by uncertainties. The total tracking accuracy is a superposition of several factors and is estimated to be better than 0.01° [48]. Tab. 3.1 provides a decomposition of the individual contributions.

[5] Naval Observatory Vector Astrometry Subroutines.

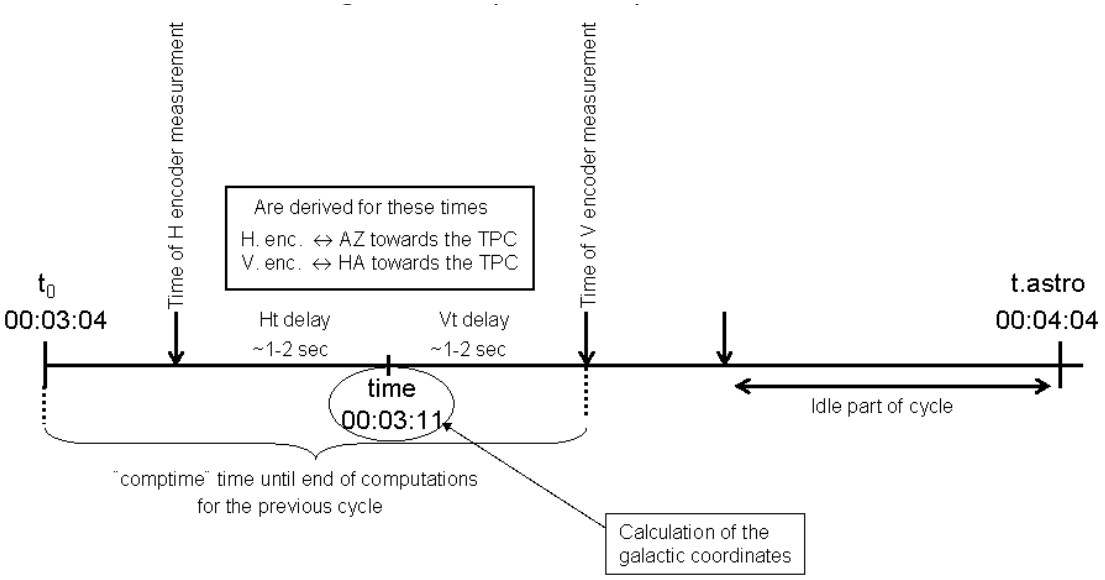

Figure 3.5: Scheme of the time of calculation. Galactic coordinates are calculated at *time* although a precise calculation needs to be carried out at *t.astro*. Figure courtesy of Dr. Silvia Borghi.

Error source	Typical value	Mamimum value
Astronomical calculations	0.002°	0.006°
Surveying measurements	0.001°	
Mathematical error in grid interpolation	0.002°	<0.01°
Horizontal encoder precision	$\sim$ 0.0014°	
Vertical encoder precision	$\sim$ 0.0003°	
Hysteresis	0.0034°	0.02°
Non-linearity of motor speeds	<0.002°	
Total	**<0.01°**	

Table 3.1: Possible Errors on Pointing Accuracy [48].

3.1.3 The Field of View

To know which pointing accuracy is needed to do reasonable observations, the field of view (FoV) of the X-ray telescope needs to be known. This holds even more if point sources are observed. The field of view can be calculated using

$$\phi = \arctan\left(\frac{r}{d}\right), \tag{3.1}$$

with r being the radius of the magnet bore and d denoting the distance from the beginning of the magnetic field to the telescope aperture (cp. Fig. 3.6).

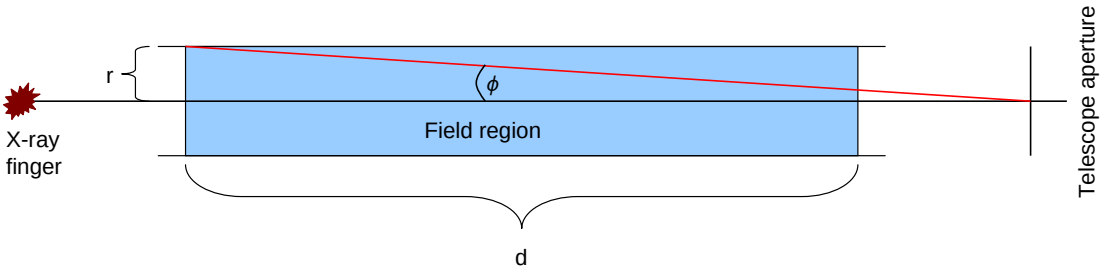

Figure 3.6: Definition of CAST's field of view.

This distance however is unknown so that information on the field of view has to be deduced indirectly. For alignment purposes an X-ray finger is installed at the opposite side of the CCD. The image these X-rays leave on the CCD - as can be seen in Fig. 3.7 - can be used to determine the field of view. The diameter of the X-ray spot is 44 pixels which corresponds to 14.18 arcmin and yields [49]

$$\text{FoV} = 2 \cdot \phi = 0.236°. \tag{3.2}$$

Similar results are obtained by crude estimations according to Eq. 3.1 using a lengt of $d \approx 10$ m.

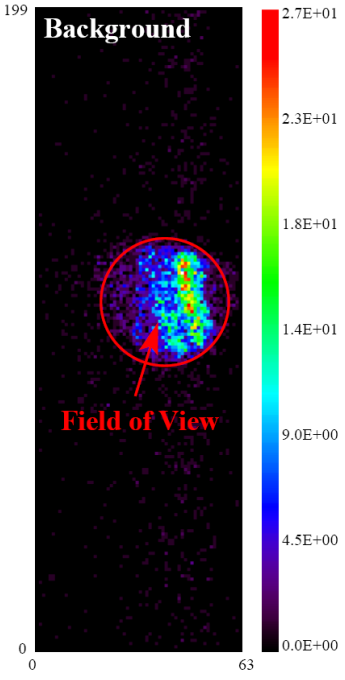

Figure 3.7: Intensity distribution as observed during X-ray finger measurements with the CCD. Figure courtesy of Dr. Markus Kuster.

3.1.4 Verification of Tracking Accuracy

Grid Measurements

The pointing accuracy can be verified by measuring the absolute position and pointing direction of the magnet by means of surveyor techniques. To exclude non-linearities in the movement of the magnet this measurement is not only carried out for a single but for several magnet positions representing the full range of movement. Thus for any position the accuracy can be determined by interpolation of the so-called grid measurements.

Filming of the Sun

The precision of the actual tracking can be directly measured by aligning a camera with the magnet and observe the sun. Twice a year - in March and September - it is possible to film the sun through a window in the wall of the CAST building. Since light, in contrast to axions, is refracted in the atmosphere the tracking software has to be modified slightly to take this deviation into account. The tracking program can run in tracking mode (no refraction) or filming mode (correct for refraction). The sun filmings performed in 2003 yielded an accuracy better than 0.05°. This result is basically limited by the precision of the camera alignment which is 0.05° itself. Within this uncertainty no additional deviation was observed. In 2004 the setup was improved resulting in a confirmed tracking accuracy of 0.02° for the measurments in March and September 2005. Further details can be found in [50].

Galactic Filming

Since the filming of the sun strictly speaking only verifies the pointing accuracy of the interplay of motors and tracking software in sun tracking mode, it is desirable to have an experimental confirmation of the pointing accuracy when the tracking software is used in galactic tracking mode as well. This can be achieved by filming a sufficiently bright star as it passes through the window, while the magnet is operated in galactic tracking mode. The same setup as in case of solar filming can be used. First results of such a galactic filming are expected soon.[6]

3.2 The X-Ray Detectors

In total three different X-ray detectors are used at CAST. Since only the analysis of data from the CCD detector is within the scope of this work, the two additional detectors are just briefly discussed.

3.2.1 Time Projection Chamber

Time Projection Chambers (TPCs) are combinations of Drift Chambers and Multi Wire Proportional Chambers (MWPC) as readout plane. Thus they detect particles by ionisation of single gas atoms followed by an avalanche process which occurs close

[6] Galactic filming will be the issue of the diploma thesis of Elisabeth Gruber. Release expected in February 2010.

to the anode where the electric field is sufficiently intense. This avalanche leads to a certain amount of charge large enough to be read out and further amplified.

The TPC designed for the CAST experiment has 48 anode wires with 20 μm diameter at 1.8 kV. The 96 cathode wires having a diameter of 100 μm are grounded. The drift field within the detection volume ($10 \times 15 \times 30$ cm^3) is 700 V/m. To let X-rays from the two evacuated magnet bores penetrate into the gas volume two mylar windows with a diameter of 6 cm each are located at the front side of the setup. Fig. 3.8 illustrates the layout of the TPC. The detection volume is filled with a mixture of 95 % argon and 5 % methane at atmospheric pressure. The detector efficiency is > 99 % for photons up to 6 keV. For higher energies it is decreasing so that photons at 11.5 keV are detected with an efficiency of roughly 50 %. The energy resolution is 12% at 5.9 keV and is monitored by use of an ^{55}Fe source in calibrations several times a day. For further details see [51].

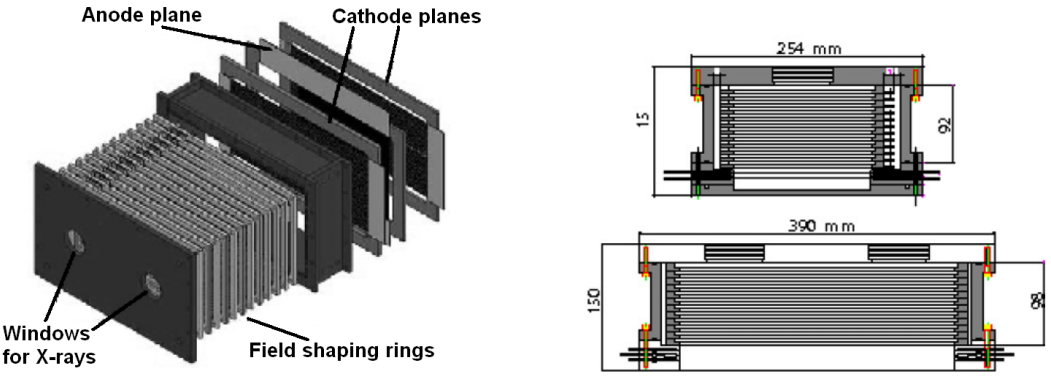

Figure 3.8: Left image: Layout of the TPC. The holes to hold the windows for X-rays coming from the magnet can be seen at the front end. Upper right image: Side view. Lower right image: Top view. All distances are given in millimeters [51].

Shielding

In order to reduce the background level active and passive shielding is installed. The innermost layer consists of 5 mm copper which is surrounded by 25 mm of lead, 1 mm of cadmium and 225 mm of polyethylene. To reduce radon contamination the setup is kept in a nitrogen atmosphere. Cosmic events are not spatially localised and can therefore be distinguished from X-rays emerging from the magnet bores. A background rate of 4.4×10^{-5} counts cm^{-2} s^{-1} keV^{-1} in the energy range from 1 to 10 keV can thus be achieved.

3.2.2 Micromegas

A MICROMEsh GAseous Structure (micromegas) is a detector for ionising particles. As a characteristic feature of micromegas the conversion volume is separated from the

amplification volume by a conducting micromesh. Two layers of microstrips are used as a two dimensional readout.

The micromegas detector used in CAST[7] in 2003 has an electric field of about 40 kV/cm between the micromesh and the readout plane separated only by 50 μm. This field causes an avalanche process leading to an amplification of about 10^4. Having an intensity of 1 kV/cm the field in the 25 mm long drift region is not strong enough to cause such processes. The anode plane has 192 x- and 192 y-strips with a pitch of 350 μm. The detector is operated with a mixture of 95 % argon and 5 % isobutane. To keep the leak rate to the vacuum inside the magnet low and to assure transparency for X-rays at the same time, two windows between detector and magnet bore are used. The first window is aluminised and serves as a cathode for the drift field. It has to stand a pressure difference of around 1 bar and is therefore supported by a strongback. The region between the windows is pumped down to roughly 10^{-3} mbar. Fig. 3.9 provides a schematic view of the detector. The consistent use of low radiation materials allows the background rate to be at 5×10^{-5} counts cm^{-2} s^{-1} keV^{-1} in the energy range from 0.6 keV to 10 keV. The energy resolution is 14 % at 5.9 keV and the detector efficiency above 50 %. Further details on the micromegas detector can be found in [52].

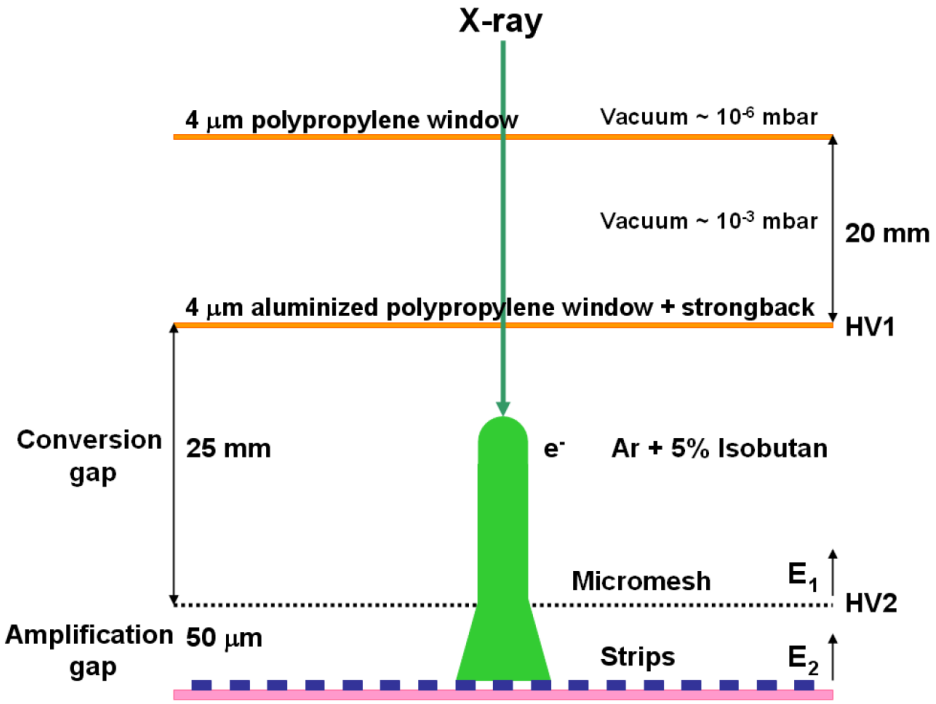

Figure 3.9: Working principle of micromegas detectors. More detailed specifications such as geometry and gas mixture refer to the detector used at CAST in 2003. Picture taken from [43].

[7]The micromegas detectors are changed quite frequently during shutdown periods. The specific features therefore might vary slightly.

3.3 The X-Ray Telescope and CCD Detector

The third detector used at CAST is a CCD detector with an X-ray telescope as imaging device. By focusing X-rays coming from the magnet bore of 14.5 cm^2 aperture to a spot of about 6 mm^2 the background level can be reduced by two orders of magnitude. Another advantage is that the focusing device allows to determine the background level simultaneously with tracking of target objects which is important in case unknown axion sources located somewhere in the sky can not be excluded. This fact plays a vital role when separating data from background in case of galactic tracking (cp. Sec. 5.1.4).

3.3.1 The X-Ray Telescope

The X-ray telescope used at CAST is a Wolter type I telescope[8] which is a spare part of the failed ABRIXAS[9] space mission. It consists of 27 nested mirror shells with a focal length of 1600 mm. The surface of these shells is gold-coated and has a micro roughness of less than 0.5 nm. The telescope is subdivided into 6 sectors with a supporting structure connecting them. The diameter of the innermost shell is 76 mm, the diameter of the outermost shell is 163 mm. The aperture of CAST is only 43 mm in diameter such that just a small fraction of the telescope is illuminated (cp. Fig. 3.10). Therefore the connection is done in a way that only one of the telescope sectors is used. To determine which sector provides the best results, a calibration measurement was done at the PANTER test facility in Munich [53].

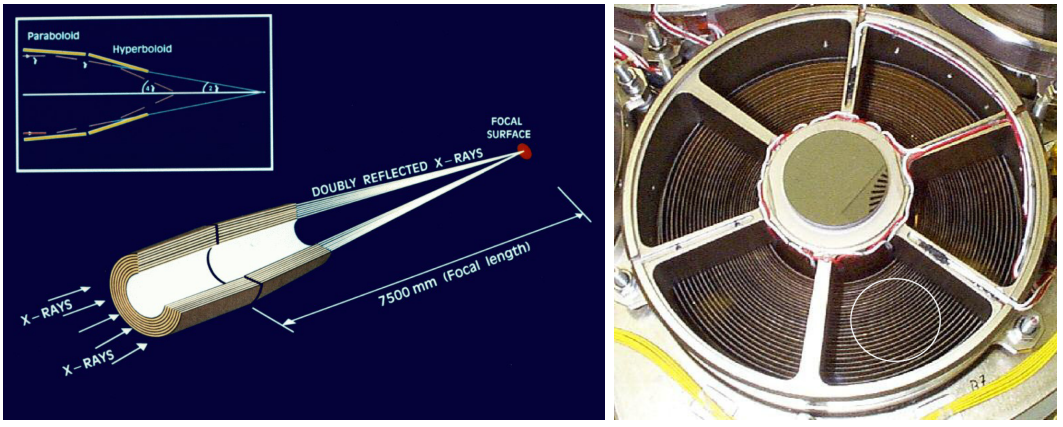

Figure 3.10: Left image: Wolter I type telescopes [54]. Right image: Front view of the X-ray telescope. The circle indicates the size and position of the magnet bore [53].

Effective Area

The effective area of a telescope is one of its important performance parameters since the transmission efficiency can be calculated to be the ratio of effective area and the aperture. Efficiency is a function of the off-axis angle and the photon energy. The

[8] Wolter type I means that parabolic mirrors are followed by hyperbolic ones where both reflections take place at the inner side of the mirrors. Compare Fig. 3.10.

[9] A BRoad-band Imaging X-ray All-sky Survey.

photon loss due to an increasing off-axis angle is also referred to as vignetting, which is energy dependent. Both vignetting for photon energies of 1.5 keV and effective area for on-axis observation where determined at PANTER. Results are plotted in Fig. 3.11 and 3.12.

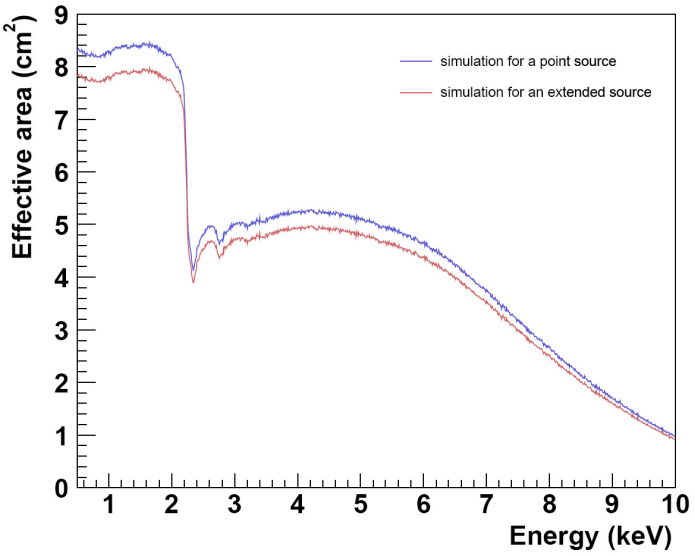

Figure 3.11: Effective area of the telescope. The blue line shows the effective area for point sources whereas the red line illustrates the effective area for extended objects like the sun [43].

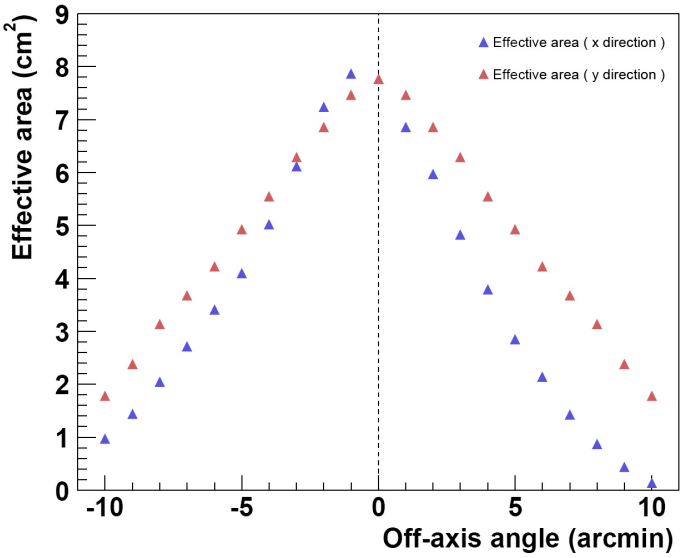

Figure 3.12: Vignetting effect on the effective area for photon energies of 1.5 keV [43].

3.3.2 The CCD Detector

The Charge Coupled Device (CCD) used as detector in combination with the X-ray telescope is of the same type as used in the XMM-Newton[10] space mission. It has 200×64 pixels with a pixel size of $150 \times 150\,\mu\text{m}^2$ each resulting in a total surface of about $1 \times 3\ \text{cm}^2$. The sensitive thickness is 280 μm. In order to reduce the noise level as well as the dark current[11] the detector is cooled down to temperatures of $-130°$ C. For details on the CCD the reader is referred to [53] and [55].

Background

Background reduction is achieved by placing a 1 cm thick layer of low activity copper around the CCD chip. An aperture hole towards the telescope is kept open. First background measurements in 2003 yielded a flat distribution besides a prominent peak in the region from 7 keV to 9 keV (cp. Fig. 3.13) which turns out to be the Cu-K$_\alpha$ line originating from the shielding itself.

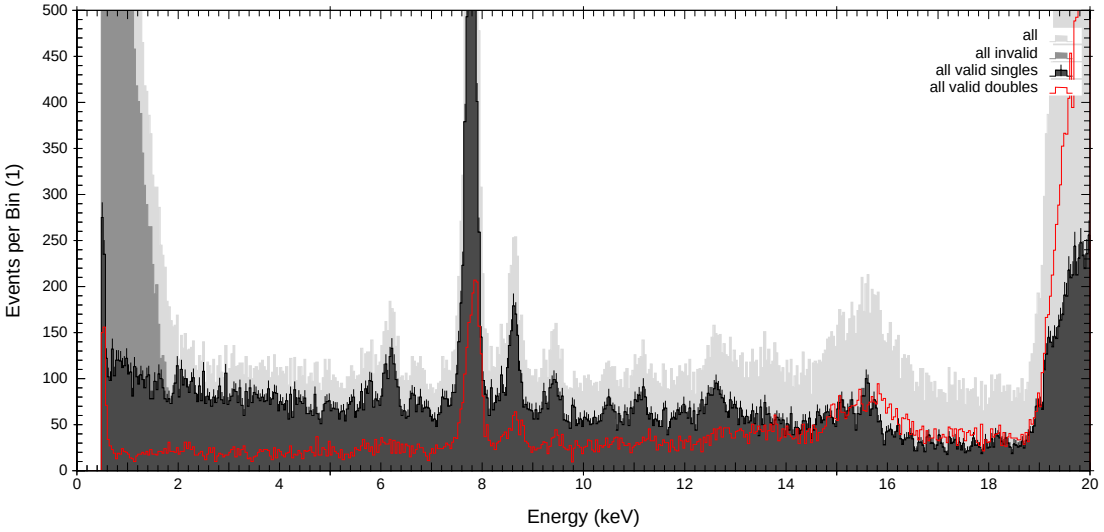

Figure 3.13: Background spectrum of the CCD detector in 2003. The total background, valid single events and invalid events are marked by different shades of gray. Double events are denoted by the red line. The copper peak can be clearly identified between 7 and 9 keV.

Further studies revealed that the background originating from outside the detector is isotropic. No dependency on the position of the magnet relative to the walls of the hall was observed. The distribution in terms of lines and columns of the CCD was also investigated, yielding a (nearly) flat distribution in both cases. Further details can be found in [43].

Split Events

During the drift towards the potential minimum the charge carriers generated after the impact of a photon onto the CCD spread out. Depending on the actual size of the

[10] X-ray Multi-mirror Mission.

[11] Dark current refers to small currents that are registered even if the CCD is not illuminated.

pixels this leads to a certain number of so-called split events. Their charge is registered by up to four pixels. Valid signals thus come from single events, double events, triple events and quadruple events. This circumstance can be used to reject signals from cosmic muons moving parallel to the CCD plane. Such movement causes events with several illuminated pixels in a row. Fig. 3.14 shows all valid events as they appear on the CCD. Tab. 3.2 provides a typical percentage distribution of split events for pixel sizes of $150 \times 150\,\mu\mathrm{m}^2$.

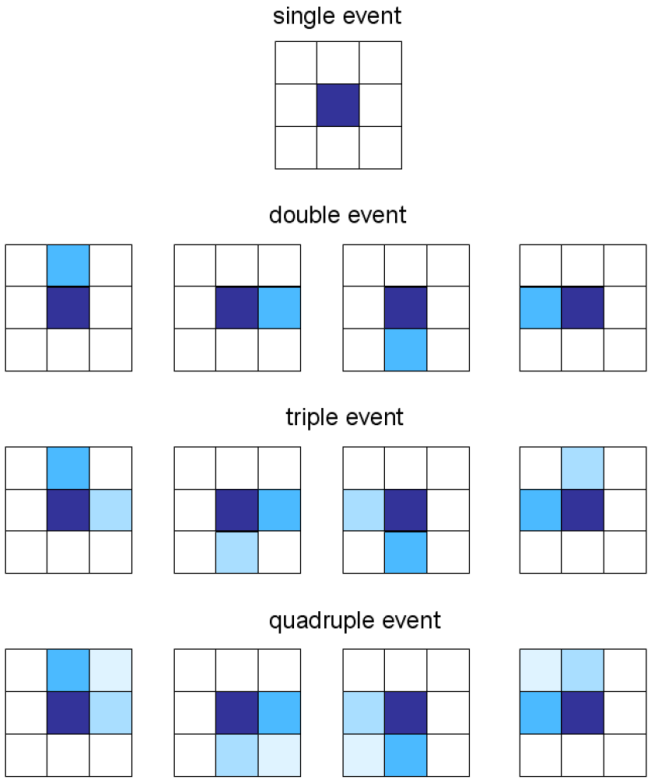

Figure 3.14: Illustration of all valid event types. The amount of charge collected is indicated by the darkness of the colour where the darkest pixel represents the one collecting the majority of the total charge [43].

Distribution type	Percentage
Single events	70
Double events	28
Triple events	1.6
Quadruple events	0.4

Table 3.2: Relative frequency of split events [43].

Bad Pixel

Pixels with dark currents way above average might occur due to problems during the manufacturing process. These pixels are referred to as hot or bad pixel. Since their position remains fixed and they easily can be identified by looking at the background distributions on the chip, these pixels can be excluded from the analysis.

Out-of-Time Events

The detector is permanently sensitive to incoming radiation which can lead to events with incorrectly allocated rows: For read-out the charges are shifted along the columns towards the anode so that events generated during this period accidentally are associated with rows the charge cloud never hit. Such events are referred to as Out-of-Time events (OoT). This effect can not be circumvented but corrected statistically. The fraction of Out-of-Time events f_{OoT} can be calculated for given read-out times $t_{\text{read-out}}$ and cycle times t_{cycle} [56].

$$f_{\mathrm{OoT}} = \frac{t_{\text{read-out}}}{t_{\text{cycle}} - t_{\text{read-out}}} = \frac{6.06\ \text{ms}}{71.7705\ \text{ms} - 6.06\ \text{ms}} = 0.092 \tag{3.3}$$

Calibration and Energy Resolution

The energy resolution ΔE, defined as the Full Width at Half Maximum (FWHM) of a peak, is given to be worse than

$$\Delta E = 2.355\, w \sqrt{\mathrm{ENC}^2 + \frac{F\,E}{w}}, \tag{3.4}$$

for silicon detectors. ENC (Equivalent Noise Charge) denotes the fluctuation of the read-out noise, w the pair creation energy and F the Fano factor. By using an ^{55}Fe source the CCD detector can be calibrated and the energy resolution determined. Such calibrations are done every day by means of a movable source, that can be brought to a position which allows to illuminate the detector. After finishing the calibration it is moved back to a shielded parking position in order not to contribute to the background. ^{55}Fe decays into an excited state of manganese by electron capture. The daughter nucleus in turn emits a photon with excitation-dependent energy. Thus two sharp lines (MnK_α and MnK_β) are observed in the spectrum (cp Fig. 3.15). By knowing the peak energies a calibration of the detector can be done. The FWHM of the K_α line is used to define the energy resolution which is of the order of 160 eV.

Quantum Efficiency

The quantum efficiency (QE) of the CCD detector denotes the percentage of incoming photons which produce an electron hole pair and thus can be detected. The QE was determined by measurements at the synchrotron radiation facilities in Berlin and Orsay. Fig. 3.16 shows the measured efficiency for the energy range from 0.15 keV to 15 keV, where absorption edges can be seen at 538 eV and 1840 eV. In the energy range from 0.5 keV up to 10 keV the quantum efficiency is larger than 90 %.

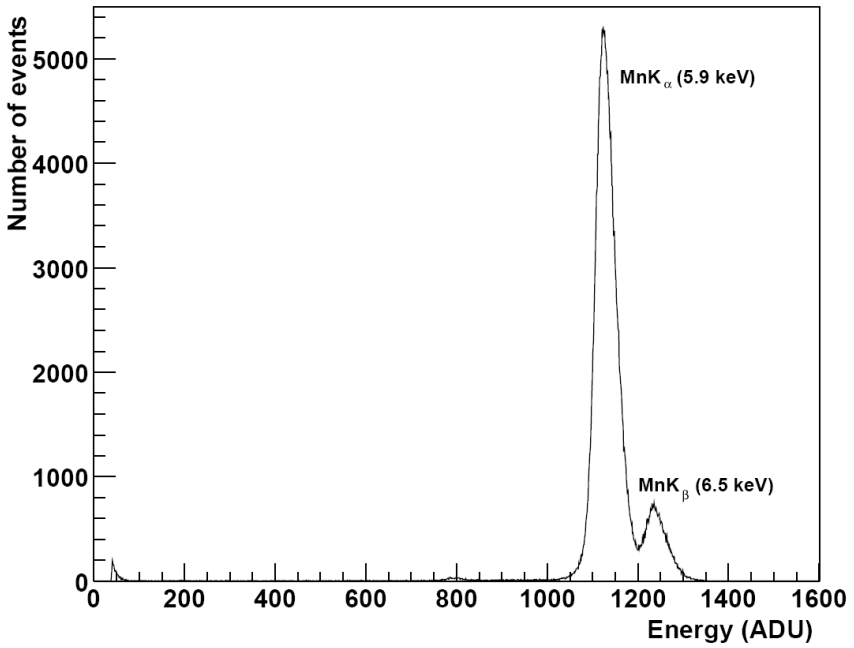

Figure 3.15: Spectrum of the ^{55}Fe source used for calibration of the CCD. The energy resolution is given as the FWHM of the K_α line [43].

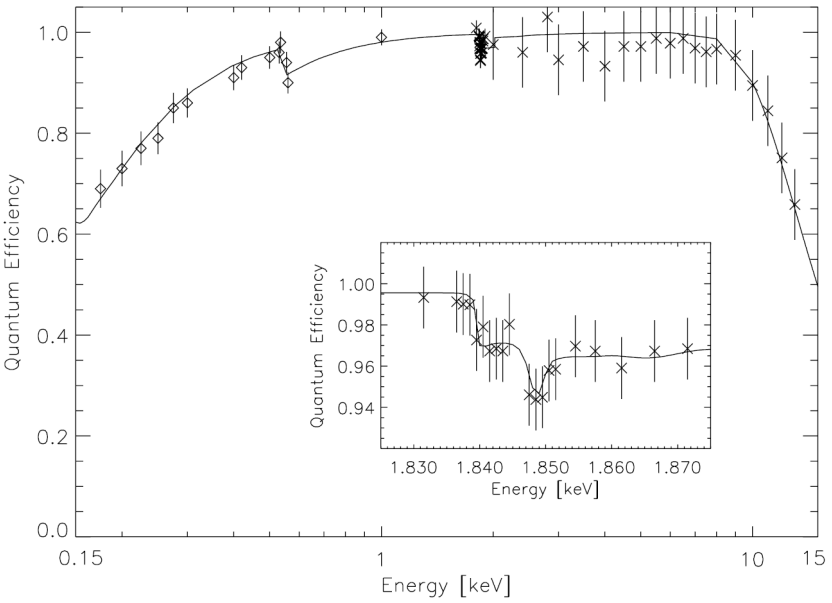

Figure 3.16: Quantum efficiency of the CCD. The embedded picture shows absorption edges around 1850 eV [55].

3.3.3 Combined Efficiency

Fig. 3.17 shows the combined efficiency of the telescope and the CCD. The black line illustrates the efficiency computed with spline interpolation in case a point source is observed. This efficiency is relevant for the analysis in Chapter 5. The efficiency gets worse in case a spread object like the sun is observed as the red line illustrates. Below 0.5 keV and above 10 keV the efficiency strongly depends on the interpolation method since no experimental data are available in this region. This fact is ilustrated by the black dotted line which represents the efficiency in case a point source is observed computed with linear interpolation.

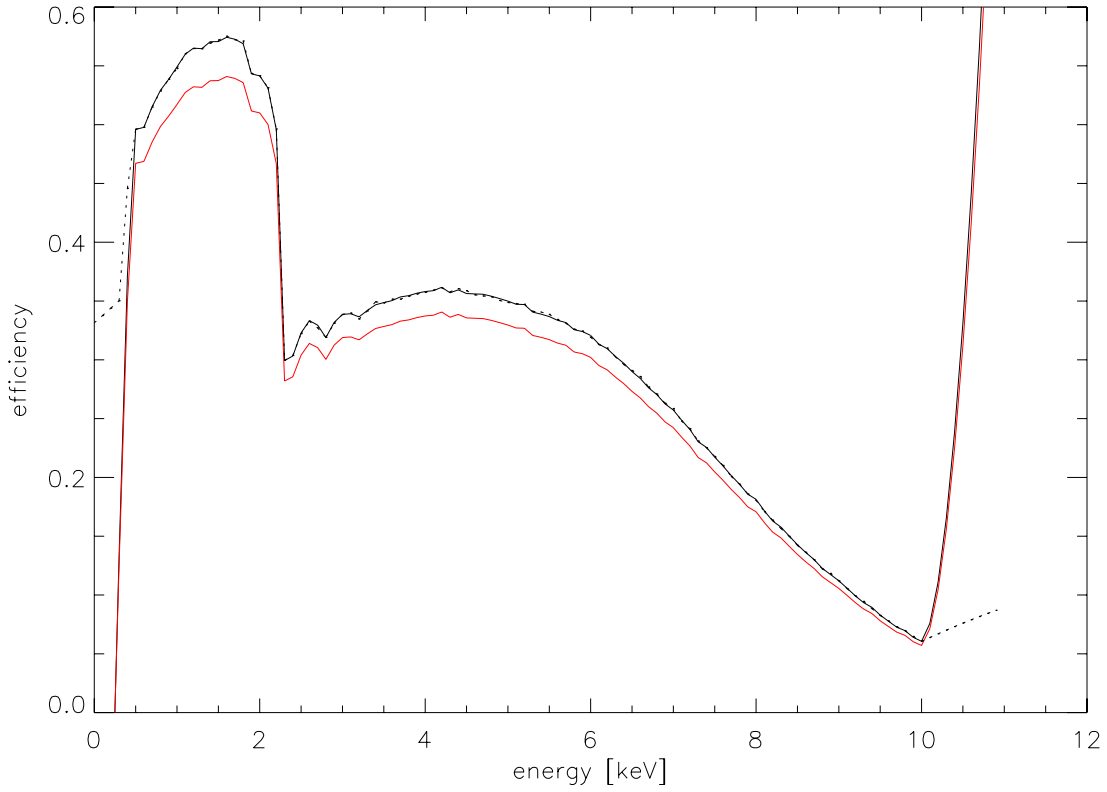

Figure 3.17: Combined efficiency of the telescope and the CCD. The black line denotes the efficiency computed with spline interpolation in case a point source is observed. Since no calibration data is available for energies larger than 10 keV or less than 0.5 keV the curves are misleading in this ranges.

3.4 Physics Program and Previous Results

The axion to photon conversion probability $P_{a\to\gamma}$ is given as

$$P_{a\to\gamma} = \frac{g_{a\gamma}^2 B^2}{4} \frac{1}{q^2 + \Gamma^2/4} \left[1 + e^{-\Gamma L} - 2e^{-\Gamma L/2}\cos(qL)\right], \tag{3.5}$$

with Γ being the damping coefficient, q denoting the momentum transfer, B the magnetic field intensity and L the length of the conversion volume. In vacuum the damping is zero such that by applying the coherence condition $qL \ll \pi$ one obtains

$$P_{a\to\gamma} = \frac{g_{a\gamma}^2}{4}(B \cdot L)^2. \tag{3.6}$$

This coherence condition limits the axion mass range a helioscope is sensitive to. Coherence can be restored for higher axion masses by using helium as a buffer gas which gives photons an effective mass of

$$m_\gamma = \sqrt{0.02\,\frac{p[\text{mbar}]}{T[\text{K}]}}\,\text{eV}/c^2. \tag{3.7}$$

This effective photon mass in turn corresponds to a narrow axion mass range in which the experiment is sensitive [57]. Since coherence can only be restored for the axion mass range

$$\sqrt{m_\gamma^2 - \frac{4\pi E_a}{L}} < m_a < \sqrt{m_\gamma^2 - \frac{4\pi E_a}{L}}, \tag{3.8}$$

a couple of measurements with different buffer gas pressures (and thus densities) have to be carried out in order to scan broad mass regions systematically. E_a denotes the axion energy. For further details on coherent conversion see [24] and references therein.

Consequently CAST was designed to be operated in two phases to be able to cover an axion mass range up to 1.2 eV/c^2 [**?**]. In phase I (2003 till 2004) the magnet bores were evacuated such that coherence was given for axion masses up to about 0.02 eV/c^2. In phase II helium is used as buffer gas. By using ^{4}He the coherence was restored for axion masses up to about 0.4 eV/c^2 in 2005 and 2006. Higher mass regions would have demanded higher pressures. This could not be achieved since the saturation pressure of ^{4}He would be exceeded in that case. Therefore ^{3}He - having a higher saturation pressure - was used from 2008 onwards[12].

[12] Phase II is expected to end in 2010.

The analysis of phase I yielded an upper limit on the axion to photon coupling constant of [43]

$$g_{a\gamma} < 8.8 \times 10^{-11}\ \text{GeV}^{-1} \text{ for } m_a \lesssim 0.02\ \text{eV}/c^2, \tag{3.9}$$

at 95 % condidence level whereas a typical upper limit on the coupling constant of

$$g_{a\gamma} \lesssim 2.17 \times 10^{-10}\ \text{GeV}^{-1}, \tag{3.10}$$

was extracted for axion masses between 0.02 eV/c^2 and 0.4 eV/c^2 [15, 24].

4. Galactic Objects

In the following the three celestial objects which were observed by CAST are introduced. The galactic centre and Scorpius X-1 were tracked using the CCD and the Micromegas detector, whereas the Crab nebula was observed with the TPC. Since only data from the CCD detector is analysed in the scope of this work, the Crab nebula is only touched briefly.

4.1 Scorpius X-1

Scorpius X-1 (Sco X-1), which later was identified to be the visible object V818 Sco[1], is the brightest X-ray source (cp. Fig 4.1) in the sky for X-rays below 20 keV apart from the sun. It is a low mass X-ray binary with a neutron star of about 1.4 solar masses and a donor star of about 0.42 solar masses [58]. The strong X-ray emission is due to the fact that matter from the donor star is accelerated and accreted by the neutron star. A by-product of this acceleration is electromagnetic radiation with energies corresponding to the strength of the acceleration. The fact that the donor star is orbiting around the neutron star leads to an intensity variation of one magnitude[2] with a period of 18.9 hours. Sco X-1 is situated in a distance[3] of (2.8 ± 0.3) kpc and has an X-ray output of 2.3×10^{31} W [59]. Thus the X-ray flux on earth can be computed to be

$$\phi_{\mathrm{X,\,Sco}} = (2.4 \pm 0.3) \times 10^{-10} \frac{\mathrm{W}}{\mathrm{m}^2}. \tag{4.1}$$

The error on the flux calculation results from the uncertainty on the distance. Tab. 4.1 summarises the coordinates of Sco X-1. For more details on celestial coordinate systems see Appendix A.

Equatorial coordinates		Galactic coordinates	
Right ascension	$16^{\mathrm{h}}\,19^{\mathrm{m}}\,55.07^{\mathrm{s}}$	Latitude (B)	23.778°
Declination	$-15°\,38'\,24.8''$	Longitude (L)	359.100°

Table 4.1: Coordinates of Sco X-1 at equinox J2000.0.

[1] V818 Sco was known long before the X-ray source Sco X-1 was discovered. Both names are used nowadays depending on the context.

[2] Magnitudes are used in astronomy to characterise the apparent brightness of stars. The difference in magnitude $m_1 - m_2$ between two objects with fluxes S_1 and S_2 is defined as $m_1 - m_2 = -2.5 \cdot \log_{10} S_1/S_2$. The apparent brightness of *Vega* ($m_{\mathrm{Vega}} = 0.03$) is used as a reference.

[3] 1 pc is approximately 3.26 light years.

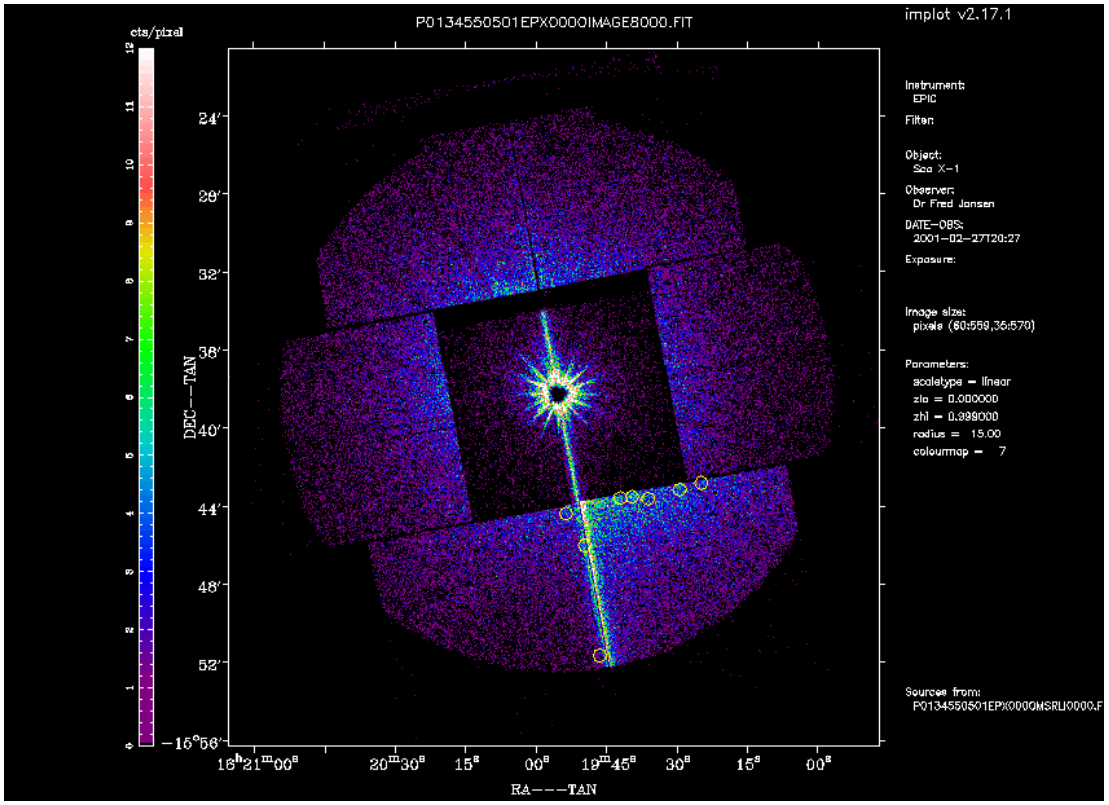

Figure 4.1: X-ray image of Sco X-1 obtained by the EPIC-MOS camera on board the XMM-Newton satellite. The small circles below the centre mark the position of identified X-ray sources nearby.

4.2 The Galactic Centre

The centre region of the Milky Way is not visible since it is hidden by an opaque dust cloud but can be studied with radio observatories and X-ray telescopes. From these observations it is known that the inner region of the galaxy contains thousands of stars. Most of them are old main sequence stars but besides that also a lot of massive stars are present. This inner region has a radius of around 1 pc which, for a given distance of 7.62 kpc, corresponds to an angle of 0.015°. This ensemble therefore is completely within the field of view of CAST which is 0.236°. The galactic centre contains the complex radio source Sgr A, which in turn contains the very intense radio source Sgr A*. This object coincides with a supermassive black hole and is the rotational centre of the Milky Way. An X-ray image of the galactic centre region can be seen in Fig. 4.2.

Sagittarius A

Sgr A consists of three components: The supernova remnant Sgr A East, the pseudo-spiral structure Sgr A West and the radio source Sgr A*. These parts are not spatially separated and overlap. They have different sizes and ages. Sgr A East for example is believed to have formed in a supernova just 10,000 to 100,000 years ago, which is very

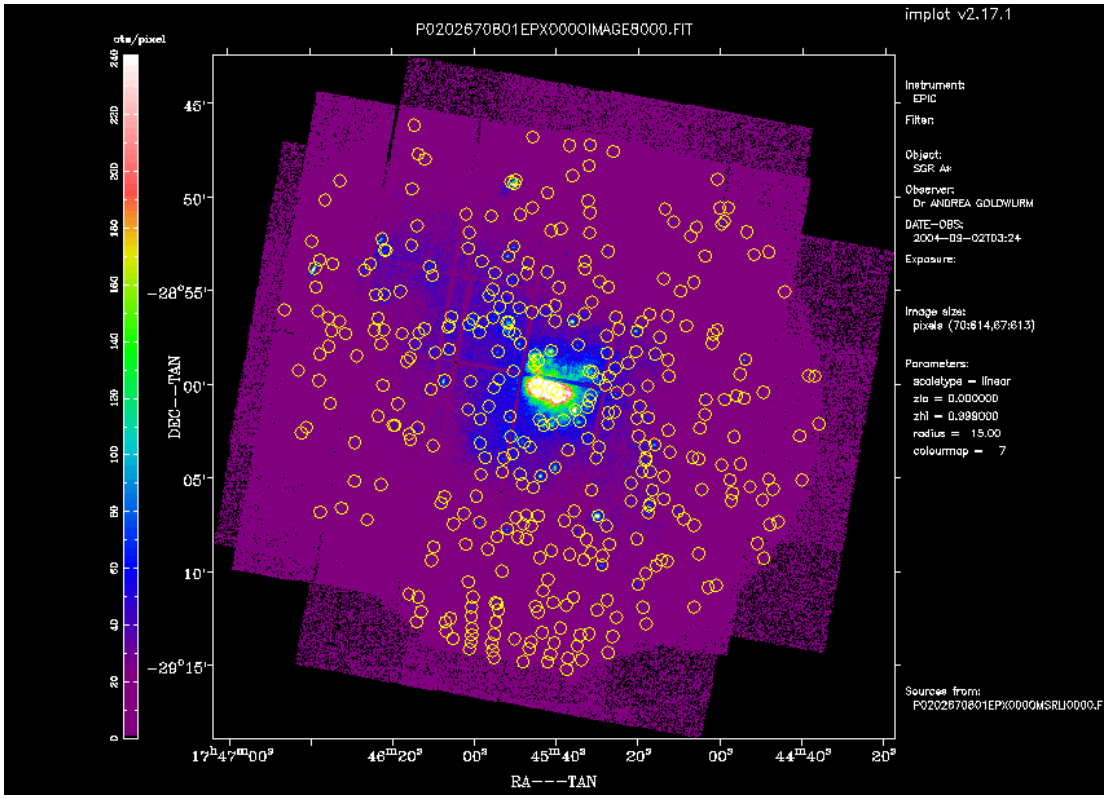

Figure 4.2: X-ray image of Sgr A* obtained by the EPIC-pn camera on board the XMM-Newton satellite. The small circles mark the position of X-ray sources nearby.

young on cosmic time scales. The total size of Sgr A is of the order of light years. Sgr A West is sometimes referred to as spiral structure, although the spiral appearance is just a consequence of the specific angle of view that observation from earth implies. Sgr A West itself can be decomposed into several gas and dust clouds orbiting around Sgr A*.

The satellite *Chandra* observed an X-ray component in the spectrum of Sgr A that implies the presence of a diffuse hot, thermal plasma at a temperature of $\sim 9 \times 10^7$ K. This temperature corresponds to energies of ~ 8 keV. The origin of this plasma is still uncertain because no known energy source is able to heat the plasma as it would be necessary to achieve such temperatures.

Sagittarius A*

Latest measurements revealed that the radio source Sgr A* has a diameter of just 44 million kilometers. Taking its mass of around 4.31 million solar masses [60] into account yields that Sgr A* must be a super massive black hole. Even though no direct evidence[4] for a black hole was found so far no object of this size and mass can be imagined that

[4] A direct evidence for a black hole is to find a certain mass within a confined space with a radius less than the corresponding Schwarzschild radius.

would not decay into a singularity on a time scale less than the age of the Milky Way [61]. Strictly speaking, Sgr A* is not the black hole itself since black holes do not radiate. If Sgr A* was arranged concentrically around the black hole, an amplification of the emission due to gravitational lensing would be expected, but is not observed. Therefore it is believed that Sgr A* is part of the accretion disc. Nevertheless it can be used to determine the properties of the central black hole of the Milky Way. X-ray flares with luminosities up to 160 times higher than the quiescent luminosity have been reported. These flares vary in duration and features [62]. For historic reasons Sgr A* is not at the centre of the galactic coordinate system but slightly aside. Tab. 4.2 summarises its coordinates.

Equatorial coordinates		Galactic coordinates	
Right ascension	$17^{\mathrm{h}}\,45^{\mathrm{m}}\,40.045^{\mathrm{s}}$	Latitude (B)	-0.046°
Declination	$-29°\,0'\,29.7''$	Longitude (L)	359.944°

Table 4.2: Coordinates of Sgr A* at equinox J2000.0.

4.3 Crab Nebula

Another prominent X-ray source is the Crab nebula situated approximately 2 pc away. For energies above 30 keV it is even the strongest source in the sky. Its total luminosity is 75,000 times larger than the one of the sun. The Crab nebula is the remnant of the supernova SN1054 which occurred in the year 1054 as reported by far eastern and arabian astronomers. The nebula itself is expanding and contains a spinning neutron star with a spin rate of 30 revolutions per second. The strong magnetic field of neutron stars focuses emitted radiation into narrow beams pointing in the direction of the magnetic poles. If the magnetic axis happens not to coincide with the rotational axis an observer detects regularly pulsating emission from the neutron star as the radiation beams pass by. Due to their apparently pulsating nature such neutron stars are referred to as *pulsars*. X-ray emission is affected by this rotational behavior as well. Even though the Crab pulsar has a mass of more than 1.9 times the solar mass, it is a very dense and compact object with a radius of just 14-15 km [63].

4.4 X-Ray Spectra and Light Curves

4.4.1 Light Curves

Galactic objects were tracked by CAST in the period from the beginning of September until the end of October 2003. For this period light curves are available from the All Sky Monitor (ASM) on board the Rossi X-ray Timing Explorer (RXTE) satellite[5]. Fig. 4.3 and Fig. 4.4 provide light curves of Sco X-1 and Sgr A. As frequently done in X-ray astronomy, the flux is normalised to the one of the Crab nebula. Each point represents an observation of 90 minutes. The length of the bars indicate statistical and systematical uncertainties.

[5] http://xte.mit.edu/asmlc/ASM.html

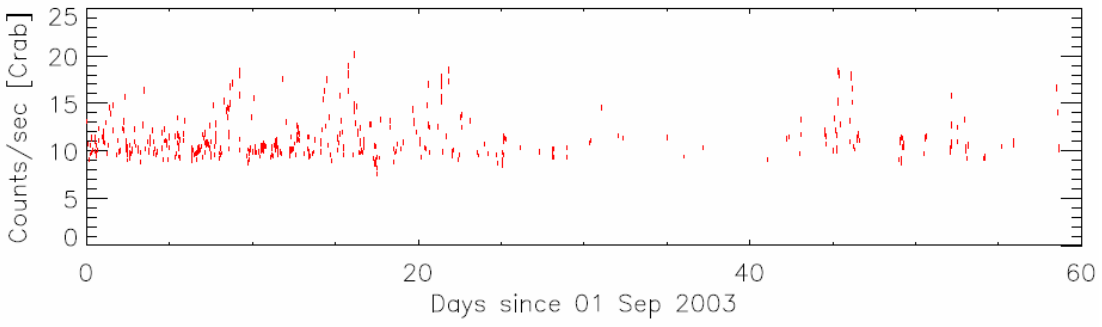

Figure 4.3: Light curve of Sco X-1 from the beginning of September until the end of October 2003. The flux is normalised to the Crab Nebula. Figure courtesy of Dr. Michael Pivovaroff.

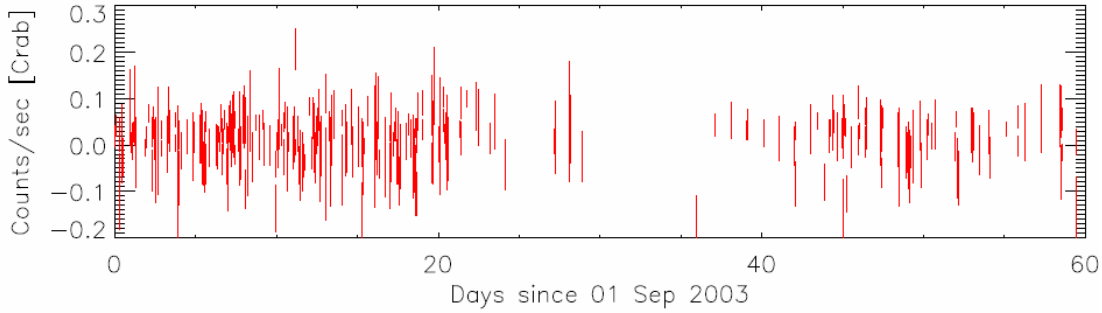

Figure 4.4: Light curve of Sgr A from the beginning of September until the end of October 2003. The flux is normalised to the Crab Nebula. Figure courtesy of Dr. Michael Pivovaroff.

4.4.2 X-Ray Spectra

The XMM-Newton Science Archive (XSA)[6] provides the opportunity to create customised X-ray spectra for any object observed by the XMM-Newton satellite. Data from the EPIC MOS[7]-CCD and EPIC pn-CCD, which is identical in construction to the CCD used in CAST, can be obtained. In order to get spectra the user has to define background and signal regions on a given X-ray image. The data is than processed by the system and raw files containing calibration curves, uncalibrated spectra and so on are send to the user. To get the actual spectra the data has to be processed with the help of the XSPEC software which is part of the HEAsoft[8] package NASA[9] offers. The possibility to fit different predefined models to the spectrum is given as well. Fig. 4.5

[6] http://xmm.esac.esa.int/xsa/
[7] European Photon Imaging Camera Metal Oxide Semi-conductor.
[8] High Energy Astrophysics software.
[9] National Aeronautics and Space Administration.

and Fig. 4.6 show the X-ray spectra of Sco X-1 and Sgr A. Scorpio X-1 is a single X-ray source, so that a power law with absoption due to interstellar hydrogen such as

$$I(E) = k\, e^{-\alpha}\, e^{-n_H \sigma(E)}, \tag{4.2}$$

can be fitted to its spectrum as a first approximation. $I(E)$ is the intensity, k a normalisation factor, α the photonindex, n_H the hydrogen column density and $\sigma(E)$ is the energy dependent electron-photon scattering cross section. The resulting parameters are

$$\begin{aligned} n_H &= 0.2385 \times 10^{22}\ \mathrm{cm}^{-2}, \\ k &= 3.2789\ \mathrm{keV}^{-1}\ \mathrm{cm}^{-2}\ \mathrm{s}^{-1}, \\ \alpha &= 1.3572. \end{aligned}$$

The residuals of this fit are plottet along with the spectrum.

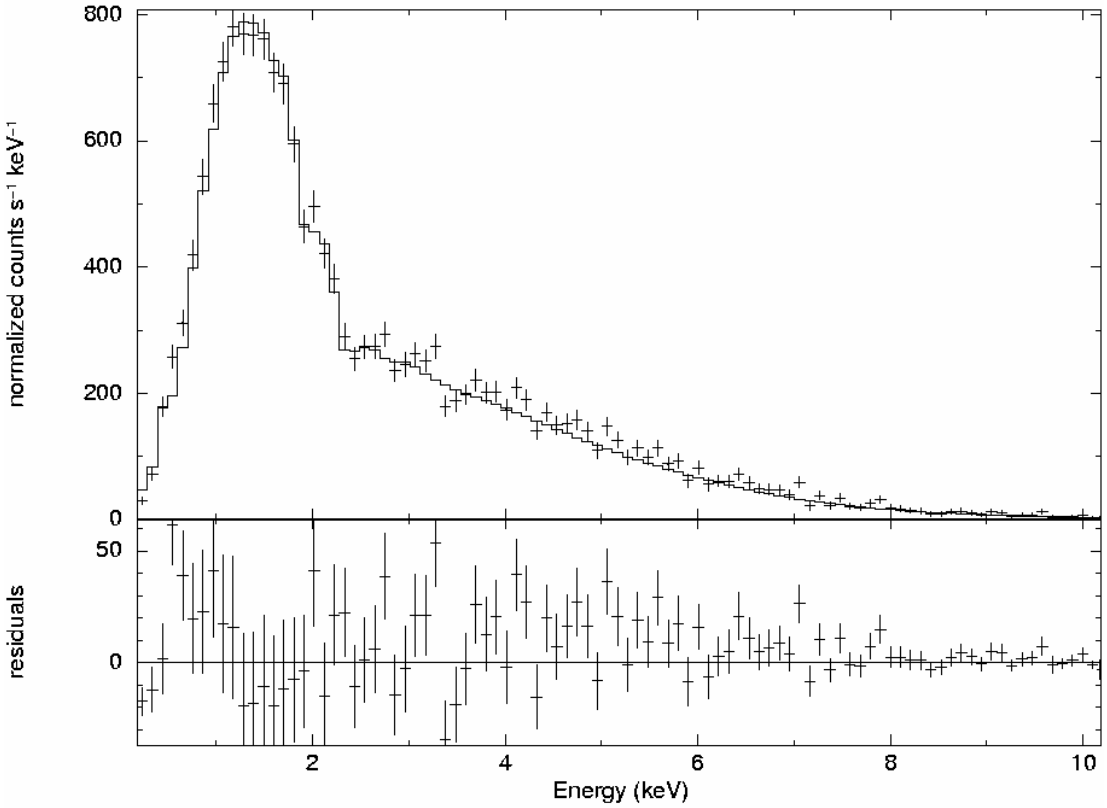

Figure 4.5: X-ray spectrum of Sco X-1. A power law including absorption by interstellar hydrogen is fitted to the data. The bin size is 0.05 keV. Residuals are plotted in the lower part. This spectrum is computed based on the X-ray image 4.1.

Several sources contibute to the spectrum of the galactic centre and parts of its origin are not understood so far. Therefore no resonable fit can be done since it is unclear which model to use (cp. Sec. 4.2).

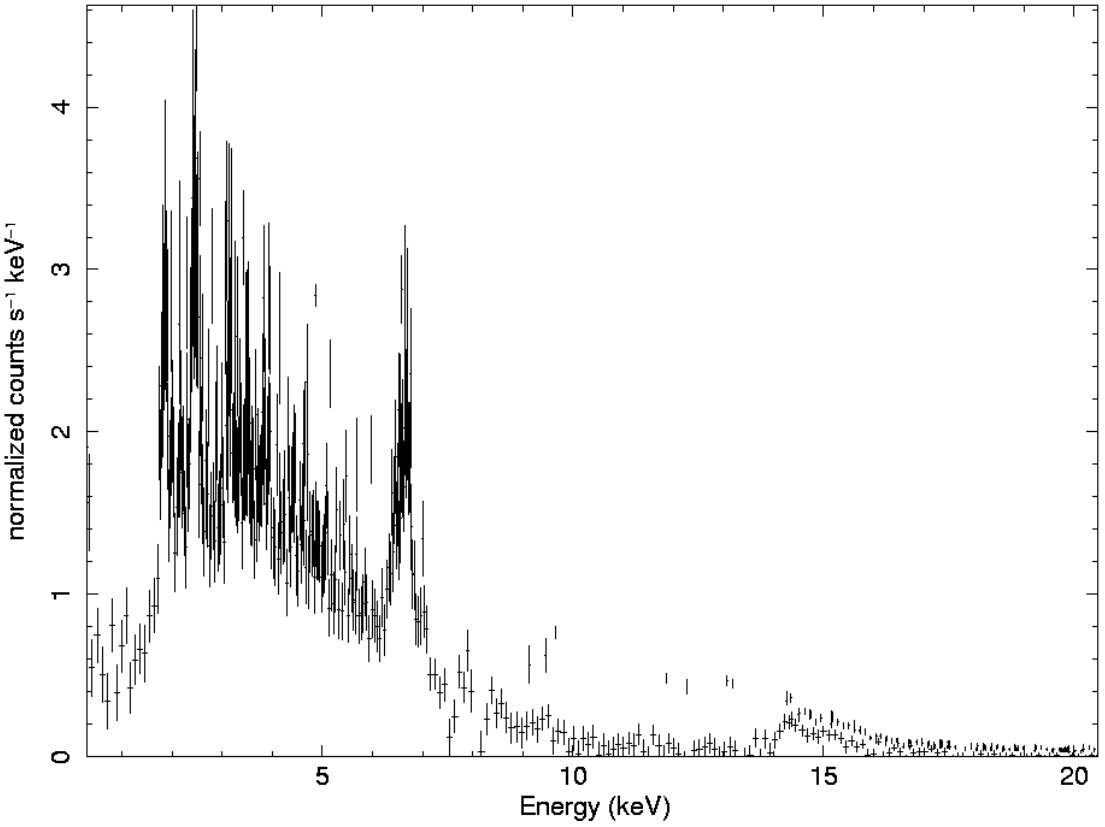

Figure 4.6: X-ray spectrum of Sgr A. Several iron emission lines form the prominent peak around 6.7 keV. The binning is done in a way that each bin is either 0.1 keV wide or that a variance of 5σ is given. The spectrum is computed based on the X-ray image 4.2.

5. Analysis of the Galactic Data

This chapter is dedicated to the analysis of the data taken during galactic trackings with the CCD detector at CAST in 2003. Since CAST was operated with evacuated magnet bores at the time all results obtained from these data refer to axions with masses below 0.02 eV/c^2.

The first half of this chapter is addressed to preliminary considerations that are needed to define reasonable conditions for data analysis. Since no signal above background was observed, an upper limit on the free parameter axion flux $\times$ coupling constant^2 ($\phi g_{a\gamma}^2$) is estimated by using the method of maximum likelihood in the second half. This estimation is done both for the data taken during observation of the galactic centre and for data from Scorpio X-1. The axion spectrum from these objects are treated as being flat or as having a shape like the corresponding X-ray spectra. Different background definitions are applied as well. In the last section the results are reviewed and an evaluation of the new insights gained by this analysis is carried out.

5.1 Preliminary Considerations

5.1.1 Energy Ranges

In principle the CCD chip used for data taking is sensitive to X-ray energies up to 20 keV. For the X-ray telescope however no calibration data for energies above 10 keV is available so that an upper limit for the investigated energy range is given (cp. Sec. 3.3.1). The lower end of this range is defined by a software threshold cutting away events with energies less than 0.5 keV. For solar analysis the data was binned using a binsize of 0.3 keV. To be consistent with this the same binsize is applied here leading to energy ranges that are always multiples of 0.3. In total, five different energy ranges are investigated:

- The maximum energy range from 0.5 to 9.8 keV.
- The maximum range with shifted lower boundary from 1.0 to 10 keV. A high noise rate is expected for low energies which suggests to cut away events with energies less than 1.0 keV.
- From further studies it is known that a prominent copper line is visible in the background spectrum around 8 keV (cp. Fig. 3.13). Therefore the maximum energy range is analysed without events having energies between 7.2 and 9.0 keV.
- To allow comparison to solar data, the range from 1.0 to 7.0 keV is investigated.

- A feature of special interest within the X-ray spectrum of Sgr A are the iron emission lines around 6.8 keV [64] which lead to an analysis of the range from 6.0 to 7.2 keV.

Tab. 5.1 summarises the investigated energy ranges.

Energy range [keV]	Relevant for analysis of
0.5 - 9.8	Sgr A, Sco X-1
0.5 - 9.8 without 7.2 - 9.0	Sgr A, Sco X-1
1.0 - 10.0	Sgr A, Sco X-1
1.0 - 7.0	Sgr A, Sco X-1
6.0 - 7.2	Sgr A

Table 5.1: Analysed energy ranges.

5.1.2 Using Different Galactic Coordinate Systems

Even though the CAST tracking software asks the user to insert galactic target coordinates with longitudes from 0° to 360°, an additional coordinate system (compare Appendix A) was used in case of observation of Sgr A. Therefore it is important to verify that data obtained with alternative[1] target coordinates (ReqL = -0.052)[2] can be analysed just as the data obtained with standard target coordinates (ReqL = 359.9).

In oder to compare the actual movement of the magnet, two plots of encoder values (Venc) versus time are compared. Each plot shows three trackings separated by two days. Times of galactic tracking can be clearly identified by rising curves. Lines on the left of the images represent trackings of Sco X-1 and Lines at the right trackings of Sgr A. The black curve in the upper part of Fig. 5.1 represents the pointing direction of the magnet using standard target coordinates. The red and blue lines in both parts as well as the black line in the lower part refer to the use of alternative coordinates.

The relative distances of the three individual lines (black, red and blue) in the upper and lower plot are the same. The offset is due to the annual modulation of the position of celestial objects that even affects trackings that are just two days apart. In case the pointing direction of the magnet depends on the coordinate system used, such similarity in the actual movement of the magnet is not expected. Similar comparisons were made with the horizontal encoder values resulting in the conclusion that the tracking software is able to deal with both types of target coordinates.

[1] The term "alternative" is misleading in this context since alternative coordinates are used more often than standard coordinates.

[2] ReqL is an acronym for requested longitude used by the tracking software.

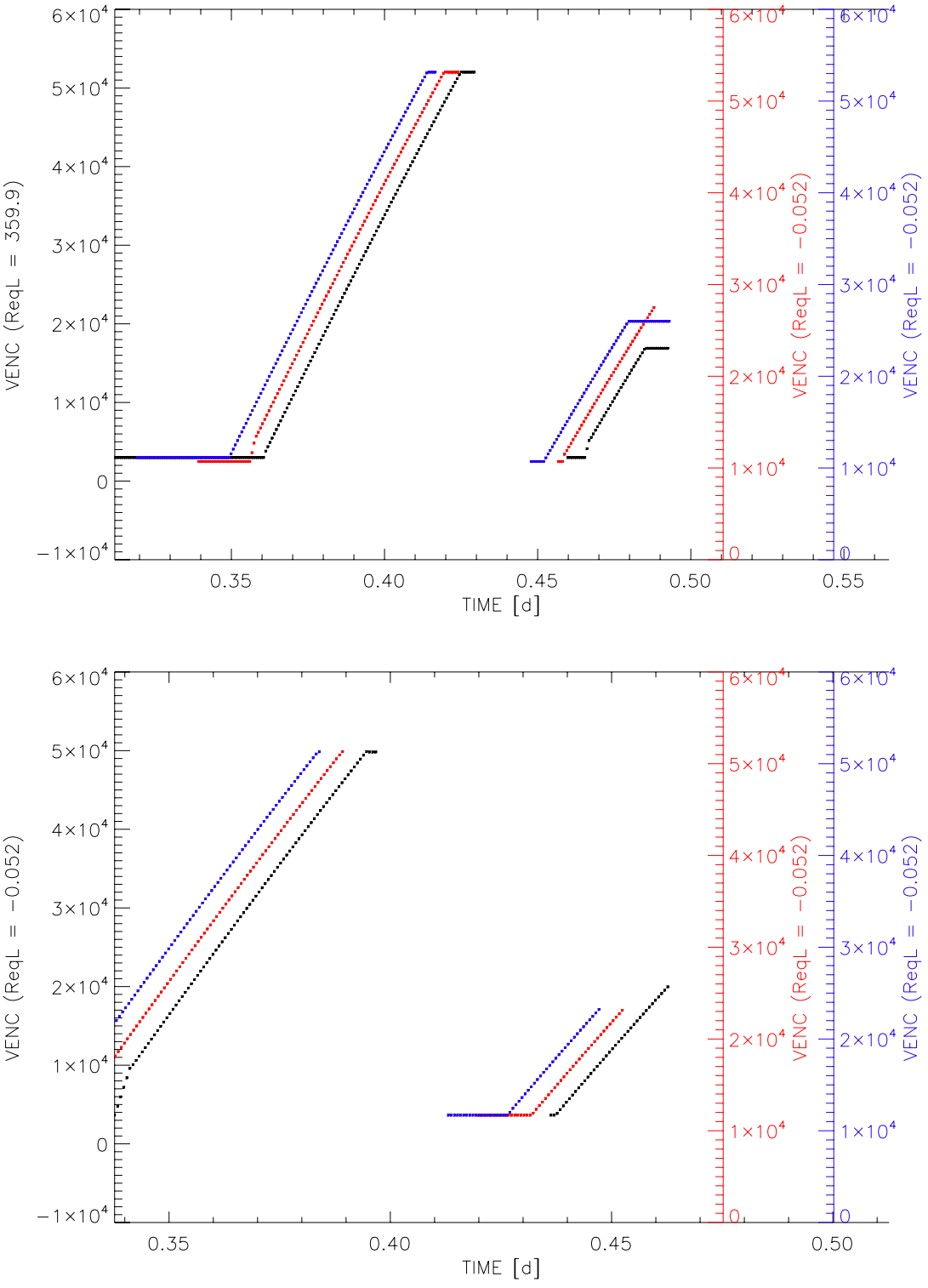

Figure 5.1: Comparison of vertical encoder values (Venc) of 3 days of tracking Sgr A (Curves on the right). The upper picture shows one tracking with standard target coordinates (black line) compared with two trackings using alternative coordinates (red and blue). The lower picture shows three days with alternative coordinates. The individual trackings are always two days apart. The curves on the left of the pictures represent times of Sco tracking.

5.1.3 Identification of Tracking Days

Days of galactic tracking can be found by looking at the shift entries in the 2003 logbook. Besides that several slow control parameters were investigated to identify galactic trackings. Fig. 5.2 exemplarily shows the voltage at the horizontal motor *VMOTV*, the requested galactic latitude *ReqB* and the value of the *PARK* variable (for explenation see Sec. 5.1.5) versus time.

Times of tracking can be clearly identified by motor voltages around 300 Volts whereas 400 Volts indicate fast movement between trackings. The shape of the voltage curves illustrates the direction of observation. Rising curves represent observations with the sunrise detectors, falling curves observations with the sunset detectors at the opposite side. The combination of ReqB being (almost) zero and PARK = 1 indicates tracking of the galactic centre. Trackings of Scorpio X-1 are identified by ReqB = 23.8 and PARK = 1. By looking at such distributions for all potential days of galactic tracking, it is possible to identify trackings that can be used for analysis. Plots that, for various reasons, lead to rejection of trackings can be found in Appendix B. Tab. 5.2 summarises both galactic trackings as they appear in the logbook and identified trackings.

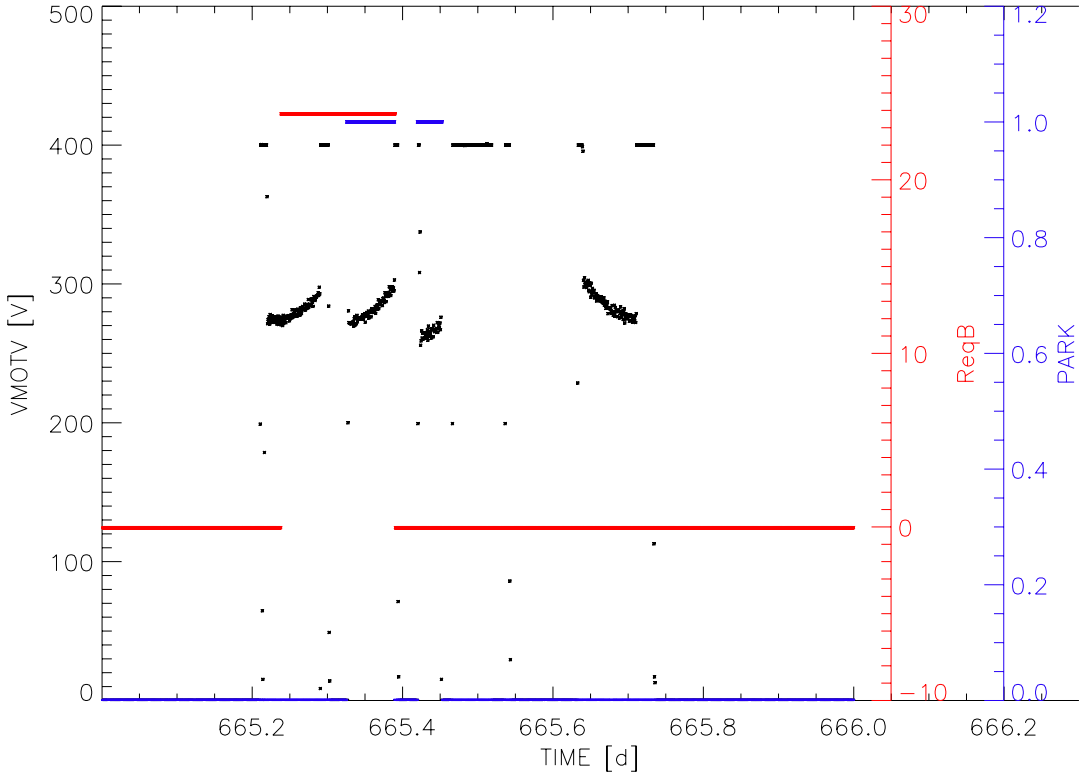

Figure 5.2: Voltage at the horizontal motor (black), requested galactic latitude (red) and value of the PARK variable (blue) versus time for 28th October 2003.

Date	Day	Logbook		Identified		Remark
		Sco	Sgr	Sco	Sgr	
04.09.03	611	x	x	x	x	
05.09.03	612	x	x	x	x	
07.09.03	614	x		x		
08.09.03	615	x	x	x	x	
11.09.03	618	x		x		Pseudo Sgr tracking with ReqL = 359.0
12.09.03	619	x		x		
20.09.03	627		x	x	x	Cryptic logbook entry
21.09.03	628	x	x	x	x	
22.09.03	629			x	x	No logbook entry
24.09.03	631	x	x	x	x	
27.09.03	634	x		x		
28.09.03	635	x	x			First half of day missing in slow control
04.10.03	641		x			Horizontal motor not running
16.10.03	653	x	x	x	x	
18.10.03	655	x	x	x	x	
20.10.03	657	x		x	x	Cryptic logbook entry
22.10.03	659	x		x		
26.10.03	663	x	x	x	x	
28.10.03	665	x	x	x	x	
30.10.03	667	x	x	x	x	
01.11.03	669	x	x			solar and galactic tracking interfere

Table 5.2: Identification of trackings. Days are counted from 1st January 2002 onwards.

5.1.4 Background Definition

Due to the use of an imaging X-ray telescope, a spot on the CCD chip can be defined where X-ray photons emerging from the magnet bore are expected to be registered. In 2003 this potential signal region was a rectangle from line 70 to 140 and column 30 to 63. Several possibilities exist to define the background used for the likelihood estimation. Each offers advantages and disadvantages so that is seems not reasonable to favour a specific method a priori. Therefore all analyses were carried out using three different background definitions whose spacial components are illustrated in Fig. 5.3.

Method 1

Events from the full CCD chip except for the signal region which were registered during galactic tracking are treated as background. The advantage of this method is that the background is measured at the same time as the tracking data so that a certain robustness concerning time dependency is given. Since the accumulated tracking time

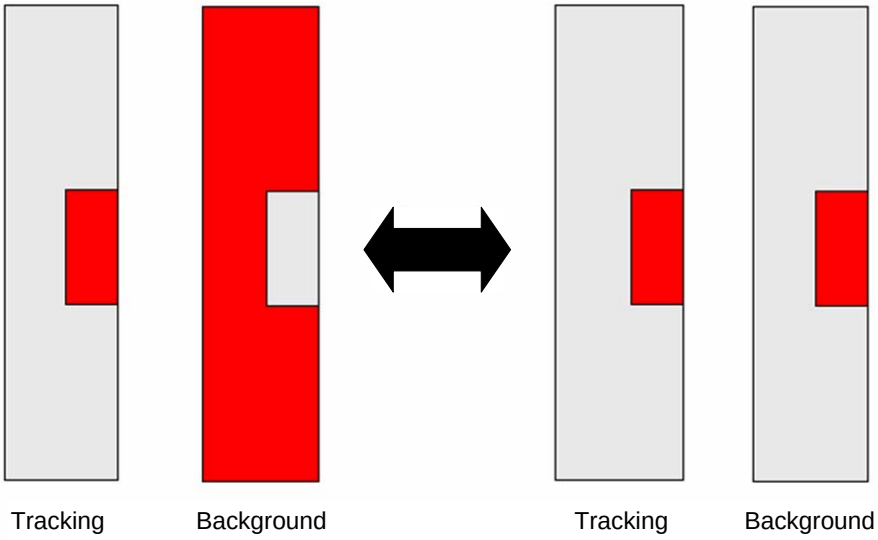

Figure 5.3: Spatial component of possible background definitions. The red area marks regions that either contribute to tracking data or background. The definition on the right hand side is just possible during non-tracking times. The distribution on the left hand side is possible during tracking and non-tracking times leading to a total of three different background definitions.

for galactic objects itself is relatively short just a limited number of background events can be obtained leading to poor statistics. Besides that unknown effects producing X-rays that emerge from the magnet and therefore are collected in the signal region can not be taken into account.

Method 2

Events being registered in the signal region during non-tracking can also be treated as background. This allows to gather high statistics and simulates most of the tracking conditions. Background photons that originate from the opposite side of the magnet and are focused on the spot can be taken into account. However, this feature can turn out to be a disadvantage as well. Even though the selected targets are somewhat prominent X-ray sources in the sky, it is a priori not clear that they emit more axions than any other star in the Milky Way. This can lead to unknown axion sources passing through the field of view that would accidentally contribute to the background. In case of solar observation this problem is avoided by the fact that the sun would dominate over any other axion source due to its proximity to earth.

Method 3

Another way to define background is to use the CCD chip as in method 1 but during non-tracking times. This enhances background measurement times enormously at the price of loosing correlation to potential signal data. This method offers the best signal to background ratio. The disadvantage of not reproducing all tracking conditions is

valid in this case as well. On the other hand axions from unknown celestial sources create photon events in the signal area and therefore do not accidentally contribute to the background.

5.1.5 Data Processing

A first stage of data processing is done by the CCD's data acquisition system (DAQ) automatically so that for each event on the chip basic information such as energy, position and time of impact is known.

The slow control PC (SC) as well as the tracking PC monitor and store the values of certain parameters that are needed for stage 2 of data processing. Correlation of information stored in the different computers is done by so-called *good time intervals (GTI)* that define times at which criteria of interest are fulfilled. All systems thus need to be synchronised. The GTIs obtained from the slow control and the tracking PC are merged together in a way that the resulting GTI defines the times when both primary GTIs coincide. This secondary GTI than can be used to select events from the DAQ computer which are stored in the FITS format[3] and can be used for further analysis later on. The criteria defined to extract data are discussed in the following.

- **Light:** This variable is used to indicate that light from the outside could disturbe the CCD detector. Different values represent different types of disturbance. It has to be assured that no light illuminates the magnet bores from the TPC side (Light $\neq 1$) and that no unknown problem occurs (Light $\neq 3$).[4]
- **MagB:** The magnetic field is calculated from the current which is monitored by the tracking PC. To make sure that the maximum sensitivity is reached, the field strength has to be larger than 8.9 T.
- **HMOTV:** The voltage at the horizontal motor has to be greater than 10 V which indicates that the magnet is actually moving.
- **VMOTV:** The voltage at the vertical motor has to fulfil the same condition.
- **ReqL:** The requested galactic longitude given in degrees. Together with ReqB this variable is used to distinguish between different galactic objects.
- **ReqB:** The requested galactic latitude given in degrees.
- **VPRECIS:** The precision of the movement concerning the vertical position has to be better than 0.01°. It is calculated by comparing the encoder values and the values the magnet is supposed to be at at a given time.
- **HPRECIS:** The tracking precision concerning the horizontal encoder values has to be better than 0.01° as well.

[3] Flexible Image Transport System.

[4] Additional shielding was installed later making it redundant to check the light variable for data obtained from 2004 on.

- **QUENCH:** This binary variable indicates quenches. If it is 1 there is a quench, if it is 0 there is none.
- **VT4OPEN:** Binary variable monitoring the status of valve VT4. If it is 1 the valve is open, if it reads 0 it is closed. To allow X-ray photons to travel towards the telescope it has to be open.
- **PARK:** Binary variable used to indicate times of galactic tracking.
- **TRACK:** Binary variable indicating times of solar tracking.

Tab. 5.3 summarises the conditions for valid galactic trackings and background definition in case the background is not measured simultaneously with the tracking data.

	Sco X-1	Sgr A	Background
Light	$\neq 1, \neq 3$	$\neq 1, \neq 3$	$\neq 1, \neq 3$
MagB	> 8.9	> 8.9	> 8.9
MMOTV	> 10	> 10	
VMOTV	> 10	> 10	
ReqL	> 359.0 and < 359.2	> 359.8 and < 360.0	
		or	
		> -0.2 and < 0.0	
ReqB	> 23.7 and < 23.9	> -0.2 and < 0.0	
VPRECIS	< 0.01	< 0.01	
HPRECIS	< 0.01	< 0.01	
QUENCH	0	0	0
VT4OPEN	1	1	1
PARK	1	1	0
TRACK			0

Table 5.3: Conditions used to define tracking data and background.

The valid ranges of ReqL and ReqB are somewhat arbitrary. By looking at all combinations of requested setpoints it can be assured that by choosing these combinations all galactic trackings are taken into account without accidentally treating anything else as galactic tracking. Combinations of ReqL and ReqB can be found in Appendix C.

Event Rejection

All events on the CCD chip are characterised by their spatial distribution (cp. Sec. 3.3.2). Single, double, triple and quadruple events can be caused by photons travelling perpendicular to the CCD plane and are therefore considered as *valid* events. All other shapes are caused by cosmic radiation and are therefore rejected as *invalid*. Events with diagonal shape can not be produced by single photons and are rejected as well.

Bad Pixel and CCD Edges

Outer lines and columns of the CCD are not able to show all types of valid event shapes and are therefore excluded from analysis. Known bad pixels are excluded as well. Fig. 5.4 illustrates the potential signal region and the position of the three known bad pixels. Cutting away the edges of the CCD leaves $200 \times 64 - 400 - 128 + 4 - 3 = 12273$ effective pixels behind. The signal area thus has a size of $70 \times 33 - 2 = 2308$ pixels.

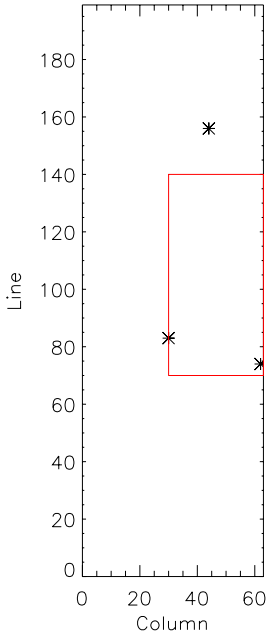

Figure 5.4: Position of bad pixels marked by crosses. The potential signal region is marked in red.

Summary of Data

After removing rejected tracking days and applying the cuts on bad pixels and CCD edges data processing yields the numbers of events and data taking times as summarised in Tab. 5.4. All events listed have energies between 0.5 and 10 keV. Event maps of the accumulated trackings of Sgr A and Sco X-1 are displayed in Fig. 5.5.

	Number of events		Data taking time		Count rate [s^{-1}]	
	Spot	Full chip	s	h	Spot	Full chip
Sgr A	8	69	22 320	6.20	3.58×10^{-4}	3.09×10^{-3}
Sco X-1	77	380	90 551	25.15	8.50×10^{-4}	4.20×10^{-3}
Bgrd	2926	16852	4 353 902	1209.42	6.72×10^{-4}	3.87×10^{-3}

Table 5.4: Number of events and data taking times. Bgrd denotes times of non-tracking as used for background method 2 and 3.

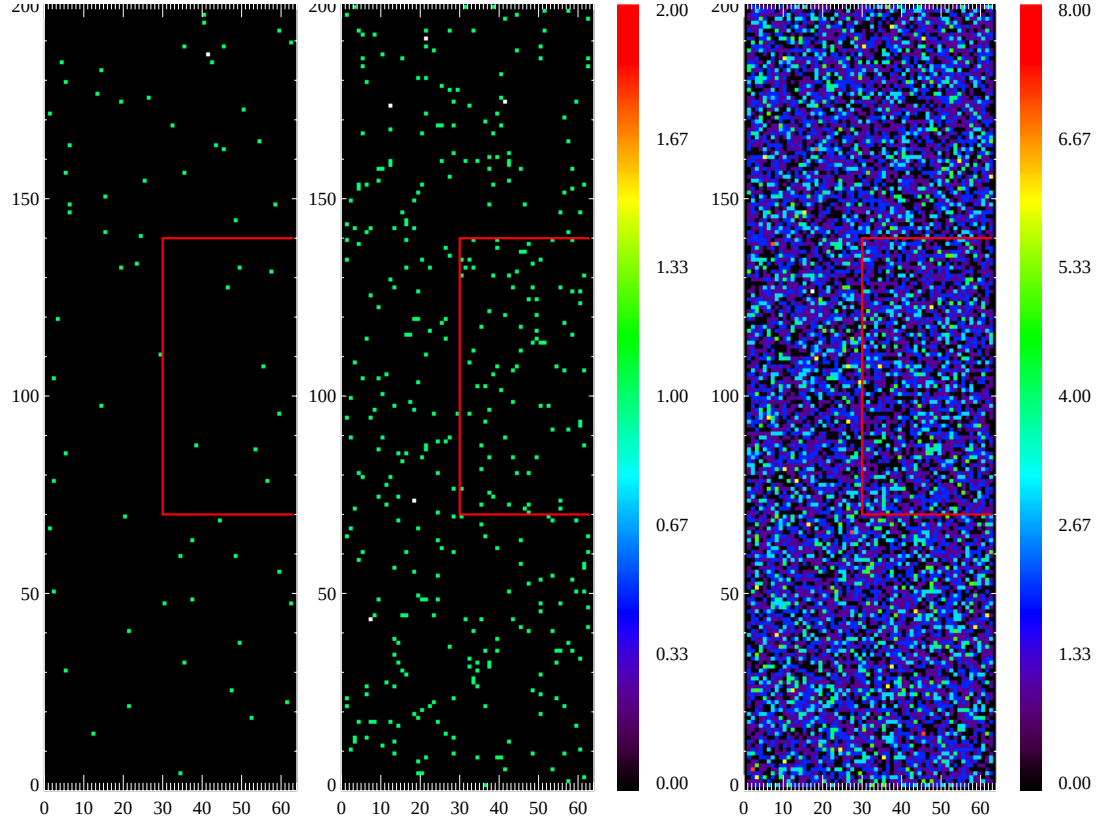

Figure 5.5: Accumulated event maps for tracking of Sgr A (left image), trackings of Sco X-1 (centre image) and background times (right image). The Signal region is marked by red rectangles. Colour keys refer to images left of them.

5.1.6 Temporal Distribution of Events

Since both observed objects show variations in their X-ray fluxes, the distribution in time of the tracking data is investigated. Fig. 5.6 and Fig. 5.7 provide a comparison of the light curves from Sgr A and Sco X-1 and the times at which events where registered by the CCD. The light curves are the same as in Fig. 4.3 and Fig. 4.4. By eye, this comparison yields no correlation of the number of events registered and the X-ray activity of the observed celestial objects.

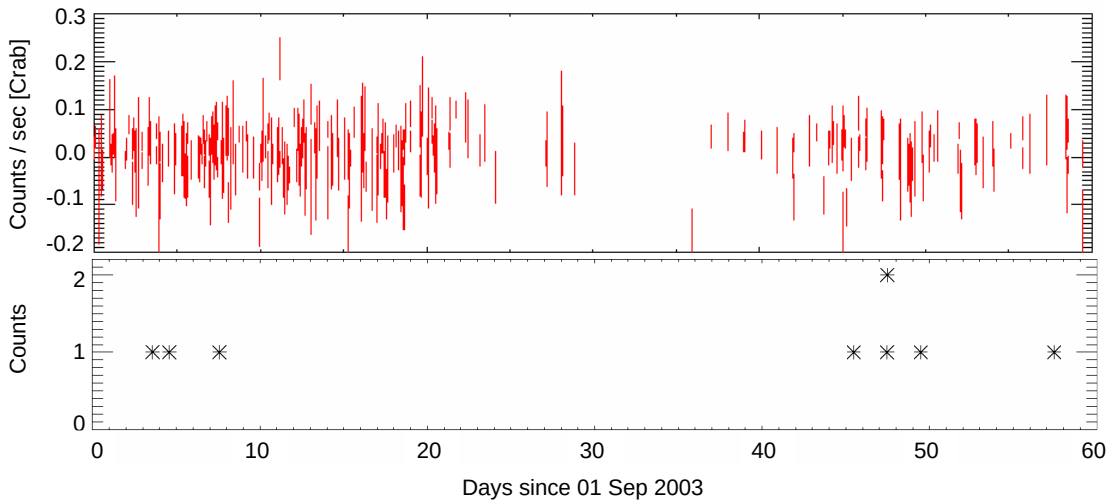

Figure 5.6: Comparison of the light curve of Sgr A and time of registration for events on the CCD. Each star denotes one event.

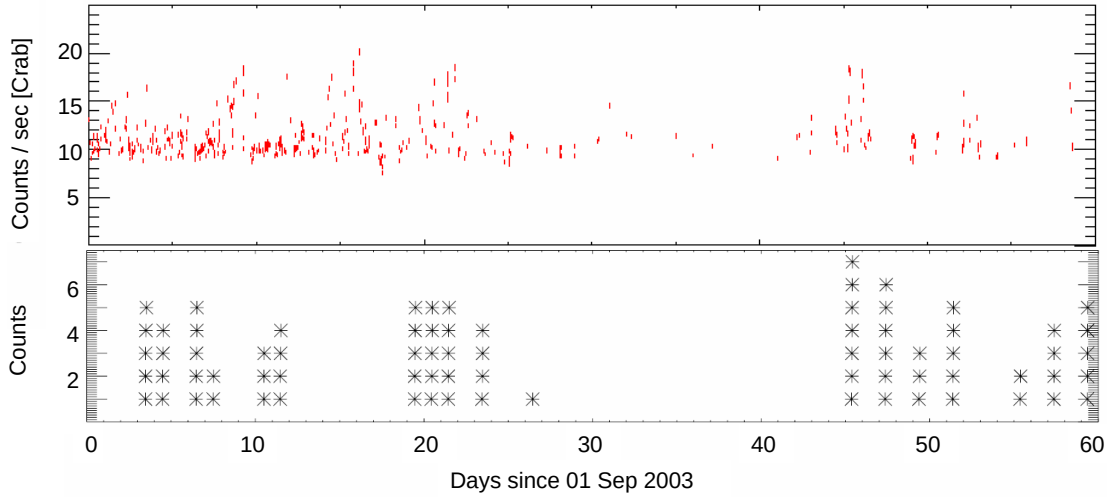

Figure 5.7: Comparison of the light curve of Sco X-1 and time of registration for events on the CCD. Each star denotes one event.

5.2 Determination of Upper Limits on $\phi g_{a\gamma}^2$

For further analyses the data obtained is binned with a binsize of 0.3 keV. Fig. 5.8 and Fig. 5.9 show histograms of the tracking and normalised background data as well as their difference. The displayed energy range is 0.5 to 9.8 keV and the background is determined according to method 3.

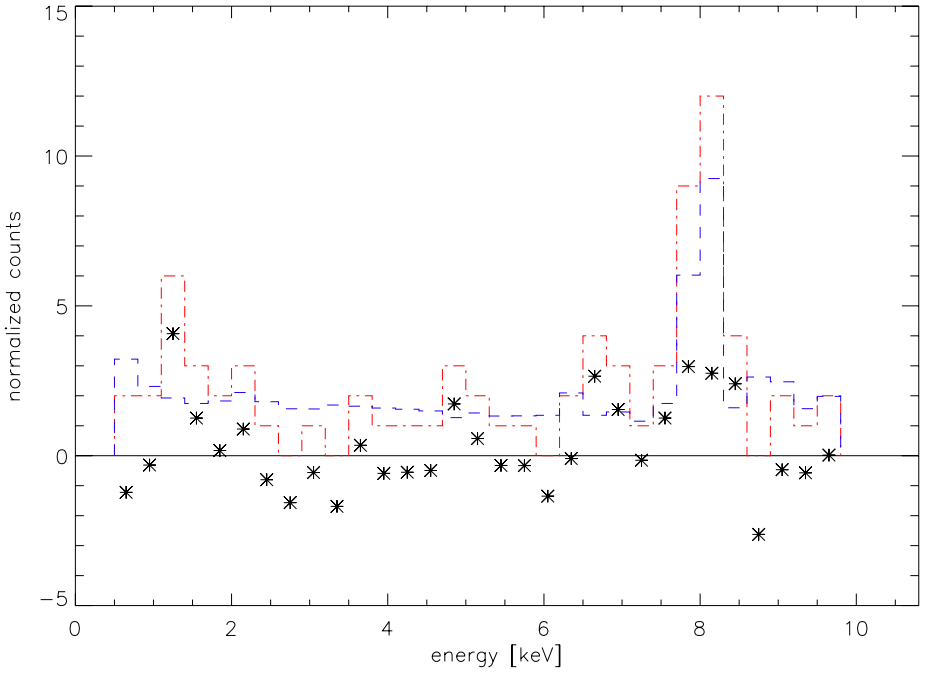

Figure 5.8: Histogram of tracking data from Sco X-1 (red dashed) and normalised background (blue dashed). The difference of the histograms is marked by black stars.

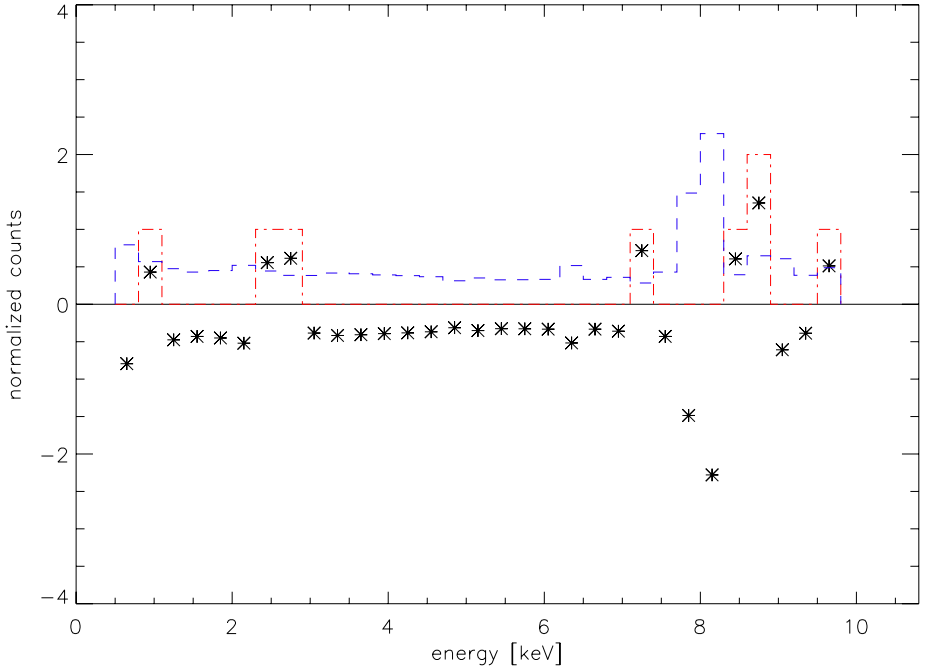

Figure 5.9: Histogram of tracking data from the galactic centre (red dashed) and normalised background (blue dashed). The difference of the histograms is marked by black stars.

The normalisation factor α is obtained by multiplying the ratios of data taking times and corresponding chip areas:

$$\alpha = \frac{\text{background time}}{\text{tracking time}} \times \frac{\text{background area}}{\text{signal area}}. \tag{5.1}$$

Depending on the background definition, the ratio of data taking times or the ratio of chip areas can be one. Tab. 5.5 summarises the background to tracking ratios for all background definitions.

Background definition	Sgr A	Sco X-1
Method 1	4.32	4.32
Method 2	195.1	48.1
Method 3	842.3	207.6

Table 5.5: Summary of background to tracking ratios.

5.2.1 The Maximum Likelihood Method

In order to determine an upper limit on the free parameter flux × coupling constant^2 ($\phi g_{a\gamma}^2$), the maximum likelihood method is used. It allows to determine parameters a in a way that the probability for the observed results is maximised. Besides that it can be applied for low statistics analyses [65]. The likelihood function

$$L = \prod_i P(x_i; a) \tag{5.2}$$

is the product of the probabilities P to find a certain data set x_i dependent on the parameter a and is supposed to be maximised. In case of Poissonian statistics the *extended maximum likelihood* can be used. This means the general likelihood function is normalised by the product of probabilities to find n events for an expectation value of n. The function to maximise then reads

$$L = \prod_i e^{-\mu_i} \frac{\mu_i^{n_i}}{n_i!} \Bigg/ \prod_i e^{-n_i} \frac{n_i^{n_i}}{n_i!}\ , \tag{5.3}$$

where n_i denotes the number of events in the ith bin and μ_i denotes the corresponding number of expected events. This expectation is the sum of normalised background counts b_i and expected signal events $a(E_i)$ whose number depends on the energy and the actual value of the fit parameter. Thus it can be expressed as

$$\mu_i = \frac{b_i}{\alpha} + a(E_i), \tag{5.4}$$

where α is the ratio of background to tracking data as summarised in Tab. 5.5. One advantage of using the extended maximum likelihood is that the value

$$\chi^2 = -2 \ln L \tag{5.5}$$

can be used as a goodness-of-fit test, since it follows a χ^2-distribution [10]. Another advantage is that applying the logarithm to Eq. 5.3 turns the product into a sum which is in general easier to compute. To avoid practical problems arising from negative values of $a(E_i)$ and thus μ_i Eq. 5.5 is rewritten as

$$\chi^2 = \sum_i 2\,\mu_i - n_i \ln(\mu_i^2) - 2\,n_i + n_i \ln(n_i^2). \tag{5.6}$$

Due to the sign in Eq. 5.5 this function is no longer maximised but minimised. The resulting *maximum likelihood estimator*, which is the value for the free parameter to minimise Eq. 5.5, is not affected.

Errors on Maximum Likelihood Estimators

Errors on maximum likelihood estimators can be obtained by looking at its likelihood-distribution. For maximum likelihood 1 σ is defined to be the value of the free parameter where $\ln L$ is 0.5 below its maximum. 2 σ can be found where $\ln L$ is 2.0 below its maximum and accordingly 3 σ where $\ln L$ is 4.5 below its maximum. However, these statistical errors are just symmetric in case of the large sample limit, i.e. if the number of events N goes to infinity. Additionally, 2 standard deviations are not twice the one standard deviation for finite N [66].

Using maximum likelihood as in Eq. 5.5, the criteria mentioned to find standard deviations have to be redefined:

$$\begin{aligned} 1\,\sigma &\mathrel{\widehat{=}} \phi g_{a\gamma}^2(\chi^2_{\min} + 1.0), \\ 2\,\sigma &\mathrel{\widehat{=}} \phi g_{a\gamma}^2(\chi^2_{\min} + 4.0), \\ 3\,\sigma &\mathrel{\widehat{=}} \phi g_{a\gamma}^2(\chi^2_{\min} + 9.0), \end{aligned}$$

where $\phi g_{a\gamma}^2$ represents the free parameter of the maximum likelihood estimation. Fig. 5.10 provides an example of a χ^2-distribution with marked standard deviations.

Upper Limits

Since no signal above background was found, an estimate on the upper limit on the free parameter $\phi g_{a\gamma}^2$ is carried out. Upper limits are closely related to confidence levels (CL) at which they are extracted.

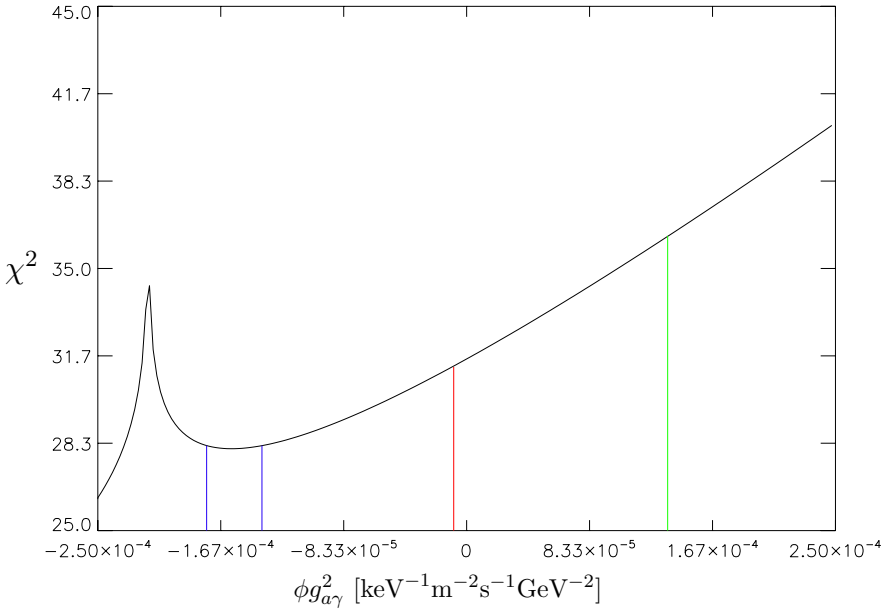

Figure 5.10: χ^2-distribution obtained with Sgr-data from Fig. 5.9. The values of one standard deviation to the left and to the right are marked by blue lines. The red line denotes 2 σ and the green line 3 σ. The x-axis shows the free parameter of the fit. Below $\phi g_{a\gamma}^2 = 2 \times 10^{-4}$ m^{-2}s^{-1}keV^{-1}GeV^{-2} the χ^2-values get non-physical.

The upper limit (UL) is the value of the free parameter that, used as upper integration limit for the normalised integral over the probability distribution function (p.d.f.), yields the integral to be equal to the confidence level:

$$\mathrm{CL} = \int_0^{\mathrm{UL}} e^{-\chi^2/2}\,\mathrm{d}\phi g_{a\gamma} \Big/ \int_0^{\infty} e^{-\chi^2/2}\,\mathrm{d}\phi g_{a\gamma}\ . \tag{5.7}$$

Both integrations start at zero because negative values are treated as being non-physical, even though the maximum likelihood estimation might yield negative best fit values [67]. χ^2 is the function defined in Eq. 5.5. Although in principle no certain value sticks out of the many choices one has, a confidence level of 95 % is generally used in the context of this work. Note that the actual value of the maximum likelihood estimator is not needed for upper limit estimations.

5.2.2 Assuming Flat Spectra

If no assumption is made concerning the shape of a potential axion spectrum, the number of expected events in a given bin $a(E_i)$ can be expressed as

$$a(E_i) = \frac{\mathrm{d}\phi}{\mathrm{d}E} \cdot P_{a\to\gamma} \cdot t \cdot A \cdot \varepsilon(E_i) \cdot (1 - f_{\mathrm{OoT}}) \cdot \Delta E. \tag{5.8}$$

$\mathrm{d}\phi/\mathrm{d}E$ is the differential axion flux, $P_{a\to\gamma}$ the axion to photon conversion probability, t the data taking time, A the area covered by the experimental setup, ε the energy dependent efficiency and f_{OoT} the fraction of Out-of-Time events. ΔE denotes the binsize. The conversion probability is [56]:

$$P_{a\to\gamma} = 1.701 \times 10^{-17} \left(\frac{B\,L}{9.0\,\mathrm{T}\;9.26\,\mathrm{m}}\right)^2 \left(\frac{g_{a\gamma}}{10^{-10}\,\mathrm{GeV}^{-1}}\right)^2, \tag{5.9}$$

with B denoting the magnetic field strength and L the length of the conversion volume. Combination of Eq. 5.8 and Eq. 5.9 yields

$$a(E_i) = \phi g_{a\gamma}^2 \cdot \frac{0.24502}{\mathrm{T}^2\mathrm{m}^2\mathrm{GeV}^{-2}} \cdot B^2 \cdot L^2 \cdot A \cdot t \cdot \varepsilon(E_i) \cdot (1 - f_{\mathrm{OoT}}) \cdot \Delta E, \tag{5.10}$$

where $\phi g_{a\gamma}^2$ is the fit parameter in units of $\mathrm{m}^{-2}\mathrm{s}^{-1}\mathrm{keV}^{-1}\mathrm{GeV}^{-2}$. Eq. 5.6 is used along with Eq. 5.4 and Eq. 5.10 to perform the maximum likelihood analysis. Some of the parameters in Eq. 5.10 are predetermined by the experimental setup:

$$\begin{aligned} B &= 9.0\,\mathrm{T}, \\ L &= 9.26\,\mathrm{m}, \\ A &= 1.4522 \times 10^{-3}\,\mathrm{m}^2, \\ f_{\mathrm{OoT}} &= 0.092, \\ \Delta E &= 0.3\,\mathrm{keV}. \end{aligned}$$

The efficiency is calculated from the effective area (cp. Fig 3.17) and the data taking time is taken from Tab. 5.4.

In case of zero entries in a bin ($n_i = 0$), the corresponding summand in Eq. 5.6 is replaced by

$$(\chi^2)_i = 2\,\mu_i. \tag{5.11}$$

Upper limits on $\phi g_{a\gamma}^2$ were extracted for all energy ranges and background definitions. A complete summary of the results can be found in Appendix D. Fig. 5.11 shows an example of an $\exp(-\chi^2/2)$-distribution along with the extracted upper limit on $\phi g_{a\gamma}^2$. The observed object is Scorpius X-1, the energy range is from 0.5 keV to 9.8 keV and the background definition applied is method 3. The resulting upper limit on $\phi g_{a\gamma}^2$ is $3.58 \times 10^{-5}\,\mathrm{m}^{-2}\mathrm{s}^{-1}\mathrm{keV}^{-1}\mathrm{GeV}^{-2}$ at 95 % confidence level.

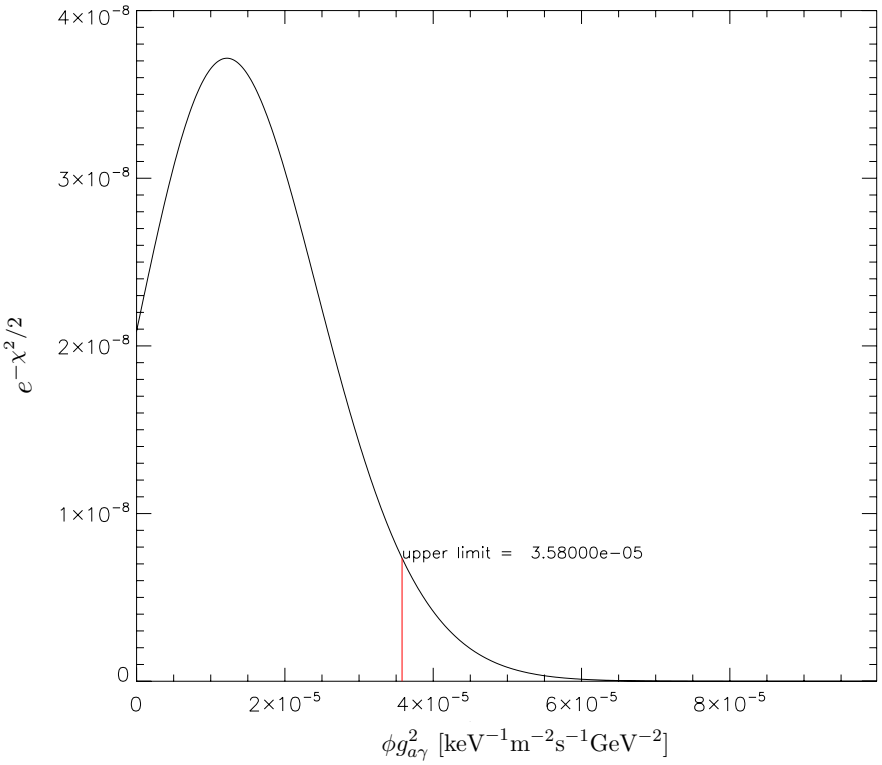

Figure 5.11: $e^{-\chi^2/2}$-distribution for Sco X-1 with no assumption on the shape of the expected axion spectrum. The investigated energy range is from 0.5 to 9.8 keV. Background method 3. The upper limit (red line) marks the position where the area under the curve up to the red line divided by the total area is 0.95.

5.2.3 Assuming X-Ray-Like Spectra

Axions are believed to be produced via the Primakoff effect. Therefore axion spectra are supposed to have a shape like the X-ray spectra of the observed celestial objects.[5] In the analysis of solar data not only the shape of the spectrum is used to compute the expectation values in Eq. 5.4 but also models predicting the number of produced axions as a function of $g_{a\gamma}$. For the objects investigated in this thesis no such models do exist, but nevertheless the axion spectrum can be assumed to have an X-ray-like shape. Eq. 5.10 is modified to take this into account:

$$a(E_i) = \phi g_{a\gamma}^2 \cdot \frac{0.24502}{\mathrm{T^2 m^2 GeV^{-2}}} \cdot B^2 \cdot L^2 \cdot A \cdot t \cdot \varepsilon(E_i) \cdot (1 - f_{\mathrm{OoT}}) \cdot \Delta E \cdot w(E_i), \quad (5.12)$$

where $w(E_i)$ denotes a weighting factor that can either suppress the influence of a certain bin or enhance it, depending on the actual value of $w(E_i)$. In order to determine the

[5] The expected axion spectrum in case of the sun follows rather the black body spectrum of the solar core than the X-ray spectrum as it can be observed.

weighting factors the spectra from Fig. 4.5 and Fig. 4.6 are tabulated. For each energy of interest the corresponding number of counts can be obtained and used as relative weighting factors $w'(E_i)$. The relative weighting factors have to be re-normalised in a way that the mean of all weighting factors equals one. Thus they are calculated according to

$$w(E_i) = \frac{w'(E_i) \cdot N}{\sum_i w'(E_i)}, \tag{5.13}$$

with N denoting the number of weighting factors used. Fig. 5.12 provides an example of an $\exp(-\chi^2/2)$-distribution obtained under the assumption of an X-ray-like axion spectrum. The same conditions as in case of Fig. 5.11 are applied. The limit on $\phi g_{a\gamma}^2$ is $1.95 \times 10^{-5}\,\mathrm{m^{-2}s^{-1}keV^{-1}GeV^{-2}}$ at 95 % confidence level. Further results can be found in Appendix D.

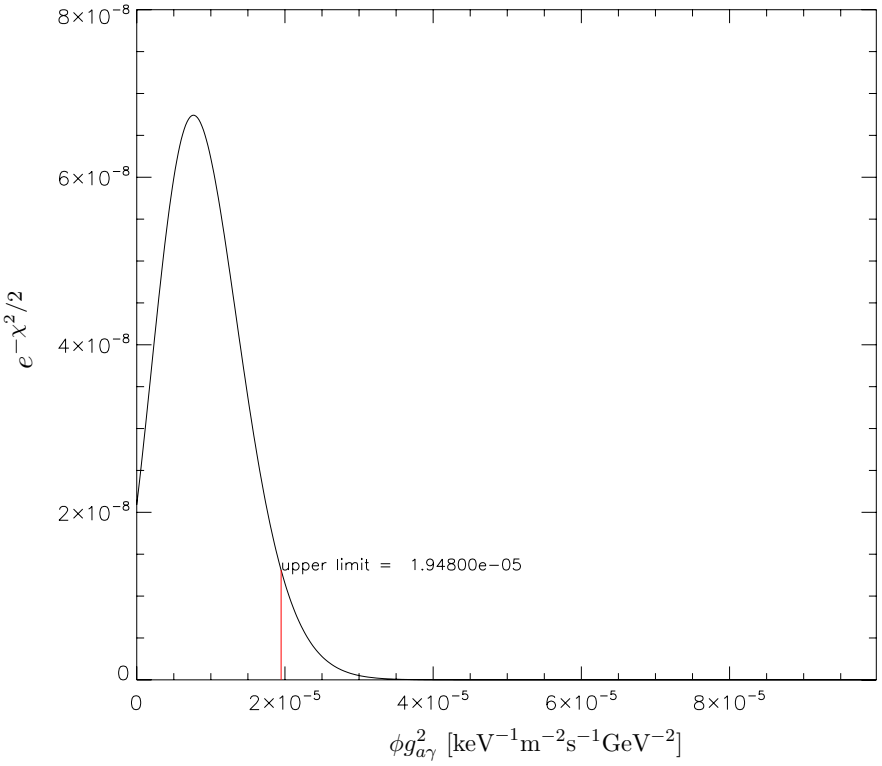

Figure 5.12: $e^{-\chi^2/2}$-distribution for Sco X-1 assuming an X-ray-like axion spectrum. The same conditions for data processing as in case of Fig. 5.11 are used. The red line marks the upper limit on $\phi g_{a\gamma}^2$.

5.2.4 Comparison of the Results

All upper limits calculated in the scope of this work are summarised and compared in Fig. 5.13 in case of Sgr A and Fig. 5.14 in case of Sco X-1. Limits extracted for the energy range from 6.0 keV to 7.2 keV are not included but can be found in Tab. 5.6.

Background definition	Axion spectrum	$\phi g_{a\gamma}^2$ (95 % CL) [m^{-2} s^{-1} keV^{-1} GeV^{-2}]
1	flat	17.6×10^{-5}
2	flat	17.6×10^{-5}
3	flat	17.6×10^{-5}
1	X-ray-like	17.5×10^{-5}
2	X-ray-like	17.5×10^{-5}
3	X-ray-like	17.5×10^{-5}

Table 5.6: Upper limits on $\phi g_{a\gamma}^2$ for the iron emission peak of Sgr A. The investigated energy range is from 6.0 to 7.2 keV.

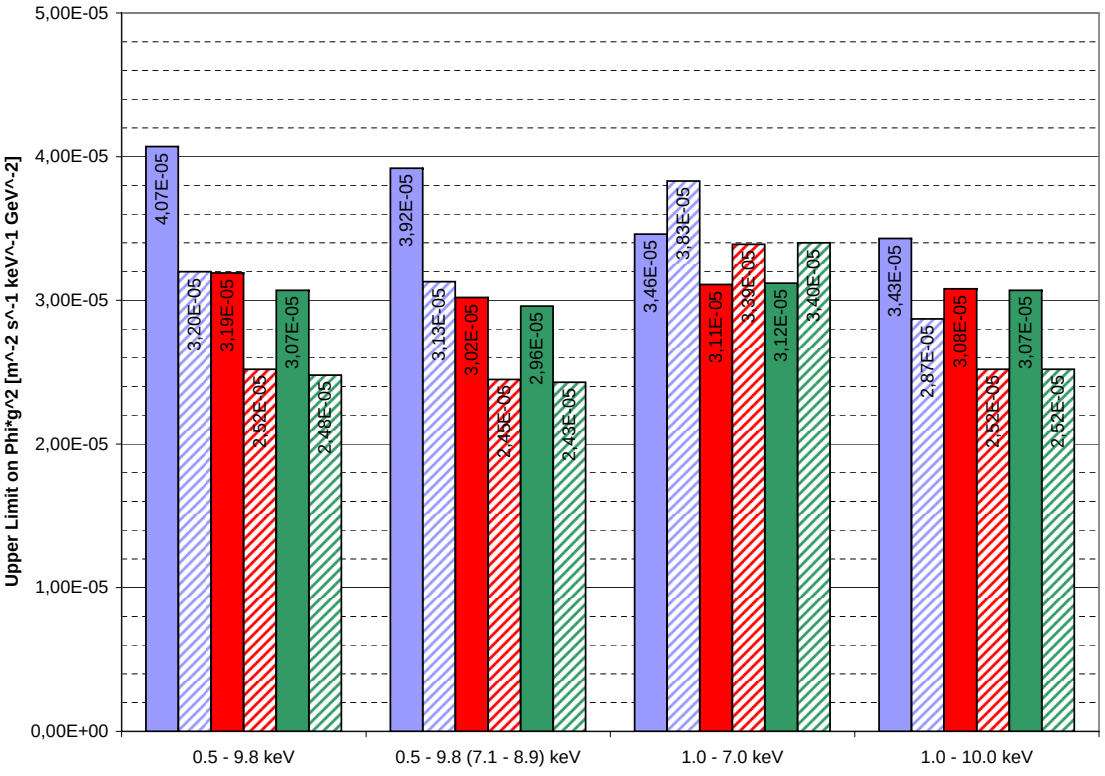

Figure 5.13: Comparison of upper limits on $\phi g_{a\gamma}^2$ extracted from Sgr A data. Solid bars represent results obtained assuming a flat axion spectrum, striped bars indicate calculations with X-ray-like spectra. Background definition 1 is represented by blue, definition 2 by red and definition 3 by green fillings. The numbers at the x-axis give the investigated energy ranges in keV. Ranges in parentheses are left out.

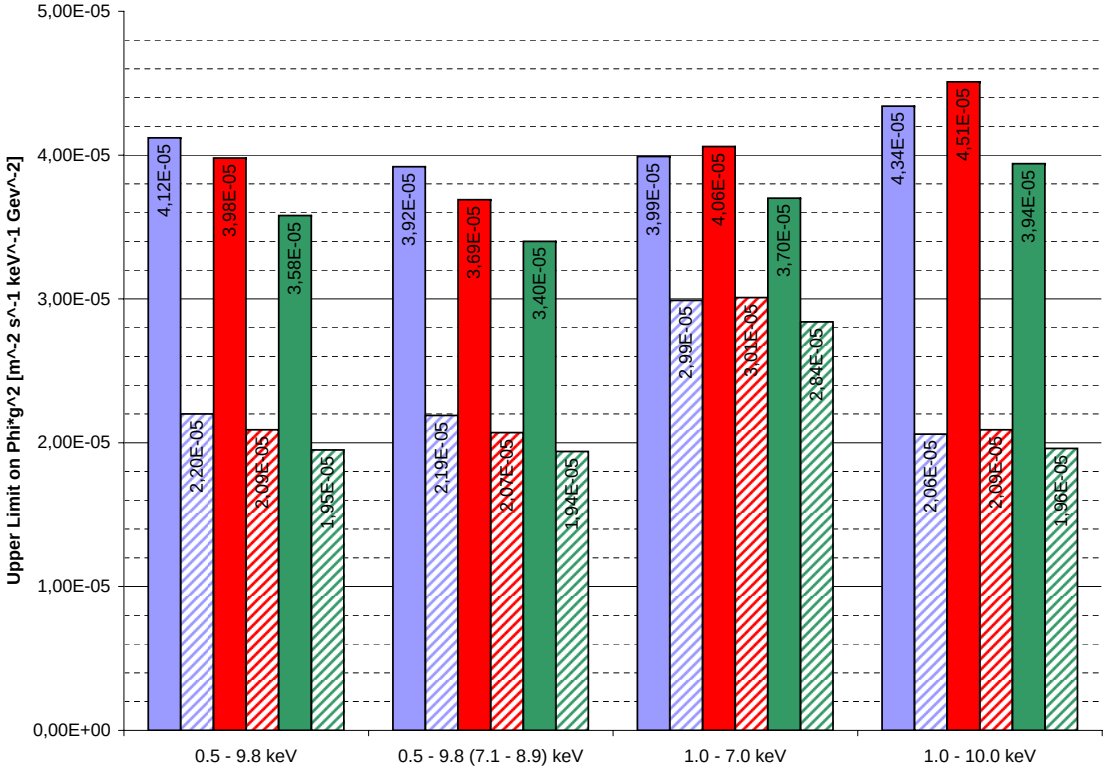

Figure 5.14: Comparison of upper limits on $\phi g_{a\gamma}^2$ extracted from Sco X-1 data. Solid bars represent results obtained assuming a flat axion spectrum, striped bars indicate calculations with X-ray-like spectra. Background definition 1 is represented by blue, definition 2 by red and definition 3 by green fillings. The numbers at the x-axis give the investigated energy ranges. Ranges in parentheses are left out.

Limits computed using background definition 2 are usually better than limits obtained by applying method 1. Method 3 provides the best results since it has the largest background to signal ratio and thus the best statistics. Cutting away the copper peak from 7.2 to 8.9 keV enhances the limit as well since it lowers the background count rate.

Flat vs. X-Ray-Like Spectra

A comparison of the upper limits calculated with both methods reveals that assuming an X-ray-like spectrum yields better limits than assuming a flat distribution. The only exception is the energy range from 1.0 to 7.0 keV in case of analysing Sgr A data (cp. Fig. 5.13). This effect is stronger for limits on Scorpio X-1 than for the limits on Sagittarius A which originates from the shape of the X-ray spectra. The spectrum of Sco X-1 follows a power law combined with absorption due to hydrogen. The maximum therefore is located at low energies. Towards higher energies the X-ray flux gets continuously lower, leaving a pronounced asymmetry behind. Even though the shape of the Sgr A spectrum is less regular, it has no such clear left-right asymmetry. Weighting factors extracted from both spectra can be seen in Fig. 5.15.

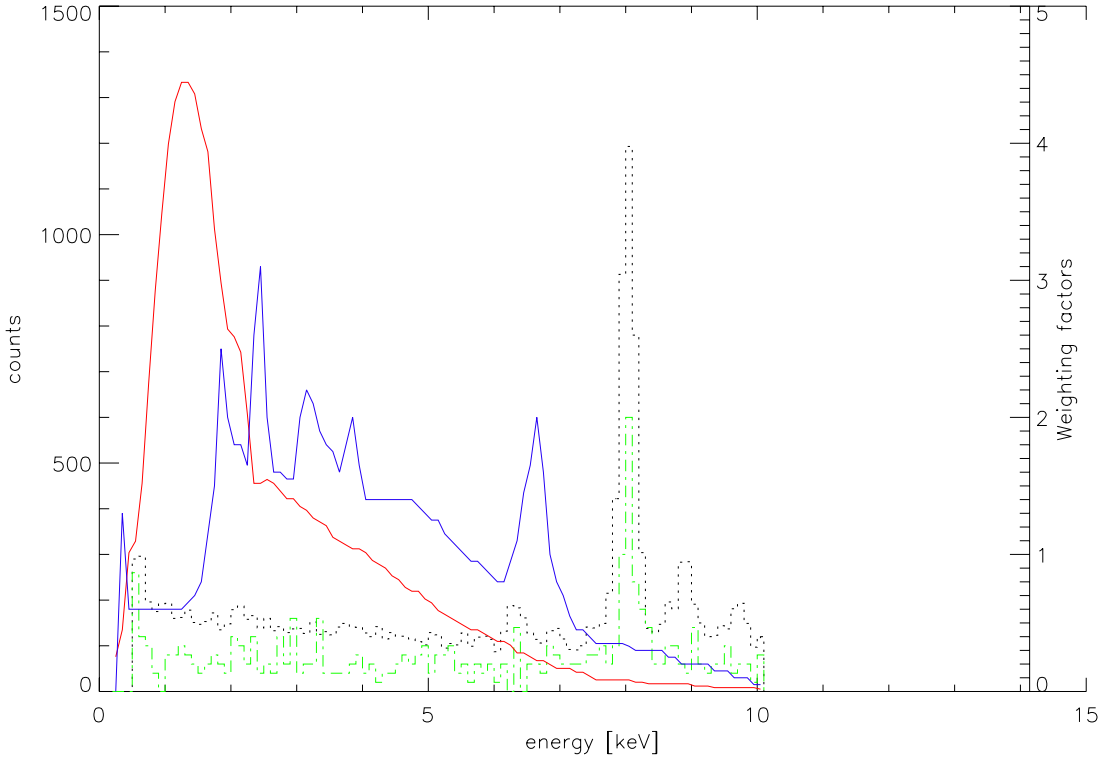

Figure 5.15: Weighting factors for data from Sco X-1 (red curve) and Sgr A (blue curve). The right y-axis give the normalised factors. The left y-axis gives the number of counts for the background spectrum (black dashed) and the spectrum from Sco tracking (green dashed) that are plotted along. Both spectra are not normalised.

Bins that correspond to intense regions in the X-ray spectra are multiplied with a large factor in Eq. 5.12. The consequence is an expectation of large numbers of counts in these bins which is not observed in the data. Staying behind expectations usually lowers upper limits. Thus these bins contribute to the calculation in a way that the total upper limit gets lowered. In contrast, expectations for bins multiplied by a weighting factor smaller than one are lowered and therefore likely to be exceeded by the data. These bins contribute to a higher upper limit. However the effect of staying behind expectations seems to be stronger than the contrary effect for most of the investigated energy ranges.

Scorpio X-1 vs. Sagittarius A

Even though the tracking time of Sco X-1 exceeds the one of Sgr A by a factor of 4, the upper limits on $\phi g_{a\gamma}^2$ are lower in case of analysing Sgr A data. This result contradicts expectations because upper limits are supposed to get lower with increasing data taking time. Using the background statistics from Tab. 5.4 and the background to signal ratios from Tab. 5.5, expectation values for galactic trackings can be derived. Background definition 3 provides the best statistics and is therefore used for this estimation. In

total, 16.5 events are expected for all trackings of Sgr A and 67.1 events are expected for all trackings of Sco X-1. Fig. 5.16 illustrates the Poisson distribution for expectation values of 16.5 and 67.1 events. The areas marked in yellow are the probabilities to find 8 or less counts for 16.5 expected events ($p = 1.7\,\%$) and the one to find 77 or less counts for 67.1 expected events ($p = 89.6\,\%$) respectively.

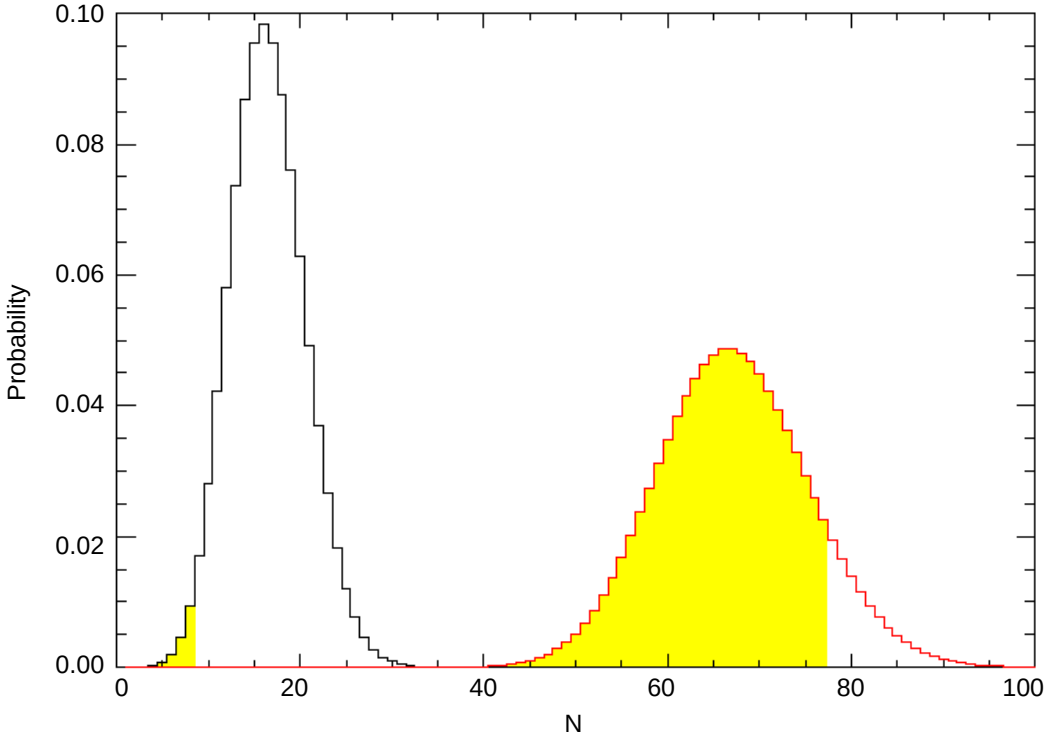

Figure 5.16: Poisson distributions for expectation values of 16.5 (black) and 67.1 respectively (red). Regions in yellow mark the probability to find 8 or less counts if 16.5 are expected and the probability to find 77 or less counts if 67.1 are expected.

5.2.5 Systematic Studies

From the Poisson statistics it can be seen that an unexpectedly low number of events was observed during trackings of the galactic centre. Whether this accounts for statistical fluctuations or for systematic influences is discussed in the following.

Several problems with the CCD chip can be imagined that would lead to lower count rates than expected. E.g., if the supply voltage of the CCD had been too low, this would have led to too few registered events. However, most of such problems would not only have an influence on the tracking but also on the background count rate. Thus the behavior of the background count rate is investigated to make sure that the low number of events during Sgr A-trackings does not originate from any systematical effect.

Fig. 5.17 shows the light curve of the CCD detector for September and October 2003.

The solid grey area denotes the total count rate, the coloured lines refer to the count rates of valid events for different energy ranges (see caption of Fig. 5.17). Note that the events used to compute the light curve are raw events and not processed as described in Sec. 5.1.5. Besides the natural fluctuations, no abnormal behavior can be observed. Thus the conclusion can be drawn that the number of raw events during trackings of Sgr A behaves as expected.

Not only the number of raw events is of interest for systematic studies. For instance problems with the calibration could lead to wrong allocation of events and energies. This in return can cause events which in principle are within the investigated energy range to be cut away during data processing. To exclude such problems, the detector performance of the period from August to October 2003 is plotted in Fig. 5.18. Even though calibration information is not available for all days, no unexpected behaviour of the CCD can be seen. The days of galactic trackings are marked in red and show no deviation besides statistical fluctuations. This holds also for the position of the ^{55}Fe peak which is used for calibration. The distribution of *gain*, which denotes the relation between analogue-digital units (ADU) as given by the read-out electronics and reconstructed event energy in eV, is flat as well. The *charge tarnsfer inefficiency* CTI denotes the fraction of charge that is lost while being shifted from the position of impact to the read out anode. The distibution of CTI shows no unexpected behaviour.

The arguments listed above lead to the conclusion that the low number of registered events in case of Sgr A-trackings are rather of statistical than of systematic nature.

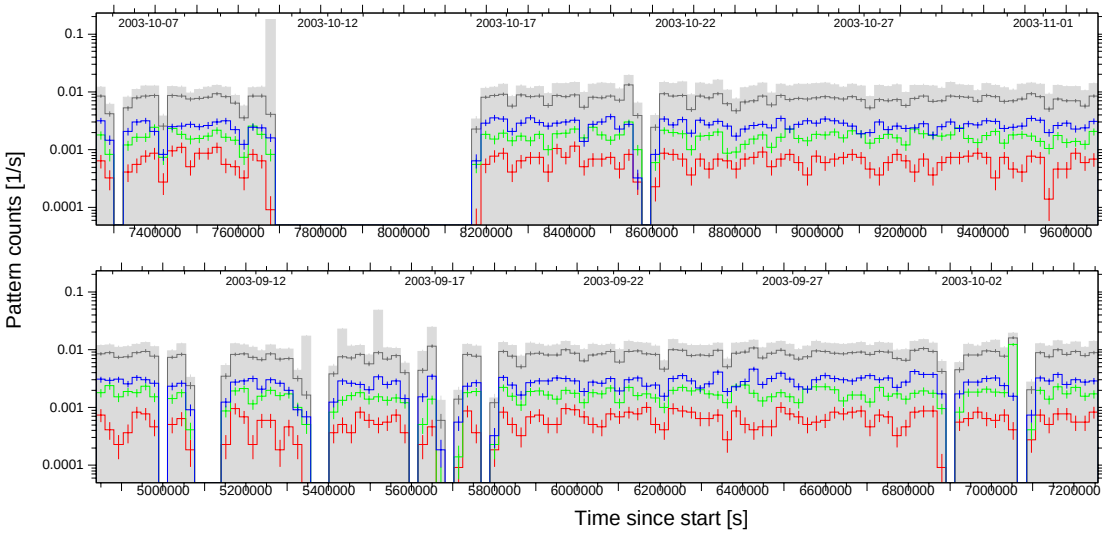

Figure 5.17: Light curve for September and October 2003. The number of total events is plotted in solid grey. The grey line denotes valid events in the energy range from 0.5 to 20.0 keV, the red line denotes 0.5 to 2.0 keV, the green line 2.0 to 7.0 keV and the blue line represents valid events with energies between 7.0 and 14.0 keV. The bin size is a quarter of a day.

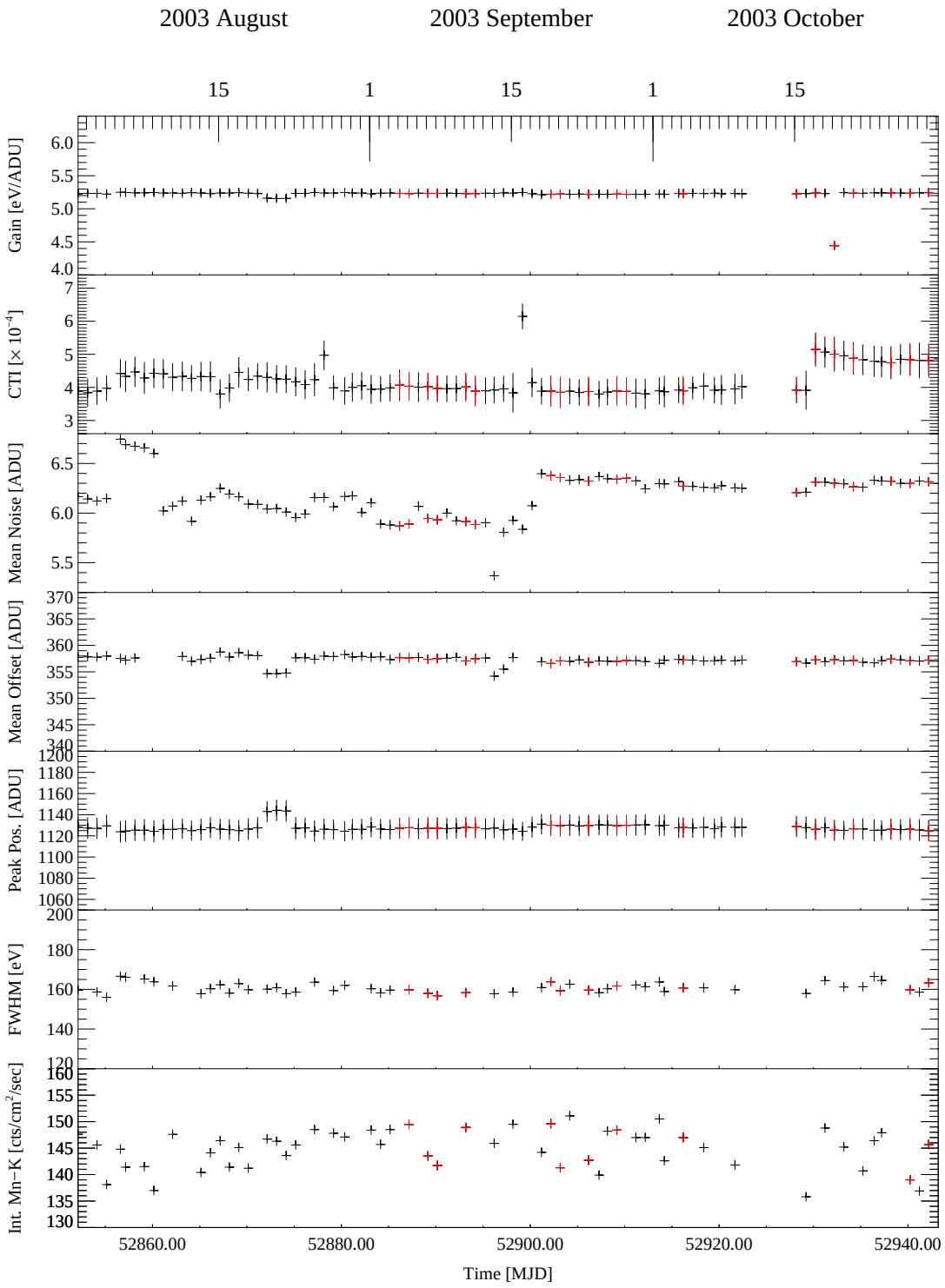

Figure 5.18: Performance of the CCD detector in 2003. Days of galactic tracking are marked by red crosses. Statistical errors are indicated by the length of the y-component of the crosses. For some days the intensity of the Mn-K line and its full width at half maximum (FWHM) is not known. On October 20th, the FWHM of the Mn-K line is about 4000 eV due to a corrupted file and therefore not displayed.

5.2.6 Upper Limit Extraction for Nearby Objects

Due to the fact that the observed galactic objects are located at a certain distance to earth, several other objects are situated in the line of sight if looking at Sgr A or Sco X-1. The field of view of CAST has a radius of approximately 0.17 °, which roughly corresponds to 10 arcmin. In contrast to solar observations, this field of view is not fully covered by celestial point sources. Therefore it is not possible to observe a given object of interest alone. Nearby objects are always observed as well, although their influence on the extracted upper limit varies.

As illustrated in Fig. 3.12, the effective area of the X-ray telescope and thus the combined efficiency of the telescope and the CCD chip depends on the angle objects are looked at (vignetting). During the calibration measurements at PANTER, the rotational orientation of the telescope remained fixed so that x- and y-components of the vignetting effect could be distinguished. However, in case of galactic trackings this orientation is unknown. Therefore mean values of all four components[6] of the vignetting effect have to be used to determine the effective areas for given off-axis angles. Due to their large number, upper limits are not extracted for each object in the proximity of Sgr A and Sco X-1. The influence of 10 different off-axis angles on the upper limit on $\phi g_{a\gamma}^2$ is determined so that a set of concentrical circles is obtained. The upper limit for an object situated in a given circle is the upper limit for the central object multiplied by the factor that corresponds to this circle. Tab. 5.7 summarises the effective areas and upper limits for off-axis observation. Fig. 5.19 shows a comparison of relative effective areas and extracted upper limits on $\phi g_{a\gamma}^2$ depending on the off-axis angle and Fig. 5.20 provides the concentrical shells of factors.

Off-axis angle		Effective area		Factor on
[arcmin]	[deg]	[cm^2]	[%]	upper limit
0	0.0	7.80	100.0	1.000
1	0.0167	7.35	94.23	1.062
2	0.0333	6.70	85.90	1.164
3	0.0500	5.83	74.68	1.339
4	0.0667	5.00	64.10	1.561
5	0.0833	4.23	54.17	1.847
6	0.1000	3.48	44.55	2.245
7	0.1167	2.85	36.54	2.736
8	0.1333	2.25	28.85	3.440
9	0.1500	1.68	21.47	4.290
10	0.1667	1.18	15.06	6.643

Table 5.7: Influence of off-axis angles on the telescope effective area and the upper limit on $\phi g_{a\gamma}^2$. Effective areas calculated from PANTER data (cp. Fig. 3.12).

[6] The four components are left (−x), right (+x), up (+y) and down (−y).

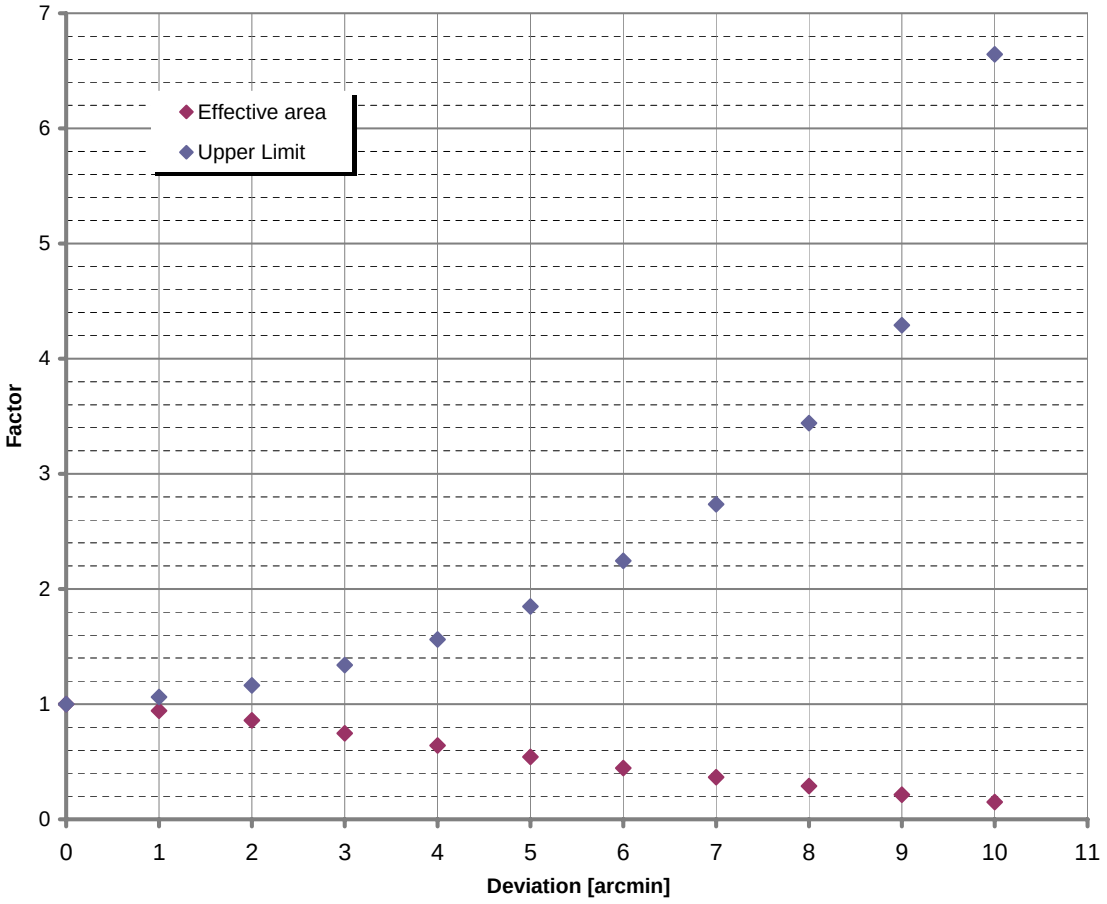

Figure 5.19: Factors for upper limits on $\phi g_{a\gamma}^2$ (blue) and relative effective areas (purple) versus off-axis angles.

The use of this shell model leads to underestimated results because the vignetting effect and its influence on upper limits is usually overestimated. Nevertheless this problem is negligible, since upper limits and not exact results are extracted.

A complete list of objects within CAST's field of view during galactic trackings can be obtained from the SIMBAD[7] database[8]. Strictly speaking, SIMBAD provides not a list of objects but a list of identifiers. One object might be referred to by a couple of identifiers depending on the method of observation. The term "Sco X-1" e.g. is the identifier for this star if observed by X-ray observatories. In the visible the same object is referred to by the identifier "V818 Sco". All identifiers are used here, since sometimes it is not clear if they denote the same objects.

[7] Set of Identifications, Measurements and Bibliography for Astronomical Data.
[8] http://simbad.u-strasbg.fr/simbad/

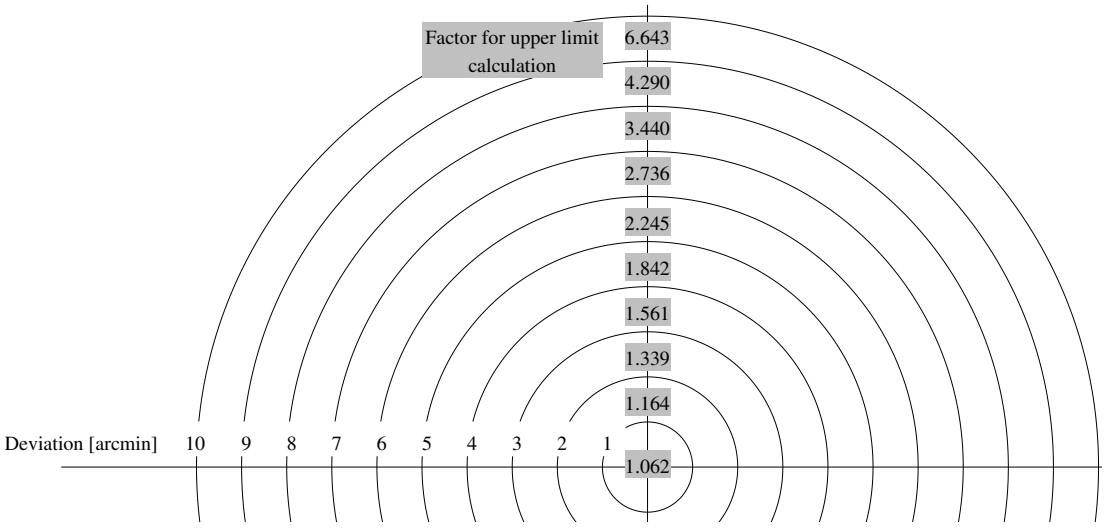

Figure 5.20: Factors for upper limit calculation for off-axis observation. The upper limit for objects in the proximity is the upper limit for Sgr A / Sco X-1 times the factor in the shell that contains the nearby object.

In total, 3790 identifiers are found in the vicinity of the galactic centre. For lack of space they are not listed but can be found online at *http://tinyurl.com/pwo283*.[9] All identifiers found within the radius of 0.17 ° around $L = 359.1\,^\circ$ and $B = 23.8\,^\circ$, which is the setpoint for observation of Sco X-1, are listed in Tab. 5.8. The corresponding upper limits on $\phi g_{a\gamma}^2$ are calculated as well, based on the results from Sec. 5.2.2. For this specific calculation the investigated energy range is 0.5 to 9.8 keV, the shape of the axion spectrum is assumed to be flat and the background definition applied is method 3. Fig. 5.21 illustrates the vicinities of Sgr A and Sco X-1 respectively.

Procedure for Possibly Existing Pointing Inaccuracy

The method of calculating angle-dependent factors for upper limit extraction can also be used to correct any kind of pointing inaccuracy. In case the galactic filming reveals a minor constant deviation between galactic target coordinates and actual pointing direction, the results obtained within this work can simply be multiplied by the factor that corresponds to the deviation.

[9] tinyurl.com is an online service that replaces long and complicated URLs by a combination of letters and numbers. The full URL is:
http://simbad.u-strasbg.fr/simbad/sim-coo?CooDefinedFrames=none&Coord=359.948d-0.046d&CooEpoch=2000&submit=submit%20query&Radius.unit=deg&CooEqui=2000&CooFrame=Gal&Radius=0.17

Identifier	Radial distance [arcmin]	$\phi g_{a\gamma}^2$ (95 % CL) [m^{-2} s^{-1} keV^{-1} GeV^{-2}]
[HH95] V818 Sco-19	1.37	4.2×10^{-5}
2MASS J16195902-1536474	1.68	4.2×10^{-5}
WISH B1617.0-1532b	1.69	4.2×10^{-5}
IRAS 16170-1532	1.85	4.2×10^{-5}
1RXS J161954.9-153542	1.92	4.2×10^{-5}
[HH95] V818 Sco-21	2.00	4.8×10^{-5}
2MASS J16195820-1539494	2.59	4.8×10^{-5}
2MASS J16194316-1539112	2.86	4.8×10^{-5}
EQ J161940-153725	2.90	4.8×10^{-5}
2MASS J16194505-1539469	2.92	4.8×10^{-5}
[HH95] V818 Sco-24	2.98	4.8×10^{-5}
[HH95] V818 Sco-36	3.10	5.6×10^{-5}
[HH95] V818 Sco-5	3.18	5.6×10^{-5}
2MASS J16194683-1534195	3.55	5.6×10^{-5}
2MASS J16194498-1534289	3.63	5.6×10^{-5}
2MASS J16195783-1541181	3.92	5.6×10^{-5}
2MASS J16194745-1533388	4.13	6.6×10^{-5}
[HH95] V818 Sco-37	4.38	6.6×10^{-5}
[HH95] V818 Sco-13	4.43	6.6×10^{-5}
2MASS J16194038-1541050	4.63	6.6×10^{-5}
[HH95] V818 Sco-26	4.67	6.6×10^{-5}
[HH95] V818 Sco-12	4.77	6.6×10^{-5}
EQ J162010-153943	4.77	6.6×10^{-5}
[HH95] V818 Sco-11	4.78	6.6×10^{-5}
BD-15 4303	4.88	6.6×10^{-5}
2MASS J16195654-1542294	4.98	6.6×10^{-5}
[HH95] V818 Sco-3	5.03	8.0×10^{-5}
2MASS J16193571-1540426	5.20	8.0×10^{-5}
[HH95] V818 Sco-6	5.53	8.0×10^{-5}
2MASS J16193620-1541297	5.62	8.0×10^{-5}
[HH95] V818 Sco-10	5.83	8.0×10^{-5}
[HH95] V818 Sco-35	5.87	8.0×10^{-5}
[HH95] V818 Sco-9	6.22	9.8×10^{-5}
[HH95] V818 Sco-41	6.33	9.8×10^{-5}
HD 146950	6.93	9.8×10^{-5}
HIP 79972	7.93	12.3×10^{-5}
IRAS 16168-1539	9.34	23.8×10^{-5}
EQ 1616-154	9.88	23.8×10^{-5}

Table 5.8: Upper limits on $\phi g_{a\gamma}^2$ for objects close to Sco X-1. Energy range: 0.5 - 9.8 keV.

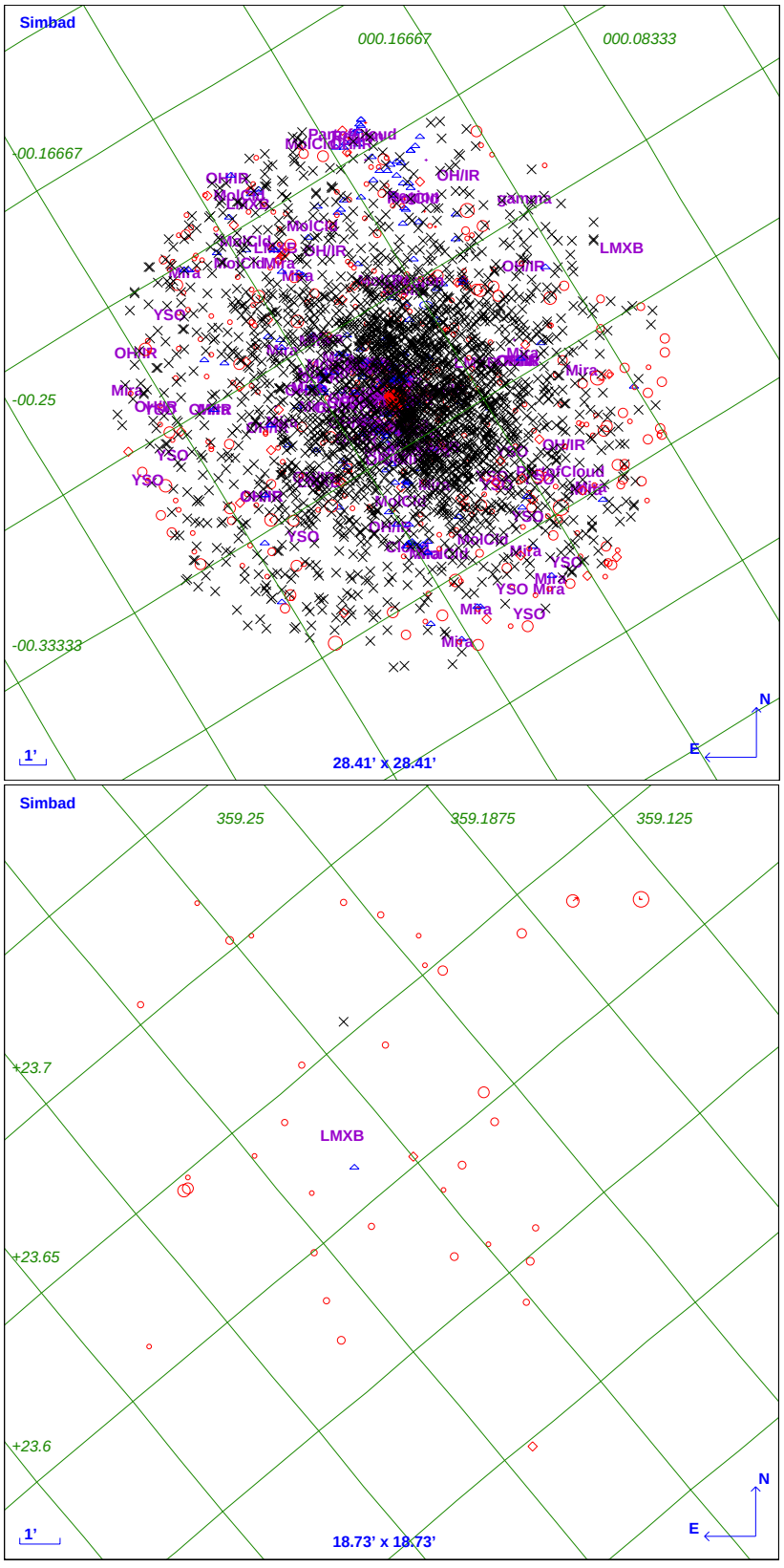

Figure 5.21: Objects in the vicinity of Sgr A (upper image) and Sco X-1 (lower image). Stars are denoted by red circles, X-ray objects by black crosses, IR sources by red diamonds, radio sources by blue triangles and other objects by purple abbreviations. Sco X-1 is located where "LMXB" is printed in the lower picture.

5.3 New Insights?

The extracted limits on the $\phi g_{a\gamma}^2$ can be used do draw exclusion plots with the coupling constant on the abscissa and the flux on the ordinate for both Sagittarius A and Scorpio X-1. Since these limits refer to axions with masses below 0.02 eV, the limit on the coupling constant from CAST phase I (cp. Sec. 3.4) can be applied:

$$g_{a\gamma} < 8.8 \times 10^{-11}\ \mathrm{GeV}^{-1}.$$

Using logarithmic axes, a straight exclusion line is obtained. Fig. 5.22 shows the exclusion plot for Sgr A.

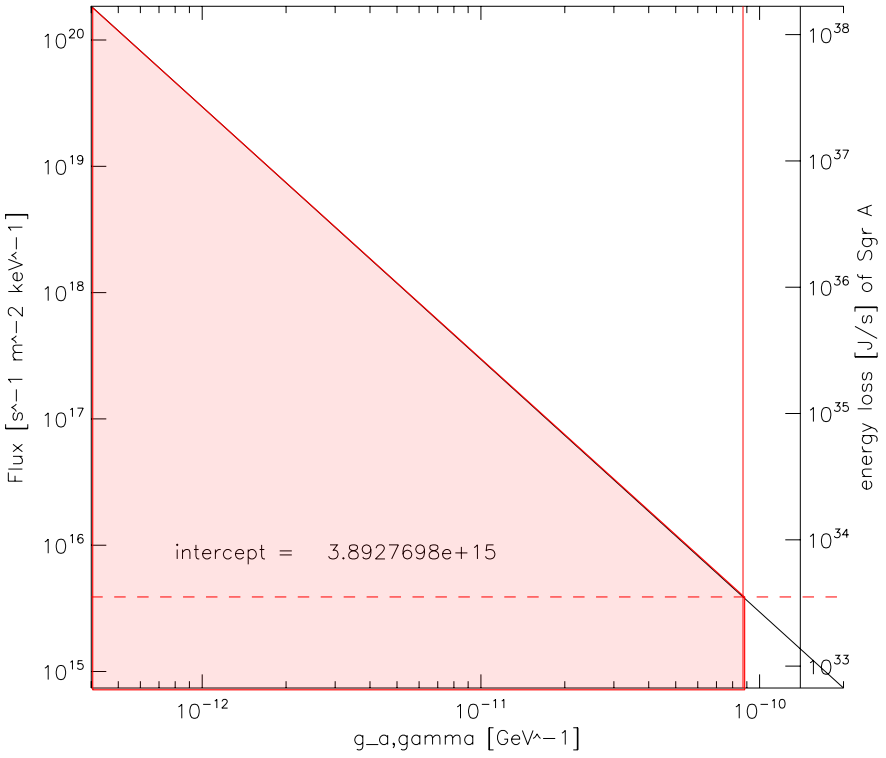

Figure 5.22: Exclusion plot for Sgr A. The x-axis represents the axion to photon coupling constant, whereas the y-axis denotes the axion flux per keV. The vertical red line is the upper limit on the coupling constant from CAST phase I. Combinations of flux and coupling constant that are not excluded are marked by the pale red filling. The horizontal dashed red line marks the intercept of exclusion line and upper limit on $g_{a\gamma}$. Using the distance of Sgr A and a minimum mass for the axion, an energy loss rate due to axion emission can be calculated (additional y-axis on the right).

The intercept of the upper limit on the coupling constant and the exclusion line denote the flux for which new insights are gained. This flux is referred to as *minimum flux* ϕ_{min} in the following. Below this line all combinations of flux and coupling constant are not

excluded yet, above this line excluded combinations appear. Knowing the distance d from a galactic object of interest to earth (cp. Chapter 4) the number of axions emitted per second N, which corresponds to the minimum flux, can be calculated. If the energy per axion E_{axion} is known, this number can even be translated into an energy loss rate P:

$$P = \phi_{\text{min}} \cdot 4\pi d^2 \cdot E_{\text{axion}} \cdot \Delta E, \tag{5.14}$$

where ΔE is the investigated energy range in keV. Multiplication by the width of the investigated energy range is needed since the flux in Eq. 5.14 stricly speaking is the differential flux $\mathrm{d}\phi/\mathrm{d}E$.

The minimum energy per axion is its rest mass energy, which is at least 10^{-6} eV as is known from theoretical constraints (cp. Sec. 2.3.2). However, if just the rest mass energy is taken into account, some sort of exotic mechanism has to be imagined that accelerates axions to energies of the order keV because 0.5 keV is the minimum axion energy CAST is sensitive to. On the other hand, this obscure mechanism should not change the direction of motion of axions, because the exclusions drawn refer to point sources. For this reasons it seems more realistic to assume that axions are emitted with kinetic energies of at least 0.5 keV by the investigated objects in order to be registered by CAST. Therefore the minimum energy per axion can be assumed to be of order keV. Tab. 5.9 provides the energy loss rates that correspond to minimum fluxes of Sgr A and Sco X-1, both taking only rest mass energy and kinetic energy into account.

	Energy loss rate [W]	
Energy per emitted axion	Sgr A	Sco X-1
Rest mass energy only (10^{-6} eV)	4×10^{33}	5×10^{32}
Kinetic energy ($\sim$ 1 keV)	4×10^{42}	5×10^{41}

Table 5.9: Energy loss rates for Sgr A and Sco X-1 that correspond to the minimum axion flux.

These results in turn imply that Scorpio X-1 actually can emit axions in the energy range of order keV with up to 5×10^{41} W, even though observation of Sco X-1 by CAST revealed no signal above background. A similar conclusion can be drawn for the galactic centre.

A comparison of these possible axion outputs with the total luminosity of the sun ($\sim 10^{26}$ W) or the integrated X-ray luminosity of Sco X-1 ($\sim 10^{31}$ W) leads to the conclusion that present day axion telescopes such as CAST do not provide the sensitivity needed to detect axions from celestial objects. Furthermore, the energy loss limits mentioned above seem to be easily beatable by stellar evolution arguments.

6. Summary and Outlook

In 2003, the CERN Axion Solar Telescope (CAST) observed the celestial objects Sagittarius A and Scorpio X-1 in order to find out whether axions with masses below 0.02 eV/c^2 are emitted by them. Sco X-1 was tracked for 25.15 hours and the galactic centre for 6.2 hours in total. In the scope of this work, the data obtained with the CCD detector is analysed. Unfortunately, no signal above background can be found. However, for the first time ever an upper limit on the flux $\times$ axion to photon coupling constant^2 ($\phi g_{a\gamma}^2$) can be derived for these two objects, using the method of maximum likelihood. To avoid any bias, this estimation is carried out for various energy ranges covered by the detector's sensitivity, and different background definitions are applied. The upper limit extraction is done under the assumption of a flat axion spectrum and under the assumption of an axion spectrum having the shape of the corresponding X-ray spectrum. For this purpose, X-ray spectra of Sgr A and Sco X-1 obtained with the XMM-Newton space mission are used.

The upper limits extracted vary depending on the energy range and the assumption for the axion spectrum. For both objects these limits are within the range of

$$\phi g_{a\gamma}^2(95\ \%\ \mathrm{CL}) \approx 2\ -\ 5 \times 10^{-5}\ \mathrm{m}^{-2}\mathrm{s}^{-1}\mathrm{keV}^{-1}\mathrm{GeV}^{-2},$$

at 95 % confidence level.

Using the distances of the celestial bodies and the upper limit on the coupling constant from CAST phase I, axion fluxes can be calculated that in principle could be irradiated without being detected by CAST. Assuming energies of 1 keV per axion, this flux can be translated into an energy loss rate caused by axion emission. The maximum energy loss due to axions that is unnoticed by CAST P_{max} is

$$P_{\mathrm{max,Sco}} \sim 5 \times 10^{41}\ \mathrm{W},$$
$$P_{\mathrm{max,Sgr}} \sim 4 \times 10^{42}\ \mathrm{W},$$

in case of Sco X-1 and Sgr A respectively. These energy loss rates exceed the integrated X-ray luminosity of Sco X-1 by 10 orders of magnitude. Even though an energy loss due to axion emission that is much greater than the X-ray luminosity can not be excluded it apears to be highly unlikely. Therefore the conclusion is drawn that present day axion telescope techniques are probably inadequate to detect axions from celestial objects.

The search for solar axions with CAST continues towards axion masses of ~ 1.4 eV/c^2, thus entering the parameter space regions that are favoured by axion models. In case the existence of the axion is proven, not only the strong CP-problem is solved. Depending on its properties, the axion is part of the unknown dark matter and therefore highly interesting in terms of astronomy and cosmology.

If the sensitivity of present day axion telescopes could be exceeded in the (far) future, the wide field of axion astronomy would open up. Axions do hardly interact with matter and thus are able to cross the universe without changing direction or loosing energy. The detection of such particles would provide a unique opportunity to investigate regions of the cosmos that can not be observed by ordinary techniques.

A. Astronomical Coordinate Systems

Equatorial Coordinates

Earth's geographic poles, zenith and nadir, as well the equator are projected onto the celestial sphere. The *declination* gives the angle of a certain object above or below the equator and is used as the first coordinate. Declinations are usually given in degrees, arcmin and arcsec as e.g. in

$$\text{dec} = -29^\circ\, 0'\, 29.7''.$$

The longitude, which is the second coordinate, can be defined in two ways:

1. The *hour angle* is fixed to earth's coordinate system in a way that south is defined to be zero. The direction of counting is south-west-north-east. Using hour angles as second coordinate makes the equatorial coordinate system dependent on time and the position of the observer.
2. Alternativly the *right ascension* can be used as a second coordinate. In this case zero is no longer defined by a position fixed to earth but by a arbitrary reference point that does not change position relative to the celestial sphere. Usually the vernal equinox Υ is used so that this equatorial system is independent of the observer's position. The direction of counting is the same as in case of using hour angles.

Both definitions have in common that the second coordinate is given in hours, minutes and seconds as in e.g.

$$\text{right ascension} = 17^\text{h}\, 45^\text{m}\, 40.045^\text{s}.$$

Galactic Coordinates

The galactic coordinate system uses the galactic plane as base circle. Latitudes B are the angles of certain objects relative to the galactic plane. Positive values are used for all objects within the northern galactic hemisphere, negative values for the southern hemispere. Longitudes L are measured using an axis pointing from the sun to the galactic centre. L is the angle beween this axis and the one connecting the sun and the projection of the observed object onto the galactical plane. Nevertheless, two different ways of counting exist:

1. Longitudes L range from -180° to $+180^\circ$, or
2. longitudes L range from 0° to 360°,

where in both cases the galactic center coincides with $L = 0^\circ$.

Epoch

Due to earth's nutation and precession the apparent position of stars changes over long periods of time. Therefore a reference time needs to be given when quoting celestial coordinates. *J2000.0* is frequently used as epoch. The preceding letter "J" referes to Julian years so that J2000.0 is julian date 2451545.0, or January 1st, 2000 at noon.

B. Rejected Trackings

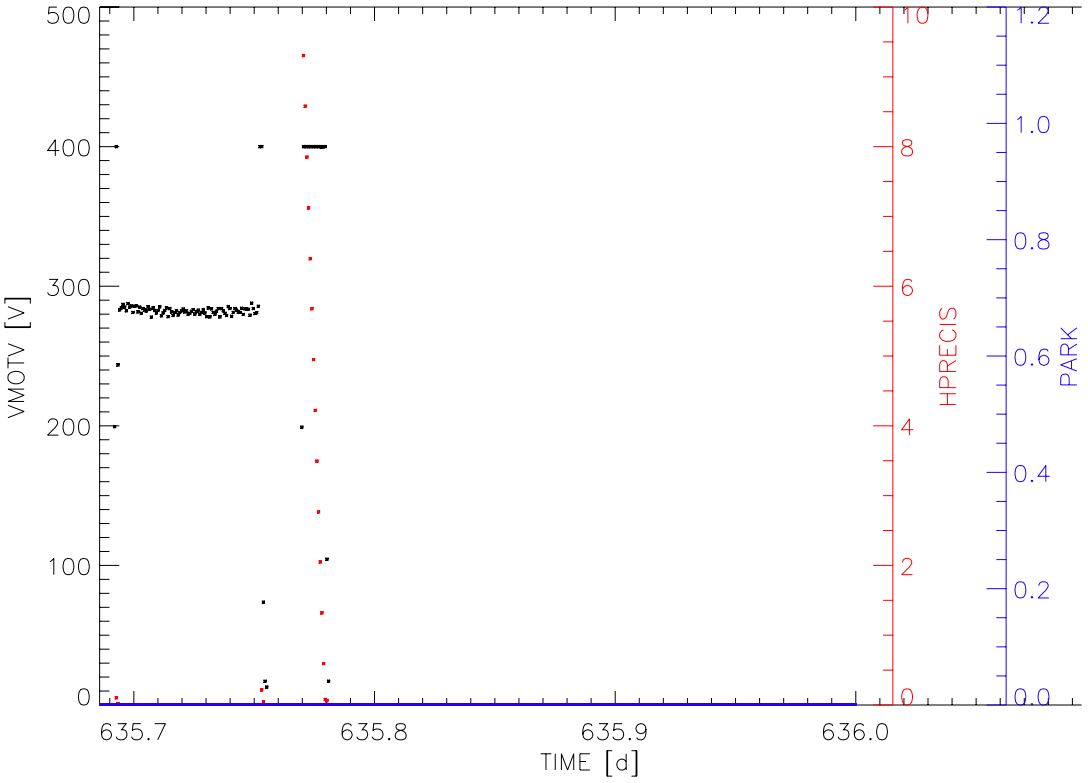

Figure B.1: Rejected trackings I. First half of day is missing in the slow control file.

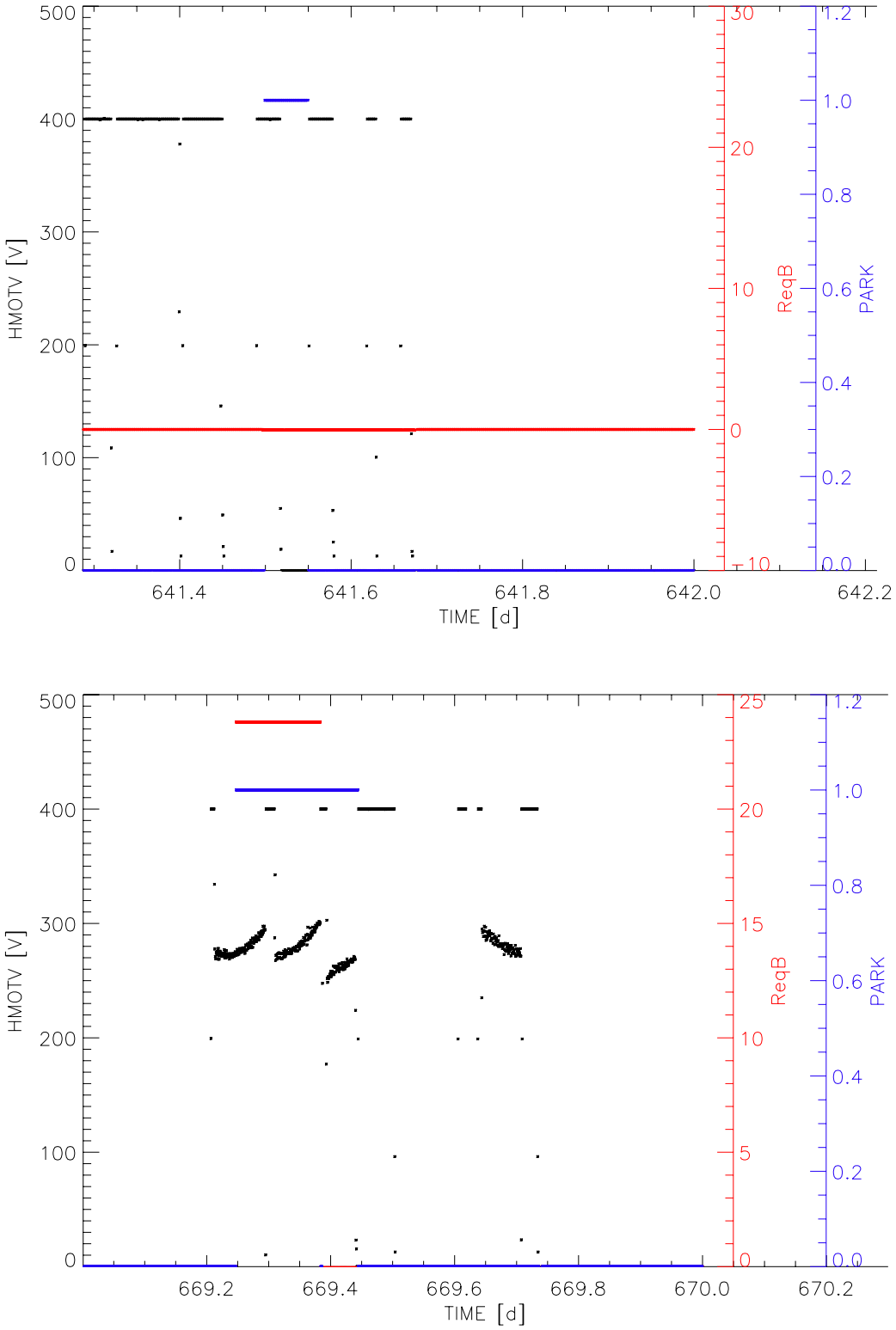

Figure B.2: Rejected trackings II. Upper picture: Horizontal motor not running. Lower Picture: Criteria for galactic tracking given during solar tracking.

C. Requested Coordinates

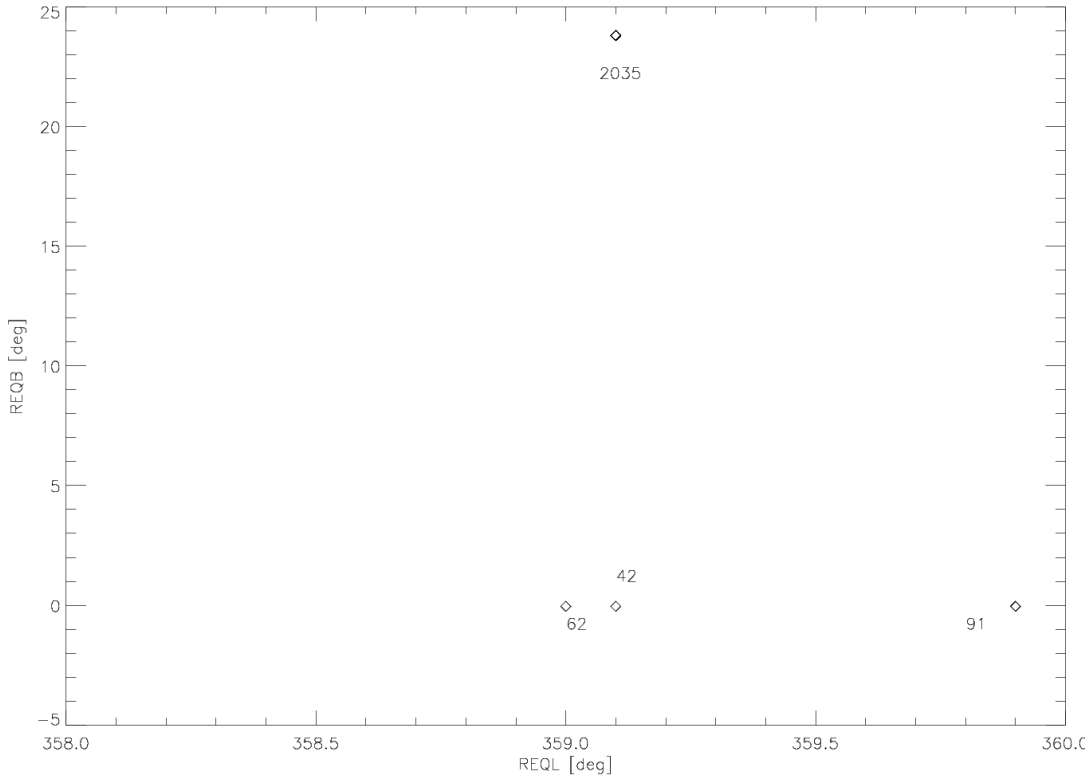

Figure C.1: Combinations of requested galactic coordinates. The number of entries in the tracking PC log-file are indicated by the numbers. Each entry in this file corresponds to one minute of observation. 2035 minutes of tracking Sco X-1 can be identified. Sgr A is tracked using standard coordinates for 92 minutes. A combination of Sco and Sgr coordinates by mistake is reported for 42 minutes. Note that the observation time mentioned here is not the total observation time for the analysis since other conditions that have to be fulfilled are not included.

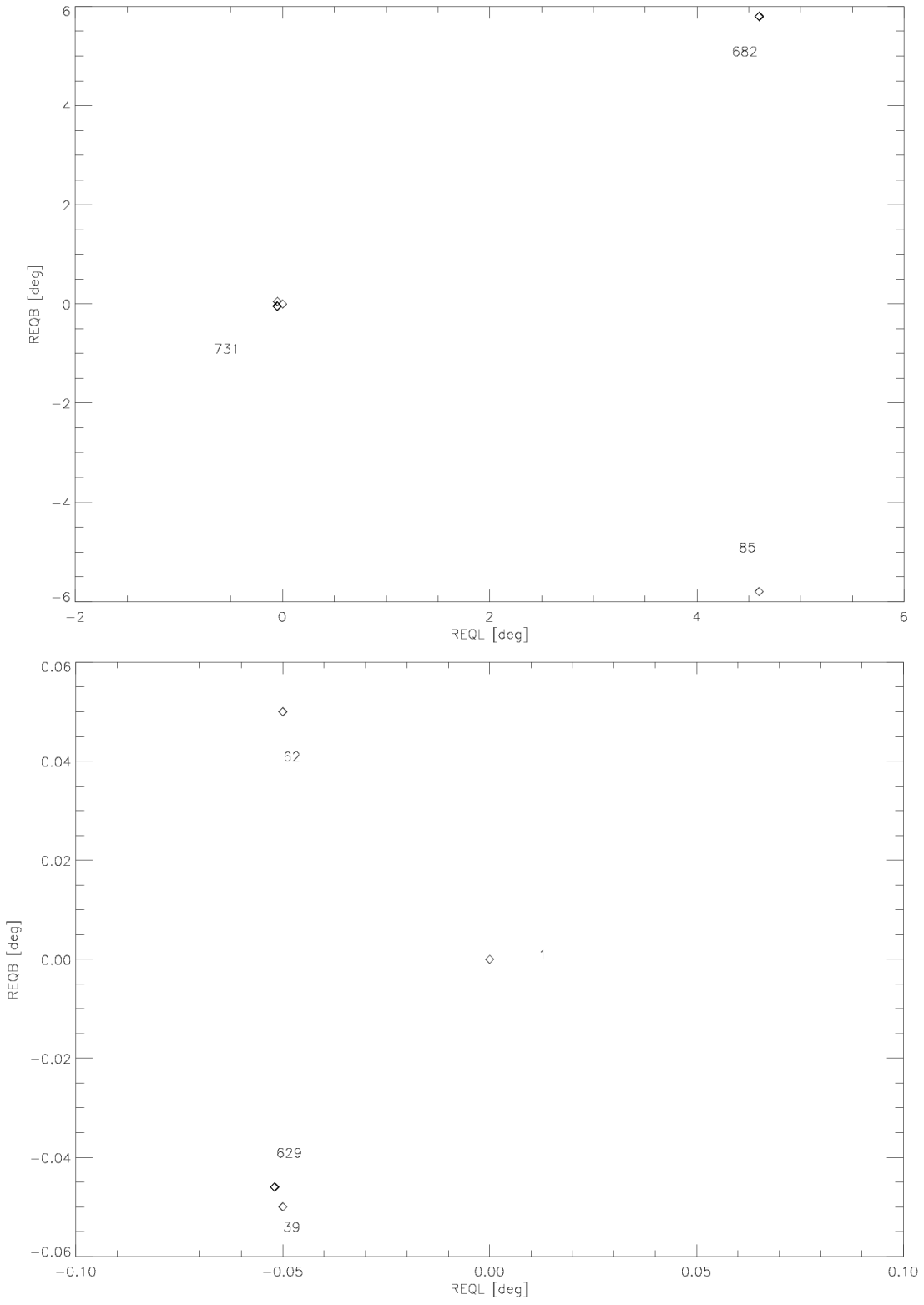

Figure C.2: Combinations of requested galactic coordinates. Upper picture: The bunch of points close together marks 731 minutes of tracking Sgr A. The other point origin from tracking of the Crab Nebula. Lower Picture: Close-up of Sgr trackings. The deviation of the requested coordinates is less than the size of the field of view.

D. Summary of Upper Limits on $\phi g_{a\gamma}^2$

Energy range [keV]	Bgrd def.	$(\phi g_{a\gamma}^2)_{\text{best}}$ [$\text{m}^{-2}\text{s}^{-1}\text{kev}^{-1}\text{GeV}^{-2}$]	Stat. error (left)	Stat. error (right)	$\phi g_{a\gamma}^2$ (95 % CL) [$\text{m}^{-2}\text{s}^{-1}\text{kev}^{-1}\text{GeV}^{-2}$]
Assuming a flat axion spectrum					
0.5 - 9.8	1	1.9×10^{-5}	1.1×10^{-5}	1.2×10^{-5}	4.12×10^{-5}
0.5 - 9.8	2	1.7×10^{-5}	1.1×10^{-5}	1.2×10^{-5}	3.98×10^{-5}
0.5 - 9.8	3	1.2×10^{-5}	1.2×10^{-5}	1.2×10^{-5}	3.58×10^{-5}
0.5 - 9.8*	1	$1.7 \times 10^{-}$	1.1×10^{-5}	1.2×10^{-5}	3.92×10^{-5}
0.5 - 9.8*	2	1.3×10^{-5}	1.1×10^{-5}	1.3×10^{-5}	3.69×10^{-5}
0.5 - 9.8*	3	1.0×10^{-5}	1.1×10^{-5}	1.3×10^{-5}	3.40×10^{-5}
1.0 - 10.0	1	1.9×10^{-5}	1.1×10^{-5}	1.4×10^{-5}	4.34×10^{-5}
1.0 - 10.0	2	2.0×10^{-5}	1.3×10^{-5}	1.4×10^{-5}	4.51×10^{-5}
1.0 - 10.0	3	1.4×10^{-5}	1.2×10^{-5}	1.3×10^{-5}	3.94×10^{-5}
1.0 - 7.0	1	1.5×10^{-5}	1.2×10^{-5}	1.4×10^{-5}	3.99×10^{-5}
1.0 - 7.0	2	1.5×10^{-5}	1.2×10^{-5}	1.3×10^{-5}	4.06×10^{-5}
1.0 - 7.0	3	1.1×10^{-5}	1.2×10^{-5}	1.4×10^{-5}	3.70×10^{-5}
Assuming a X-ray-like axion spetrum					
0.5 - 9.8	1	1.1×10^{-5}	0.5×10^{-5}	0.6×10^{-5}	2.20×10^{-5}
0.5 - 9.8	2	0.9×10^{-5}	0.6×10^{-5}	0.6×10^{-5}	2.09×10^{-5}
0.5 - 9.8	3	0.8×10^{-5}	0.6×10^{-5}	0.6×10^{-5}	1.95×10^{-5}
0.5 - 9.8*	1	$1.0 \times 10^{-}$	0.5×10^{-5}	0.6×10^{-5}	2.19×10^{-5}
0.5 - 9.8*	2	0.9×10^{-5}	0.5×10^{-5}	0.6×10^{-5}	2.07×10^{-5}
0.5 - 9.8*	3	0.8×10^{-5}	0.5×10^{-5}	0.6×10^{-5}	1.94×10^{-5}
1.0 - 10.0	1	0.9×10^{-5}	0.5×10^{-5}	0.6×10^{-5}	2.06×10^{-5}
1.0 - 10.0	2	0.9×10^{-5}	0.5×10^{-5}	0.6×10^{-5}	2.09×10^{-5}
1.0 - 10.0	3	0.8×10^{-5}	0.5×10^{-5}	0.6×10^{-5}	1.96×10^{-5}
1.0 - 7.0	1	1.3×10^{-5}	0.7×10^{-5}	0.9×10^{-5}	2.99×10^{-5}
1.0 - 7.0	2	1.2×10^{-5}	0.8×10^{-5}	0.9×10^{-5}	3.01×10^{-5}
1.0 - 7.0	3	1.1×10^{-5}	0.8×10^{-5}	0.9×10^{-5}	2.84×10^{-5}

Table D.1: Summary of upper limits on $\phi g_{a\gamma}^2$ for Sco X-1.

***: Copper peak between 7.1 and 8.9 keV removed.**

Energy range [keV]	Bgrd def.	$(\phi g_{a\gamma}^2)_{\text{best}}$ [$\text{m}^{-2}\text{s}^{-1}\text{keV}^{-1}\text{GeV}^{-2}$]	Stat. error (left)	Stat. error (right)	$\phi g_{a\gamma}^2$ (95 % CL) [$\text{m}^{-2}\text{s}^{-1}\text{keV}^{-1}\text{GeV}^{-2}$]
Assuming a flat axion spectrum					
0.5 - 9.8	1	0.9×10^{-5}	0.6×10^{-5}	1.2×10^{-5}	4.07×10^{-5}
0.5 - 9.8	2	-3.4×10^{-5}	1.0×10^{-5}	1.6×10^{-5}	3.19×10^{-5}
0.5 - 9.8	3	-4.8×10^{-5}	1.2×10^{-5}	1.7×10^{-5}	3.07×10^{-5}
0.5 - 9.8*	1	$0.9 \times 10^{-}$	0.6×10^{-5}	1.2×10^{-5}	3.99×10^{-5}
0.5 - 9.8*	2	-3.9×10^{-5}	0.7×10^{-5}	1.4×10^{-5}	3.02×10^{-5}
0.5 - 9.8*	3	-5.5×10^{-5}	1.0×10^{-5}	1.5×10^{-5}	2.96×10^{-5}
1.0 - 10.0	1	-2.8×10^{-5}	1.1×10^{-5}	1.7×10^{-5}	3.43×10^{-5}
1.0 - 10.0	2	-5.8×10^{-5}	9.5×10^{-5}	1.6×10^{-5}	3.08×10^{-5}
1.0 - 10.0	3	-6.0×10^{-5}	1.1×10^{-5}	1.6×10^{-5}	3.07×10^{-5}
1.0 - 7.0	1	-3.2×10^{-5}	0.9×10^{-5}	1.5×10^{-5}	3.46×10^{-5}
1.0 - 7.0	2	-7.5×10^{-5}	0.8×10^{-5}	1.5×10^{-5}	3.11×10^{-5}
1.0 - 7.0	3	-7.1×10^{-5}	0.8×10^{-5}	1.4×10^{-5}	3.12×10^{-5}
Assuming a X-ray-like axion spetrum					
0.5 - 9.8	1	0.7×10^{-5}	0.5×10^{-5}	0.9×10^{-5}	3.20×10^{-5}
0.5 - 9.8	2	-2.5×10^{-5}	0.6×10^{-5}	1.3×10^{-5}	2.52×10^{-5}
0.5 - 9.8	3	-2.4×10^{-5}	0.6×10^{-5}	1.1×10^{-5}	2.48×10^{-5}
0.5 - 9.8*	1	$0.7 \times 10^{-}$	0.5×10^{-5}	0.9×10^{-5}	3.13×10^{-5}
0.5 - 9.8*	2	-2.6×10^{-5}	0.6×10^{-5}	1.1×10^{-5}	2.45×10^{-5}
0.5 - 9.8*	3	-2.4×10^{-5}	0.6×10^{-5}	1.1×10^{-5}	2.43×10^{-5}
1.0 - 10.0	1	-1.1×10^{-5}	0.7×10^{-5}	1.2×10^{-5}	2.87×10^{-5}
1.0 - 10.0	2	-3.3×10^{-5}	0.6×10^{-5}	1.2×10^{-5}	2.52×10^{-5}
1.0 - 10.0	3	-3.2×10^{-5}	0.7×10^{-5}	1.2×10^{-5}	2.52×10^{-5}
1.0 - 7.0	1	-1.6×10^{-5}	1.0×10^{-5}	1.6×10^{-5}	3.83×10^{-5}
1.0 - 7.0	2	-4.5×10^{-5}	0.8×10^{-5}	1.5×10^{-5}	3.39×10^{-5}
1.0 - 7.0	3	-4.5×10^{-5}	0.9×10^{-5}	1.5×10^{-5}	3.40×10^{-5}

Table D.2: Summary of upper limits on $\phi g_{a\gamma}^2$ for Sgr A.

***: Copper peak between 7.1 and 8.9 keV removed.**

Bibliography

[1] C. E. Aalseth et al.: Proposal to the SPSC: A solar axion search using a decommissioned LHC test magnet CERN-SPSC-P-312

[2] K. Zioutas et al.: A decommissioned LHC model magnet as an axion telescope; *Nucl. Instrum. Meth.* A425: (1999), 480–489; `astro-ph/9801176`

[3] T. P. Cheng and L. F. Li: *Gauge theory of elementary particle physics: Problems and solutions*; Clarendon, Oxford (2000)

[4] R. D. Peccei: The strong CP problem and axions; *Lect. Notes Phys.* 741: (2008), 3–17; `hep-ph/0607268`

[5] C. Quigg: Gauge theories of the strong, weak and electromagnetic interactions; *Front. Phys.* 56: (1983), 1–334

[6] G. 't Hooft: Symmetry breaking through Bell-Jackiw anomalies; *Phys. Rev. Lett.* 37: (1976), 8–11

[7] J. E. Kim: Light Pseudoscalars, Particle Physics and Cosmology; *Phys. Rept.* 150: (1987), 1–177

[8] R. J. Crewther et al.: Chiral Estimate of the Electric Dipole Moment of the Neutron in Quantum Chromodynamics; *Phys. Lett.* B88: (1979), 123

[9] N. F. Ramsey: Electric dipole moment of the neutron; *Ann. Rev. Nucl. Part. Sci.* 40: (1990), 1–14

[10] C. Amsler et al.: Review of particle physics; *Phys. Lett.* B667: (2008), 1

[11] R. D. Peccei and H. R. Quinn: CP Conservation in the Presence of Instantons; *Phys. Rev. Lett.* 38: (1977), 1440–1443

[12] R. D. Peccei and H. R. Quinn: Constraints Imposed by CP Conservation in the Presence of Instantons; *Phys. Rev.* D16: (1977), 1791–1797

[13] S. Weinberg: A New Light Boson?; *Phys. Rev. Lett.* 40: (1978), 223–226

[14] F. Wilczek: Problem of Strong p and t Invariance in the Presence of Instantons; *Phys. Rev. Lett.* 40: (1978), 279–282

[15] E. Arik et al.: Probing eV-scale axions with CAST; *JCAP* 0902: (2009), 008; 0810.4482

[16] G. G. Raffelt: Axions: Motivation, limits and serches; Presentation in PONT d'Avignon (21-25 Apr 2008)

[17] A. Weigert, H. J. Wendker and L. Wisotzki: *Astronomy and astrophysics (In German)*; Wiley-VCH, Weinheim; 4 edn. (2005)

[18] D. Clowe et al.: A direct empirical proof of the existence of dark matter; *Astrophys. J.* 648: (2006), L109–L113; astro-ph/0608407

[19] F. D. Steffen: Dark Matter Candidates - Axions, Neutralinos, Gravitinos, and Axinos; *Eur. Phys. J.* C59: (2009), 557–588; 0811.3347

[20] S. Hannestad et al.: Cosmological constraints on neutrino plus axion hot dark matter: Update after WMAP-5; *JCAP* 0804: (2008), 019; 0803.1585

[21] J. Lesgourgues and S. Pastor: Massive neutrinos and cosmology; *Phys. Rept.* 429: (2006), 307–379; astro-ph/0603494

[22] J. Gasser and H. Leutwyler: Quark Masses; *Phys. Rept.* 87: (1982), 77–169

[23] G. G. Raffelt: *Stars as laboratories for fundamental physics: The astrophysics of neutrinos, axions, and other weakly interacting particles*; The University of Chicago Press, Chicago, London (1996)

[24] J. Vogel: *Searching for Solar Axions in the eV-Mass Region with the CCD Detector at CAST*; Phd thesis; Albert-Ludwigs-Universität; Freiburg (2009)

[25] C. Edwards et al.: Upper Limit for $J/\psi \to \gamma$ + Axion; *Phys. Rev. Lett.* 48: (1982), 903

[26] M. B. Wise, H. Georgi and S. L. Glashow: SU(5) and the Invisible Axion; *Phys. Rev. Lett.* 47: (1981), 402

[27] J. E. Kim: Weak Interaction Singlet and Strong CP Invariance; *Phys. Rev. Lett.* 43: (1979), 103

[28] M. A. Shifman, A. I. Vainshtein and V. I. Zakharov: Can Confinement Ensure Natural CP Invariance of Strong Interactions?; *Nucl. Phys.* B166: (1980), 493

[29] M. Dine, W. Fischler and M. Srednicki: A Simple Solution to the Strong CP Problem with a Harmless Axion; *Phys. Lett.* B104: (1981), 199

[30] A. R. Zhitnitsky: On Possible Suppression of the Axion Hadron Interactions. (In Russian); *Sov. J. Nucl. Phys.* 31: (1980), 260

[31] G. G. Raffelt: Astrophysical axion bounds; *Lect. Notes Phys.* 741: (2008), 51–71; hep-ph/0611350

[32] S. Hannestad et al.: Cosmological constraints on neutrino plus axion hot dark matter; *JCAP* 0708: (2007), 015; 0706.4198

[33] J. Preskill, M. B. Wise and F. Wilczek: Cosmology of the invisible axion; *Phys. Lett.* B120: (1983), 127–132

[34] M. Dine and W. Fischler: The not-so-harmless axion; *Phys. Lett.* B120: (1983), 137–141

[35] L. F. Abbott and P. Sikivie: A cosmological bound on the invisible axion; *Phys. Lett.* B120: (1983), 133–136

[36] P. Sikivie: Axion cosmology; *Lect. Notes Phys.* 741: (2008), 19–50; astro-ph/0610440

[37] P. Sikivie: Experimental tests of the *invisible* axion; *Phys. Rev. Lett.* 51: (1983), 1415

[38] L. D. Duffy et al.: A High Resolution Search for Dark-Matter Axions; *Phys. Rev.* D74: (2006), 012006; astro-ph/0603108

[39] Z. Ahmed et al.: Search for Axions with the CDMS Experiment 0902.4693

[40] G. Cantatore: Recent results from the PVLAS experiment on the magnetized vacuum; *Lect. Notes Phys.* 741: (2008), 157–197

[41] P. Pugnat et al.: First results from the OSQAR photon regeneration experiment: No light shining through a wall; *Phys. Rev.* D78: (2008), 092003; 0712.3362

[42] R. Kotthaus et al.: The X-ray telescope of the CAST experiment astro-ph/0511390

[43] D. Kang: *Search for solar axions with the CCD detector at CAST (CERN Axion Solar Telescope)*; PhD Thesis; Albert-Ludwigs-Universität; Freiburg (2007)

[44] http://doc.cern.ch//archive/electronic/cern/others/PHO/photo-di/

[45] M. Bona et al.: Performance of the first CERN - INFN 10 m long superconducting dipole prototype for the LHC; Presentation at 4th European Particle Accelerator Conference (EPAC 94) (27 Jun - 1 Jul 1994)

[46] K. Barth et al.: Commissioning and first operation of the cryogenics for the cern axion solar telescope (cast); *AIP Conf. Proc.* 710 (CERN-AT-2004-001-ECR): (2004), 168–175. 8 p

[47] Silvia Borghi, private communication

[48] J. Collar: A few precisions on tracking precision; Presentation at 18th CAST collaboration meeting (Oct 2003)

[49] M. Kuster, D. Nowakowski and A. Nordt: The CAST Sky-Survey; Presentation at 37th CAST collaboration meeting (15 - 17 Oct 2008)

[50] J. Vogel: *The Precision of the Tracking System in Search of Solar Axions*; Diploma Thesis; Albert-Ludwigs-Universität; Freiburg (2005)

[51] D. Autiero et al.: The CAST time projection chamber; *New J. Phys.* 9: (2007), 171; physics/0702189

[52] P. Abbon et al.: The Micromegas detector of the CAST experiment; *New J. Phys.* 9: (2007), 170; physics/0702190

[53] M. Kuster et al.: The X-ray Telescope of CAST; *New J. Phys.* 9: (2007), 169; physics/0702188

[54] L. Strüder: High-resolution X-ray spectrometers; *Nucl. Instrum. Methods* A454: (2000), 73

[55] L. Strüder et al.: The European Photon Imaging Camera on XMM-Newton: The pn- CCD camera; *Astron. Astrophys.* 365: (2001), L18–26

[56] J. Franz: Axion Search - Normalization; internal report

[57] K. van Bibber et al.: Design for a practical laboratory detector for solar axions; *Phys. Rev.* D39: (1989), 2089

[58] D. Steeghs and J. Casares: The mass donor of Scorpius X-1 revealed astro-ph/0107343

[59] L. Titarchuk et al.: Normal Branch Quasi-Periodic Oscillations in Sco X-1: Viscous Oscillations of a Spherical Shell Near the Neutron Star s astro-ph/0105559

[60] S. Gillessen et al.: Monitoring stellar orbits around the Massive Black Hole in the Galactic Center; *Astrophys. J.* 692: (2009), 1075–1109; 0810.4674

[61] S. Doeleman et al.: Event-horizon-scale structure in the supermassive black hole candidate at the Galactic Centre; *Nature* 455: (2008), 78; 0809.2442

[62] G. Belanger et al.: Repeated X-ray Flaring Activity in Sagittarius A*; *Astrophys. J.* 635: (2005), 1095–1102; astro-ph/0508412

[63] M. Bejger and P. Haensel: Moments of inertia for neutron and strange stars: Limits derived for the Crab pulsar; *Astron. Astrophys.* 396: (2002), 917; astro-ph/0209151

[64] Konstantin Zioutas, private communication

[65] M. D. Hannam and W. J. Thompson: Estimating small signals by using maximum likelihood and Poisson statistics; *Nucl. Instrum. Meth.* A431: (1999), 239–251

[66] R. Barlow: *Statistics. A Guide to the Use of Statistical Methods in the Physical Sciences*; John Wiley & Sons, Chichester (1989)

[67] L. Lyons: *Statistics for nuclear and particle physicists*; Cambridge Univerity Press, Cambridge (1986)

Deutschsprachige Zusammenfassung

Das Standardmodell der Teilchenphysik ist eine erfolgreiche Theorie zur Beschreibung der starken, schwachen und elektromagnetischen Wechselwirkung. Allerdings gibt es innerhalb des Standardmodells einige Details, die bisher nicht verstanden werden können, so z.B. das starke CP-Problem. Verletzung der Invarianz unter Vertauschung des Ladungsvorzeichens (sogenannte C-Konjugation), kombiniert mit Raumspiegelung (sogenannte P-Konjugation) ist für die schwache, nicht aber im Falle der starken Wechselwirkung experimentell beobachtet worden. Eine Erklärung für diesen Umstand könnte die Existenz einer weiteren, spontan gebrochenen Symmetrie in der Quanten-Chromo-Dynamik (QCD) liefern. Diese gebrochene Symmetrie wiederum würde einem leichten, pseudoskalaren Teilchen, dem Axion, entsprechen. Die ursprüngliche Annnahme einer Axionenmasse von etwa 100 keV/c^2 wurde recht bald experimentell ausgeräumt, aber kurz darauf entwickelte Theorien, die eine deutlich leichtere Variante des Axions vorschlagen, gilt es immer noch zu überprüfen.

Sollten Axionen existieren, könnten sie u.A. durch den Primakoff-Effekt erzeugt werden. Reelle Photonen wechselwirken mit virtuellen Photonen, die aus einem elektrischen oder magnetischen Feld stammen, und erzeugen so Axionen. Zum Nachweis von Axionen kann der Primakoff-Effekt umgekehrt werden. Axionen, die z.B. in ein Magnetfeld eindringen, können so in Photonen entsprechender Energie umgewandelt werden, die wiederum mit herkömmlichen (Röntgen-) Detektoren nachgewiesen werden. Auf dieser Funktionsweise beruht das CAST Experiment am CERN. Ein ausgemusteter LHC Dipol-Prototyp wird verwendet, um ein Magnetfeld von ca. 9 T zu erzeugen. Der Magnet selbst ist dreh- und schwenkbar gelagert und kann daher für etwa 1,5 Stunden auf ein Objekt der Wahl ausgerichtet werden, wobei die genaue Messzeit von der Position des gewünschten Zieles abhängt. Obwohl CAST in erster Linie gebaut wurde um Axionen aus dem Sonneninneren nachzuweisen, wurde noch vor der Inbetriebnahme des Experimentes beschlossen, einige galaktische Objekte zu beobachten, die besonders vielversprechend erscheinen. Unter diesen befindet sich Scorpius X-1, nach der Sonne die hellste Röntegquelle am Himmel, sowie das Zentrum der Milchstraße, Sagittarius A.

Im Rahmen der vorliegenden Arbeit wurden die Daten analysiert, die während der Beobachtung der beiden erwähnten Objekte mit dem CCD Detektor gesammelt wurden. Aufgrund der seinerzeit vorliegenden Kohärenzbedingung beziehen sich alle so gewonnenen Ergebnisse auf Axionen mit Masse kleiner als 0.02 eV/c^2. Da kein Signal oberhalb des Hintergrundniveaus gefunden werden konnte, wird ein Upper Limit auf

den freien Parameter Fluss mal Axion-Photon Kopplungskonstante^2 ($\phi g_{a\gamma}^2$) extrahiert. Um die Analyse möglichst unvoreingenommen durchzuführen, werden dabei verschiedenen Energiebereiche, die durch die Sensitivität des Röntgenteleskopes und der CCD vorgegeben sind, analysiert. Verschiedene Hintergrunddefinitionen werden angewandt und der erwartete Verlauf des Axionspektrums wird ein Mal als flach, ein anderes Mal als dem Röntgenspektrum des Zielobjektes entsprechend, angenommen. Die so gewonnenen Ergebnisse variieren, bewegen sich aber im Bereich

$$\phi g_{a\gamma}^2(95\ \%\ \mathrm{CL}) \approx 2\ -\ 5 \times 10^{-5}\ \mathrm{m^{-2}s^{-1}keV^{-1}GeV^{-2}}.$$

Generell fällt dabei auf, dass die Ergebnisse für Sgr A trotz kürzerer Messdauer besser sind als die für Sco X-1. Da dieser Umstand den Erwartungen widerspricht, wurde anhand von Hintergrundverteilungen und Detektorcharakteristiken sichergestellt, dass kein sytematischer Effekt vorliegt, sondern diese Abweichung lediglich statistischer Natur ist.

Unter Anwendung der Obergrenze für die Kopplungskonstante aus Phase I des CAST Experimentes kann ein Bereich neuer Erkenntnis im Parameterraum ermittelt werden, der durch den Fluss und die Kopplungskonstante aufgespannt wird. Trägt man beide Größen logarithmisch auf, ergibt sich eine Gerade, die dem extrahierten Upper Limit entspricht. Unterhalb dieser Geraden sind alle Kombinationen aus Fluss und Kopplungskonstante erlaubt, die Kombinationen oberhalb dieser Geraden sind ausgeschlossen. Die Obergrenze auf die Kopplungskonstante entspricht in dieser Auftragung einer Senkrechten. Der Schnittpunkt von Ausschlussgerade und Kopplungskonstante kann auf die Flussachse projiziert werden (vgl. Abb. 5.22). Dieser Wert entspricht einem maximalen differentiellen Fluss, der kombiniert mit allen noch nicht ausgeschlossenen Möglichkeiten für die Kopplungskonstante keine ausgeschlossenen Paare bilden kann. Für Flüsse kleiner als dieser Grenzwert sind also keine neuen Erkentnisse gewonnen.

Ist die Entfernung zum beobachteten Objekt bekannt und kann jedem Axion eine minimale Energie zugeordnet werden, so kann der Grenzwert des Flusses in einen Grenzenergieverlust pro Zeit umgerechnet werden. D.h., die beobachteten Objekte könnten Axionen mit dieser Leistung abstrahlen, ohne dass die Möglichkeit eines Nachweises durch CAST bei moderater Messdauer besteht. Die entsprechenden Grenzwerte für Scorpio X-1 und Sagittarius A lauten

$$P_{\mathrm{max,Sco}} \sim 5 \times 10^{41}\ \mathrm{W},$$
$$P_{\mathrm{max,Sgr}} \sim 4 \times 10^{42}\ \mathrm{W},$$

falls eine Energie von mindestens einem keV pro Axion angenommen wird. Vergleicht man diese Leistung mit der Leistung der Sonne (ca. 10^{26} W) oder der integrierten Röntgenleistung von Sco X-1 (ca. 10^{31} W), wird deutlich, dass Axionenteleskope wie CAST zur Beobachtung von Axionen galaktischen Ursprungs nicht geeignet erscheinen.

Acknowledgments

This thesis would not have been possible without the help of many people. First of all I have to thank my supervisor Kay Königsmann for giving me the opportunity to join his group and for always lending an ear to my questions. I also have to thank Horst Fischer who helped me a lot both in physics and by making my trips to CERN as uncomplicated as they were.

Special thanks are addressed to Julia Vogel, who I think suffered the most from my countless questions on CAST. Thanks for proofreading and never loosing patience!
I also benefited from the constant support and help of the other members of the CCD group: Elisabeth Gruber, Donghwa Kang, Annika Nordt and especially Markus Kuster.

Konstantin Zioutas should be mentioned here representing all the CAST collaboration. I always had the feeling of being welcome, right from the moment I joined the collaboration. The experienced cooperativeness can be exemplified by two names: Silvia Borghi took the time to explain the tracking software to me and Michael Pivovaroff provided me with light curves of the galactic objects in no time, without having to.

I should not forget to mention my gratitude to all the members of Group Königsmann, who helped me with the countless little things: Stefan Bartknecht, Jochen Barwind, Rainer Fastner, Jürgen Franz, Florian Herrmann, Louis Lauser, Andreas Mutter, Frank Nerling, Khalil Rehmani, Susanne Rombach-Mikl, Christian Schill, Sebastian Schoperer, Johannes ter Wolbeek, Heiner Wollny and Elisabeth Wursthorn.

Last but not least I have to thank my parents for supporting me all the time and Christiane Focke who steadily encouraged me and stood the ”pleasure” of proofreading this thesis.

Erklärung

Diese Arbeit ist von mir selbständig verfasst worden und ich habe keine anderen als die angegebenen Quellen als Hilfsmittel verwendet.

Tillmann Guthörl, September 2009